

Doctorate Thesis

**Study of the Conditions that Determine the
Formation of Coronal Mass Ejections Using Models of
the Coronal Magnetic Field**

(太陽コロナ磁場モデルに基づくコロナ質量放出の形成条件
に関する研究)

By:
LIN Pei Hsuan

Supervisor:
Prof. Kanya Kusano

Nagoya University
January 2021

Abstract

Solar flares and coronal mass ejections (CME) are two important solar eruptions that release the magnetic energy stored in the active regions (ARs) of the Sun through the magnetic reconnections and MHD instabilities. Notwithstanding these two phenomena are indicated to be two different manifestations for an identical energy release, observations have shown that solar flares and CMEs are in fact not a one-to-one relationship. To date, it is still unclear what determines the capability of an AR to specifically produce eruptive flares and CMEs, and this hinders our knowledge of the initiation mechanism for the eruptive component of these phenomena. We believe that the relative strength of magnetic flux ropes (MFRs) to the magnetic field in the immediate vicinity is key to analyze the CME-eruptivity. Based on data obtained by the Solar Dynamics Observatory/Heliioseismic and Magnetic Imager, the coronal magnetic field for 51 flares larger than M5.0 class, from 29 distinct ARs, is constructed using a nonlinear force-free field extrapolation model. Statistical analysis based on linear discriminant function analysis (DA) is performed to answer the question of what determines the capability of a solar AR to specifically produce eruptive flares and CMEs.

In the first part of this study, we propose a new parameter r_m to measure the possibility that a flare which occurs in an AR can be eruptive and produce a CME. The parameter r_m is defined by the ratio of the magnetic flux of twist higher than a threshold T_c to the surrounding –and specifically the overlying – magnetic flux. We find that the foot-points of field lines with twist larger than 0.2 can well represent the subsequent flare ribbons by comparing the flare-ribbon-associated magnetic flux provided by Toriumi et al. (2017). The results revealed by linear DA suggest that r_m is moderately well able to distinguish ARs that have the capability of producing eruptive events (vs. confined events). Moreover, field lines overlying and “fencing in” the highly twisted region will work to confine the eruption, generating confined flares.

Second, to understand why r_m failed to correctly determine the CME-eruptivities of three flares originating from AR 12192, two new schemes of identifying those field lines involved in eruptions, the r -scheme, and q -scheme, are proposed to analyze the eruptive and confined nature of solar

flares, as extensions to the original r_m scheme. Motivated by three solar flares originating from NOAA Active Region 12192 that are mis-classified by r_m we introduce refinements to the r -scheme employing the “magnetic twist flux” to approximate the force balance acting on the MFR; in the q -scheme, the reconnected field is represented by those field lines which anchor in the flare ribbons. The linear DA results show that despite both schemes providing moderately successful classifications for the 51 flares, the CME-eruptivity classification for the three target events can only be improved with the q -scheme. An analysis based on the torus instability shows that the expected eruptivity changes with approximations of MFRs defined by different schemes, emphasizing the importance of correctly separating the volume of an MFR from the ambient magnetic field. We find that the highly twisted field lines and the flare-ribbon field lines have equal average force-free constant α , but all of the flare-ribbon-related fieldlines are shorter than 150 Mm in length. The findings lead us to conclude that it is challenging to distinguish the MFR from the ambient magnetic field using any quantity based on common magnetic nonpotentiality measures.

Our results demonstrate the importance of considering the suppressive field-line topology and identifying core MFRs when analyzing the eruptivity. We conclude that even though both r - and q -scheme can be applied to most of the solar eruptions, more than one mechanism may govern CME production such that they are only moderately able to classify the eruptions.

Acknowledgements

Foremost, I would like to express my sincere gratitude to my advisors: Prof. Kanya Kusano and Dr. KD Leka, for their patience, motivation, and immense knowledge. Without the assistance and dedicated involvement in every step throughout the process, this study would have never been accomplished

I would like to thank my thesis committee members for all of their guidance through this process; your discussion, ideas, and feedback have been absolutely invaluable.

Besides my advisor, I would like to thank my collaborators: Dr. Satoshi Inoue, Dr. Daikou Shiota, and for their insightful comments, hard questions, and discussions that improved the manuscript for the publications. I thank to Assoc. Prof. Satoshi Masuda, Dr. Shinsuke Imada, Dr. Sung-Hong Park, Dr. Takafumi Kaneko, Dr. Takuma Matsumoto, Dr. Haruhisa Iijima, and Dr. Shin Toriumi for their supports and helps to my research. I thank to all my fellow students in ISEE, for the discussions, supports of life in Japan, and for all the fun we have had in the last three years. Also, I thank to all secretaries in Integrated Studies group in ISEE, especially Ms. Motoko Kunieda, who helps me a lot with the administrative works and overseas internship. I also thank to Ms. Tae Torii in ISEE office for helping me deal with the administrative works, managing academic procedures, and paperwork during my study.

My sincere thanks also go to Lockheed-Martin Solar and Astrophysics Laboratory (LMSAL) for offering me the internship opportunities in their groups and providing a lot of valuable comments. I thank to Project for Solar-Terrestrial Environment Prediction (PSTEP) for the financial supports during the internship.

I would like to acknowledge the Japan-Taiwan Exchange Association for giving me the scholarship and financial support during my stay at Nagoya University. This work was supported by MEXT/JSPS KAKENHI Grant Number JP15H05814. A part of this work was carried by using the computational resource of the Center for Integrated Data Science, ISEE, Nagoya University.

Finally, my thanks go to all the people who have supported me to complete the research work directly or indirectly.

Contents

Abstract	i
Acknowledgements	iii
List of Figures	ix
List of Tables	xiii
1 Introduction	1
1.1 Solar eruptions	2
1.2 Solar force-free magnetic field model	10
1.3 CME-initialization model	14
1.4 Motivation and scientific objective	22
2 Event List, Data, and Method	25
2.1 Event list	25
2.2 SDO spacecraft	28
2.3 Coronal magnetic field construction	30
2.3.1 MHD relaxation method	31
2.3.2 Validity of NLFFF extrapolation	36
2.4 Linear discriminant function analysis	39

3	A New Parameter from Coronal Magnetic Field Models to distinguish Eruptive-Flare Producing Solar Active Regions	45
3.1	A new parameter: r_m	46
3.1.1	Concept of r_m parameter	47
3.1.2	Magnetic twist and highly twisted region	50
3.2	Results and Discussion	55
3.2.1	Comparison of highly twisted magnetic flux and flare-ribbon magnetic flux	55
3.2.2	Overlying field and wall Field	59
3.2.3	DA results	64
3.2.4	An exceptional event: X1.2 flare on 2014 January 7	66
3.3	Summary and Conclusion	69
4	Eruptivity in Solar Flares: The Challenges of Finding the Magnetic Flux Rope	71
4.1	Exceptional events under the r_m -scheme from NOAA AR 12192	72
4.2	Analysis	75
4.2.1	Testing hypothesis #1: the r_τ parameter and r_κ parameter	75
4.2.2	Testing hypothesis # 2 with the q-schemes: q_m , q_τ , and q_κ	81
4.3	Discussion	92
4.3.1	Critical height analysis	92
4.3.2	Differences between the “highly-twisted” regions and the “flare ribbon” Regions	95
4.4	Summary and conclusions	100
5	Conclusions and Future Work	103
	References	107
	Appendices	
A	Highly Twisted Region with $T_c = 0.1$	127

B Error Analysis	131
C Flare Ribbon Area Sensitivity to Different Intensity Thresholds	133

List of Figures

1.1	A three-part structure CME captured by the SOHO-LASCO C2.	4
1.2	Schematic diagram of magnetic reconnection.	5
1.3	Schematic diagram of the CSHKP model.	7
1.4	Schematic diagram of the CSHKP model in a 3-D fashion.	8
1.5	Schematic diagram of a CME.	9
1.6	Plasma β model as a function of height above the photosphere.	12
1.7	Schematic diagram of equilibrium states.	15
1.8	Schematic diagram of the magnetic breakout model.	16
1.9	Schematic diagram of the tether cutting model.	17
1.10	Observation and simulation of the kink instability.	18
1.11	Titiov-Démoulin model.	19
1.12	Schematic diagram of the double arc instability.	20
2.1	Top view of the Solar Dynamics Observatory spacecraft.	28
2.2	The method of generating the lower boundary of the PFSS model.	32
2.3	Demonstration of non-linear force free field extrapolation results.	35
2.4	Force-freeness during the relaxation time.	36
2.5	An example of linear DA results.	40
3.1	Schematic diagram of an MFR suspended in the solar corona.	48

3.2	Comparison of α inferred from observations and NLFFF constructions.	49
3.3	Demonstration of processes for identifying the highly twisted flux.	50
3.4	All events with the highly twisted flux used for analysis indicated.	53
3.4	(<i>cont.</i>)	54
3.5	Scatter plots present the comparison of the highly-twisted magnetic flux and flare-ribbon flux.	56
3.6	Schematic of twist distributions among field lines involved in a tether-cutting reconnection.	59
3.7	Schematic for overlying field lines and wall field lines.	60
3.8	Curves illustrate selected highly-twisted, overlying, and wall field lines in event #1.	61
3.9	Linear DA results of r_m^o and r_m^{o+w}	64
3.10	SDO/AIA observations of AR11944 and AR11943 at different times.	67
3.11	Selected NLFFF reconstruction of coronal field lines for event #29 at Jan 7 17:00 UT.	68
4.1	SDO/AIA 94 Å, SDO/AIA 1600 Å observations, and NLFFF extrapolation overlaid on SHARP magnetogram data results of AR12192.	73
4.2	Histograms of r_τ^o , r_τ^{o+w} , r_κ^o , and r_κ^{o+w} for eruptive events and confined events.	79
4.3	The comparison of the resulting DA metrics for r -scheme and q -scheme.	82
4.4	De-saturated procedure applied on the SDO/AIA 1600 Å images remapped into CEA projections.	85
4.5	Deriving the Φ_{Ribbon} , $\Phi_{\text{overlying,R}}$, and $\Phi_{\text{wall,R}}$, demonstrated on event #36.	86
4.6	Histograms of q_m^o , q_m^{o+w} , q_τ^o , q_τ^{o+w} , q_κ^o , and q_κ^{o+w} for eruptive events and confined events.	90
4.7	Decay index with height contour plot overlaid on photospheric CEA B_r magnetograms.	93
4.8	Map of integrated twist T_w , lengths of field lines (L), and (g)-(i) force-free constant (α) for event #35, #36, and #37.	96
4.9	Diagram of α versus L for (a) event #35, (b) event #36, and (c) event #37.	97
4.10	Temporal evolution of flare ribbons overlaid on the SHARP B_r magnetogram for events #35, #36, and #37.	98

- A.1 Scatter plot presents the comparison of the $\Phi_{|T_w| \geq 0.1}$ and the Φ_{Ribbon} 128
- A.2 Highly twist regions with different value of T_c demonstrated by event #38. 129

List of Tables

1.1	Classification of solar flares based on <i>GOES</i> X-soft ray observations.	2
2.1	Event list for analysis.	27
2.2	The wavelength channels of AIA and the the primary emission lines observed by AIA (the information listed in this table is adopted from Lemen et al. (2011)).	30
2.3	NLFFF model extrapolation metrics.	38
2.4	Example of a classification table.	42
3.1	Highly twisted flux based on different T_c	58
3.2	Estimations related to r_m	63
3.3	DA results (with $n - 1$ cross-validation) of r_m^o and r_m^{o+w}	65
3.4	Classification table (with $n - 1$ cross-validation) for r_m^o	66
3.5	Classification table (with $n - 1$ cross-validation) for r_m^{o+w}	66
4.1	r_m -exception events for analysis	74
4.2	Estimations related to r_τ and r_κ	78
4.3	DA results (with $n - 1$ cross-validation) of the parameters in r -scheme	80
4.4	Estimations related to q_m , q_τ and q_κ	88
4.5	DA results (with $n - 1$ Cross-validation)	91
4.6	Comparison of DA results across different schemes	92

C.1	Maximum variation rate with different intensity thresholds	135
C.2	DA results (with $n - 1$ cross-validation)	136

Chapter 1

Introduction

The Sun, a star in the solar system center, is the energy source for life on Earth. It is a nearly perfect sphere of hot plasma, which makes the magnetic activities frequently occur across the solar surface. During this century, it has gradually become clear that many of the solar activities are related to the Sun's magnetic structure. The magnetic energy stored in the Sun can release through the solar eruption, causing severe space weather disturbance that influences the space-borne and ground-based technological systems, even human health. In particular, coronal mass ejections (CMEs) and solar flares are critical topics in solar physics since they are the main driver of space weather near the Earth. Therefore, to have a good understanding of these phenomena is a stated goal in the field of solar physics. To date, despite the observations that have revealed a great amount of the characteristics in these solar eruptions, it is still unclear what determines the initiation mechanism for the solar eruptions.

Before introducing the issues that will be investigated in the research, it is imperative to have a basic understanding of the solar eruptions as well as the achievements gained via the previous investigations. This chapter begins with an introduction for the overall characteristics of solar flares as well as CMEs (§1.1). §1.2 continues by describing a generally used model for analyzing the Sun's magnetic field and is followed by a review of various models for interpreting CME's initiation (§1.3). Finally, §1.4 addresses the problems and scientific objective that will be explored in this thesis.

1.1 Solar eruptions

Various solar eruptions occurring in the solar atmosphere, specifically solar flares and CMEs in this thesis, are strongly associated with each other. CMEs often follow flares (Munro et al., 1979, Sheeley Jr et al., 1983, Webb & Hundhausen, 1987) and it is commonly believed that CMEs and flares are the different manifestations of the same magnetic energy release process in the corona (see Cheng et al., 2010, Harrison, 1995, 2003, Lin & Forbes, 2000, Maričić et al., 2007, Priest & Forbes, 2002, Temmer et al., 2008, Zhang & Dere, 2006, Zhang et al., 2001), yet observations have shown that there is in fact not a one-to-one relationship between these phenomena, and it hinders our prediction for the impact of the Earth. In this era, thousands of scientific and commercial satellites are operating today, hence this question has gathered much attention.

A solar flare is a sudden release of energy from the Sun occurring at a time scale of minutes. The wavelength of the emission generated by flares can cover a large range of the electromagnetic spectrum. In 1859, R. C. Carrington and R. Hodgson independently witnessed one of the most intense solar flares (Carrington, 1859, Hodgson, 1859), which is reported as the localized, minute-long brightening on the Sun. When a solar flare occurs, the energy released is estimated to be about 10^{28} - 10^{32} erg; meanwhile, various observational signatures can be detected, such as radio wave burst and cosmic ray enhancement. The classification system for solar flares is according to the peak flux of soft X-rays (1 – 8 Å, SXR) as measured at the Earth by the *Geostationary Operational Environmental Satellite (GOES)* spacecraft. The classification is lettered by B, C, M, and X, which is outlined in Table 1.1, and X-class flares are the strongest of them all. Each class is further divided into a logarithmic scale from 1 to 9. Solar flares can occur everywhere on the Sun, but prefers to take place at Active Regions (ARs) with complex structure, especially for the extremely intense flares (*e.g.*, X-class flares).

Class	Peak of Soft X-ray Flux ($\text{erg cm}^{-2}\text{s}^{-1}$)
A	10^{-5}
B	10^{-4}
C	10^{-3}
M	10^{-2}
X	10^{-1}

Table 1.1: Classification of solar flares based on *GOES* X-soft ray observations.

A CME constitutes large-scale ejections of solar mass and magnetic flux from the lower corona into the interplanetary medium. Historically, CMEs are first identified by Tousey et al. (1973) and MacQueen et al. (1974). A “coronal transient” that traveled outward at over 1000 km/s is captured by the OSO-7 and Skylab coronagraphs, and it seems that no material falls back to the solar surface. Typically, the mass carried by a CME is estimated to be ranging in $1 \times 10^{11} - 4 \times 10^{13}$ kg, and averaged at 3×10^{12} kg (Gopalswamy & Kundu, 1992, Hudson et al., 1996, Jackson, 1985); furthermore, a CME can eject roughly 10^{23} Maxwell of magnetic flux to the interplanetary space (Gosling, 1990). The fundamental morphology of CMEs appears to be the so-called three-part structure in the coronagraph, which consists of a bright frontal loop in the outermost edge, a bright core in the inner part, and a dark cavity between them (Illing & Hundhausen, 1985, Saito & Hyder, 1968, Saito & Tandberg-Hanssen, 1973, Sturrock & Smith, 1968). However, the appearance of CMEs presented in the coronagraph could look very different from case to case, this is probably owing to the projection effects (Cremades & Bothmer, 2004). In Figure 1.1, a clear three-part structure was captured by a coronagraph. It is worth noting that many CMEs are associated with the prominence eruption (Gopalswamy et al., 2003, Jing et al., 2004). Filament (or prominence, when it appears above the solar limb) refers to a large, gaseous structure anchoring on the solar surface, extending outward the solar corona. The plasma constitutes prominence is usually cooler than the corona. The prominence is, therefore, seen as a dark stripe when projected on the solar disk. It is often regarded that part of the erupting filament becomes the bright core in the three-part structure; (House et al., 1981), yet observation shows that not every eruption is accompanied with a prominence.

CMEs and flares have been widely accepted to be regarded as two different manifestations of an identical energy-release event, observations also revealed that CMEs are usually accompanied by solar flares, yet the flare-less CMEs could occur. Several possible reasons for causing these flare-less CMEs might be (1) the CMEs are originating at the backside of the Sun; (2) the intensity of soft X-ray emitted by the accompanied flare is too weak to be identified as a solar flare (Hiei et al., 1993, Wu et al., 2002, Zhou et al., 2003). Conversely, it is observed that a significant portion of flares is CME-accompanying. The key property to trigger a CME is, therefore, remaining elusive. In terms of the flare-CME association, previous studies showed that the flares with higher peak flux in the SXR observation tend to be accompanied by CMEs (Andrews, 2003, Harrison, 1995, St. Cyr & Webb, 1991, Wang, 2002, Yashiro, 2005); it has also been indicated that flares with longer duration have a higher probability of being erupted with CME (Cui et al., 2018, Harrison, 1995, Kahler, 1992, Kahler et al., 1989). However, much of the so far investigation indicates that flare properties measured from *GOES* observations are not the only factor to be associated with the presence of the CME during an eruption. For instance, Harra et al. (2016) found that among 42 analyzed X-class

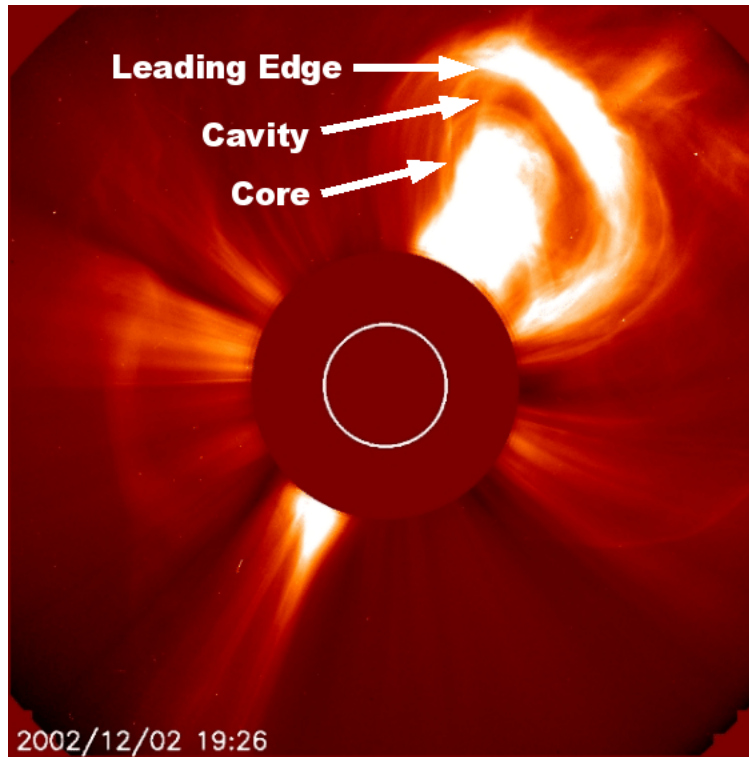


Figure 1.1: A CME captured by the Large Angle and Spectrometric Coronagraph Experiment (LASCO) onboard the Solar & Heliospheric Observatory (SOHO) is presented. The CME's three-part structure shows the leading edge, dark cavity, and bright core, as seen on December 2, 2002.

flares, there are not clear discriminators between the eruptive events and confined events when considering the event duration and *GOES* classification; Toriumi et al. (2017) statistically analyzed 51 $\geq M5$ -class flare events, finding that flare intensity and duration are not sufficient conditions to produce eruptive flares.

Certainly, the fundamental issue in all researches regarding solar eruptions deals with the eruption's origin: why and how magnetic reconnection takes place in the coronal magnetic field? It is believed that magnetic reconnection is a ubiquitous feature in the Sun's atmosphere. It is a physical process that converts magnetic energy to kinetic energy, thermal energy, and particle acceleration, which allows large-scale explosions occurring in the Sun's atmosphere. Figure 1.2 outlines the schematic diagram of magnetic reconnection; in the schematic, one can find that the magnetic reconnection involves two parts of ambient plasma with oppositely directed field lines moving towards each other into the diffusion region (shaded box in the center of Figure 1.2). The field lines in the

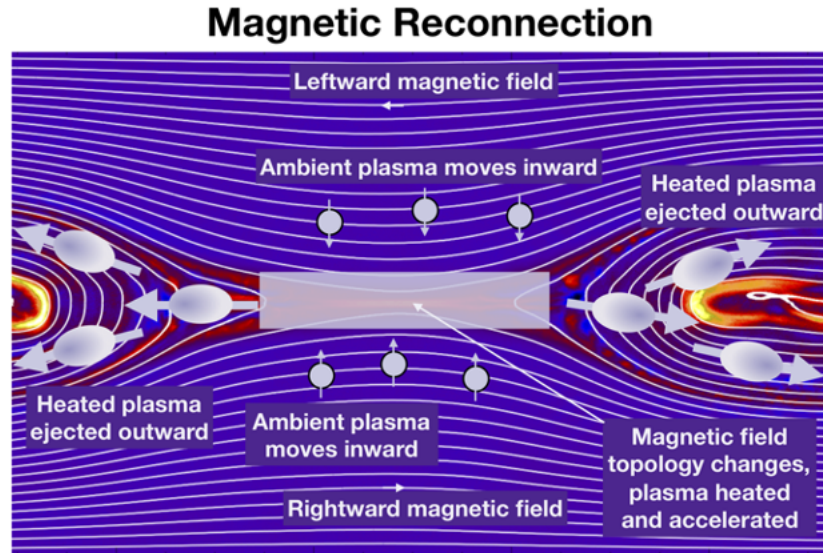


Figure 1.2: Schematic diagram of magnetic reconnection. The magnetic field lines in opposite directions (leftward at the upper region and rightward at the lower region), and the ambient plasma (light blue circles) moves towards the diffusion region (shaded box in the center). The plasma heated by the reconnection is ejected outward from the diffusion region after the reconnection process (reprinted from Hesse & Cassak, 2020).

diffusion region subsequently reconnect to the opposing halves. Following the reconnection process, the magnetic field topologically changes, the plasma is also heated and accelerated during the reconnection. To date, substantial evidences appeared during the flare eruption have denoted that magnetic reconnection could power solar eruptions; for instance, the cusp-shaped loops growing with time (Tsuneta, 1996), the plasmoid ejections (Shibata, 1998, Takasao et al., 2011), emission seen in magnetic arcades loops and loop tops (Masuda et al., 1994), and solar flare ribbons (Forbes, 2000, Qiu et al., 2012). The onset of a solar eruption is, therefore, confirmed to be strongly related to magnetic reconnection.

A magnetic flux rope (MFR) structure is regarded as the origin of the solar eruptions (see the review by Chen, 2011, Cheng et al., 2017, Filippov et al., 2015, and references therein). In general, an MFR describes a group of coherent twisted structures that wind around a common axis, usually found anchoring across polarity inversion lines (PILs) as viewed with photospheric maps of the solar magnetic field (Titov & Démoulin, 1999). A variety of models have indicated MFRs could form before or during the onset of solar eruptions. The observational manifestations of the preexisting MFR can be confirmed via the hot coronal loops presented in the passband corresponding

to hot temperature, such as 94 Å pass-band (Chen, 2011). Moreover, the filaments presented in the H α images have been theoretically demonstrated that they are kept by the helical magnetic configuration (Aulanier et al., 1998, Kuperus & Raadu, 1974, Priest et al., 1989, van Ballegoijen & Martens, 1989). Another candidate of the observational signature for an MFR could be the bald patch separatrix surface (BPSS; Gibson & Fan, 2006, Titov et al., 1993). BPSS is defined as the field lines that graze the photosphere at which magnetic connectivity is discontinuous, and it usually appears where the MFR just touches the photosphere. Fan & Gibson (2006) modeled the prominence as a twisted MFR, finding that a current sheet forms within the MFR cavity along with a BPSS, enclosing the helical field lines that support the filament. Moreover, the sigmoid, which refers to the S-shaped emission patterns showing in EUV and SXR observations, is also regarded as a signature of an MFR. The sigmoids could be formed with the heating in a curved current sheet at the interface between the helical field contained in an MFR and the ambient field (Kliem et al., 2004). The existence of MFRs inside CMEs can be verified in the coronagraph observations near the sun, which corresponds to the dark cavity shown in Figure 1.1 (Chen et al., 1997, Dere et al., 1999, Gibson et al., 2006, Riley et al., 2008, Vourlidis et al., 2013). When a CME escapes away from the solar surface, the in-situ solar wind measurements reveal that the counterpart of the CME in the interplanetary space are often comprised of helical “magnetic cloud”; the corresponding signatures include rotation of magnetic field, depressed proton temperature, and low plasma beta (Burlaga et al., 1981). These features have been demonstrated that they can be explained by a force-free MFR model (Lepping et al., 1990).

The CSHKP model generally accepted in the solar physics community (Carmichael, 1964, Sturrock, 1966, Hirayama, 1974, Kopp & Pneuman, 1976) is developed to understand the physical origins of solar eruptions. This model can integrate and interpret the signatures that have been detected in a solar eruption, providing a “standard picture” of an eruption event. The model depicted in Figure 1.3 summarizes the interrelationship between the various features that can be seen in a solar eruption. According to this model, magnetic reconnection occurs at a coronal loop anchoring on the solar surface, which manifests as the solar flares. Subsequently, a plasmoid with the closed magnetic field is formed above the reconnection spot and is pushed outwardly by the reconnection (Tsuneta, 1997), meanwhile post flare loops appear below the reconnecting point. The outflow jets from the reconnection spot (the heated plasma and accelerated particles origins from the magnetic reconnection) will emit Hard X-ray (HXR) at the top of the loops anchoring on the solar surface. Several studies have verified such emission (e.g., Hudson et al., 2001, Masuda et al., 1994). Moreover, the reconnection jets will stream down along the field lines into the chromosphere and the transition region below, causing emission with wavelengths in H α and (E)UV locating at the loop’s footpoints, respectively; the enhanced emission is known as flare ribbons. The plasma upflows/downflows can

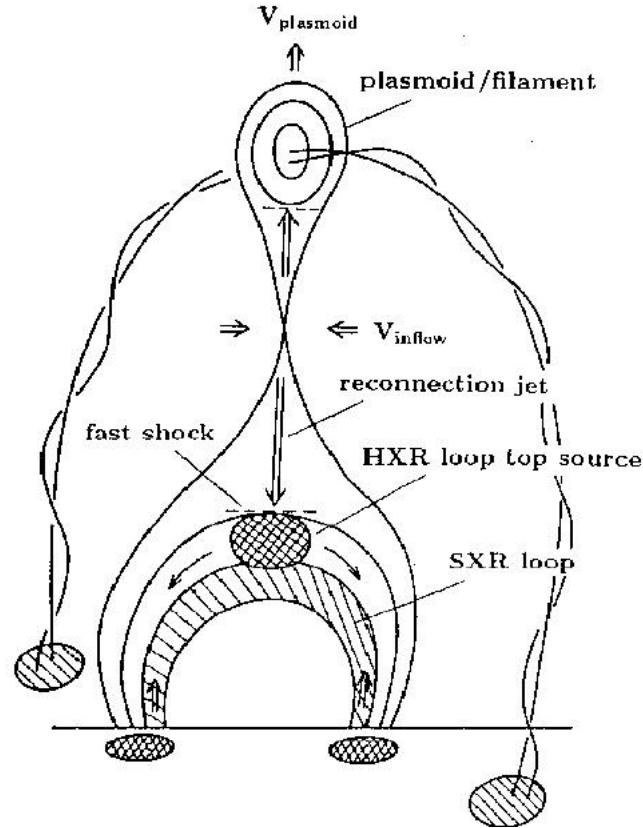


Figure 1.3: Schematic diagram of the CSHKP model of the magnetic field topology (solid lines) and major observed energy release processes in $H\alpha$, HXR, and SXR observations during a two-ribbon flare (reprinted from Shibata et al., 1995).

be seen in the spectroscopy, revealed as blueshift and redshift emission in the observations (e.g., Antonucci & Dennis, 1983, Milligan et al., 2006, Teriaca et al., 2006). As a consequence of the chromospheric heating, the material suffers from a pressure imbalance, piling up into the closed magnetic fields in the corona. Such a phenomena leads to the so-called chromospheric evaporation, and appears as the SXR emission that is usually observed as a cusp-shape geometry (e.g., Shibata & Magara, 2011).

Overall, it has been extensively confirmed through various observations that the CSHKP model can act as a standard model for describing the process of a solar flare; however, to explain the role of an MFR during an eruption, we need to extend the CSHKP model into a three-dimensional version, which has been proposed by many previous studies (e.g., Longcope et al., 2007, Priest &

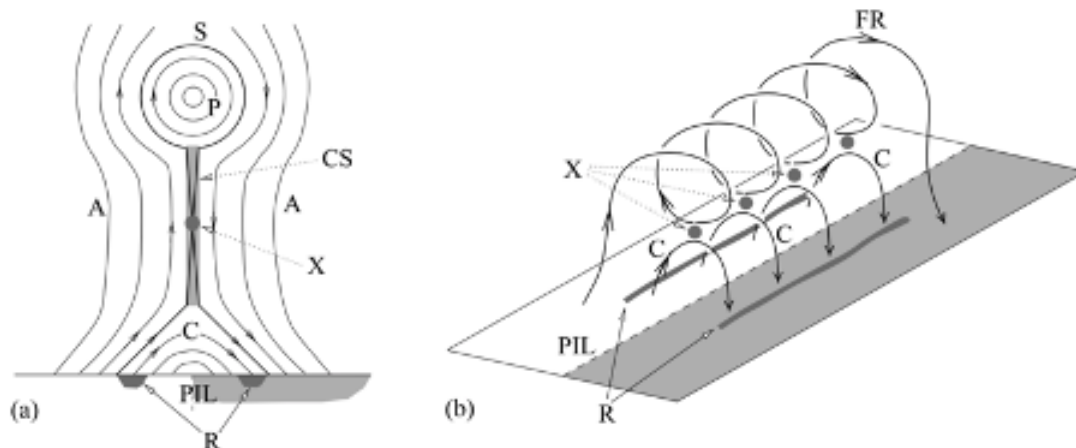


Figure 1.4: Basic elements of the CSHKP model in two (a) and three (b) dimensions. X denotes the reconnection points and c indicates the post-flare arcades. P stands for the plasmoid in the 2-D model, whereas it corresponds a twisted flux rope (FR) in the 3-D model. R represents the flare ribbons on the solar surface (reprinted from Longcope et al., 2007).

Forbes, 2002). The basic elements composing the CSHKP model in a 2-D and 3-D generalization are presented in Figure 1.4 (a) and (b), respectively. In the 3-D fashion, the whole erupting configuration is comprised of successive coronal loops, with every element shown in the 2-D version is elongated in the lateral direction. The reconnection is assumed to simultaneously occur among these loops, the MFR is, therefore, corresponding to the plasmoid shown in the 2-D version. One important application of the 3-D model is that it maps the morphology of the flare-ribbon patterns (Hoynig et al., 1981, Mariska et al., 1996) at the footpoint of the post-flare arcades, which is conjugating across the PIL; this property can be served as a good indication of where the MFR is locating. If prominence exists in this system, it is believed to thread through the bottom of the MFR (Kuperus & Raadu, 1974), but its presence is not necessary in the system.

At the present time, it is generally accepted that the CME can be considered as an erupting MFR system which can be outlined by the CSHKP model mentioned above. The schematic depicting the model of a CME is presented in Figure 1.5. The magnetic field configuration attaching to the solar surface is described by the CSHKP model. The MFR, which is denoted by the embedded cavity in the schematics, is locating at the upper part of the CSHKP model, driving the onset of the CME. The erupting MFR will form the CME in the observation. The MFR pushes the field lines straddling on it during the propagating, generating a leading shock ahead. If there is a prominence existing in the system, it will be dragged out by the embedding cavity, forming the brightening core

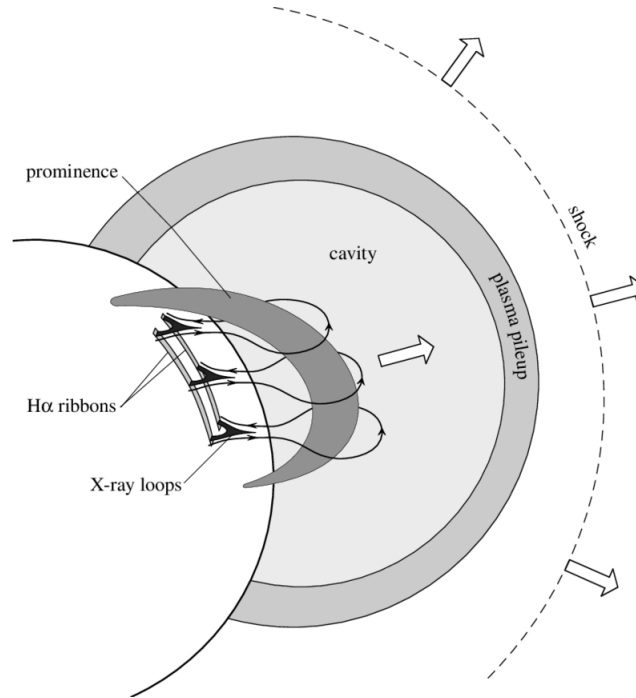


Figure 1.5: A schematic sketch shows the typical structure of a CME associated with a two-ribbon flare described by the CSHKP model. The plasma pileup (semi-circular shaded region) refers to the outermost circular brightening seen in the coronagraph (*e.g.*, leading edge shown in Figure 1.5). An MFR (corresponding to the area labeled with “cavity”) with a prominence (the dark semi-circular region) threading in the bottom is the main body of the CME (reprinted from Forbes, 2000).

part shown in the coronagraph (Low & Hundhausen, 1995).

With the big picture of the solar-eruption’s magnetic configurations is given, most of the observed phenomena can be successfully interpreted as the different aspects of an identical energy-release process; for instance, solar flares correspond to the brightness released during the reconnections, whereas CMEs correspond to the erupting MFRs. However, the observations have suggested that many flares are not with CMEs. Recalling that the CME eruption is described as an MFR undergoing an unstable state, there must be a certain *quantitative* method that can help us determine the state of stability for an MFR. For the sake of analyzing the solar eruptions quantitatively, information on the magnetic configuration in a 3-D framework would be required to perform further analysis. To do that, the so-called force-free magnetic field model, which is introduced in §1.2, is a good approach for us to infer the possible coronal magnetic structure.

1.2 Solar force-free magnetic field model

Currently, the routine measurement of the solar magnetic field is technically limited to photospheric observation, especially for the full-disk magnetogram. This is because the most widely used methods for measuring the solar magnetic field are based on the Zeeman effect, which is an effect that the spectral lines split due to interacting with an external magnetic field. Difficulties would arise in detecting the Zeeman effect at the area above the photosphere (*i.e.*, chromosphere and corona): the low plasma density lead to weak emission and absorption signals of the spectral lines, and the relatively low magnetic field strength can weaken the Zeeman signals. Due to the difficulties that might be met when directly detecting the chromospheric/coronal magnetic field, several alternative approaches to indirectly measure, by way of models, the magnetic field above the photosphere have been developed. For instance, extrapolation procedures with the photospheric magnetogram as the bottom boundary. To physically compute the extrapolation, the “force-free magnetic model” is proposed to model the coronal magnetic field.

ARs are assumed to be at an equilibrium state in the pre-eruption phase, which implies that the net force vanishes across the system. Regarding the possible source of the force, it is deemed that two kinds of forces are dominant in the Sun’s atmosphere, which are the magnetic-related force (Lorentz force) and the force generated from kinematic plasma flow pressure. Generally, other forces (*e.g.*, gravity force) are often neglected in the solar atmosphere. An important quantity must be introduced here is the plasma beta β , which is defined as the ratio of plasma kinetic pressure P_k and magnetic pressure P_B in a plasma:

$$\beta = \frac{P_k}{P_B} = 2\mu_0 \frac{P_k}{B^2}, \quad (1.1)$$

where P_k is the plasma pressure, B is the magnetic flux density, and μ_0 is the permeability of vacuum. The magnetic pressure (P_B) is calculated according to $P_B = \frac{B^2}{2\mu_0}$. At the region with β is extremely small, the magnetic pressure dominates over the plasma pressure, hence other non-magnetic forces are not considered over this region. With β , we are able to characterize the solar atmosphere based on its value: Figure 1.6 shows how the β value varies with height above the photosphere. The solar corona, at which the magnetic activities we are interested in occur frequently, host the value of $\beta \ll 1$ (Gary, 2001); this allows us to formulate the force balance in the corona as:

$$\mathbf{J} \times \mathbf{B} = 0, \quad (1.2)$$

where the current density is $\mathbf{J} = \frac{1}{\mu_0}(\nabla \times \mathbf{B})$, then:

$$(\nabla \times \mathbf{B}) \times \mathbf{B} = 0. \quad (1.3)$$

Such an approach is called the “force-free field approximation”.

So far, it is apparent that there are two kinds of magnetic field configuration can satisfy Equation (1.2), which are (1) current vanishes everywhere ($\mathbf{J} = 0$); or (2) current is parallel to the magnetic field ($\mathbf{J} \parallel \mathbf{B}$). In the case (1), Equation (1.3) turns into:

$$\nabla \times \mathbf{B} = 0. \quad (1.4)$$

The solution fulfills Equation (1.4) is called a potential field (\mathbf{B}_p), or current-free field, which is the simplest assumption for the coronal magnetic field. Here, with a potential scalar ϕ , \mathbf{B}_p can be expressed as:

$$\mathbf{B}_p = -\nabla\phi, \quad (1.5)$$

$$\nabla^2\phi = 0. \quad (1.6)$$

Equation (1.6) is a Laplace’s equation; therefore, the vertical component magnetogram data is required as the lower boundary condition to solve Equation (1.6) uniquely. Several methods have been proposed to extrapolate \mathbf{B}_p , for instance, Green function (Sakurai, 1982), Fourier method (Alissandrakis, 1981), and Potential Field Source Surface (PFSS; Altschuler & Newkirk, 1969). The potential field solution is fast and easy to compute; thus, it is a helpful tool for providing the first glance of the overall solar magnetic field. However, only when the actual solar magnetic field above the photosphere has remained stationary for a long time so that the coronal magnetic field is expected to be a potential field, which is often not the case, especially in the ARs with complex structures. Therefore the pre-erupt magnetic field structure, particularly the site where eruption occurs, is usually not consistent with the \mathbf{B}_p solution.

To take into account the energy that drives the eruption, we need a solution that enables the current flowing through the field which corresponds to the second case ($\mathbf{J} \parallel \mathbf{B}$). Such a magnetic field can be rewritten as:

$$\nabla \times \mathbf{B} = \alpha\mathbf{B}, \quad (1.7)$$

where α is a scalar function so-called force-free parameter. Next, we take the divergence of Equation (1.7) so the left hand side vanishes identically with the solenoidal condition ($\nabla \cdot \mathbf{B} = 0$):

$$\nabla \cdot (\alpha\mathbf{B}) = 0, \quad (1.8)$$

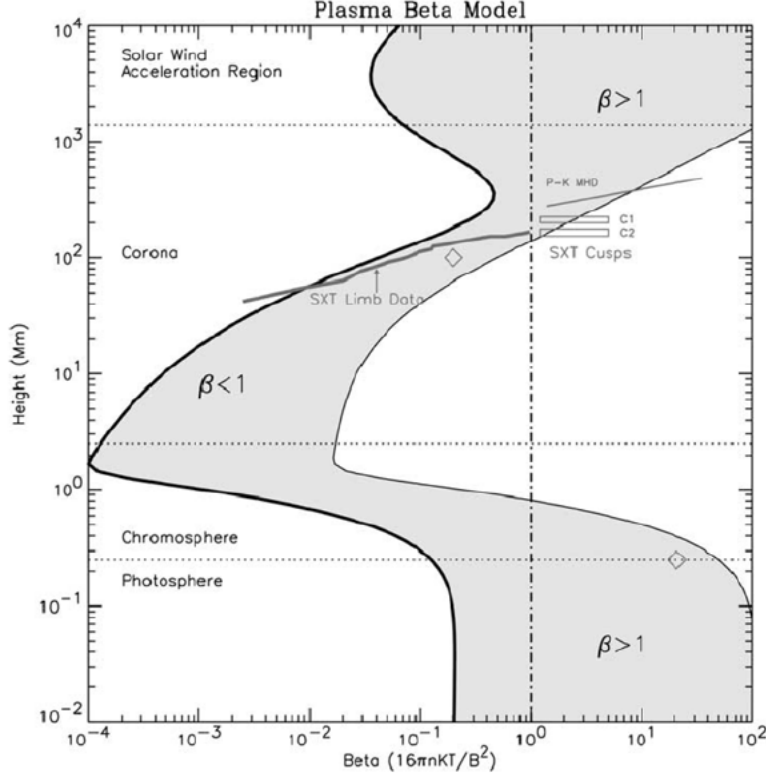


Figure 1.6: Plasma β model for an AR presented as a function of height above the photosphere. The range of the plasma β varies with height is shown shaded for open and closed field lines, which are originated from a sunspot (right solid line) and a plage region (left solid line). Horizontal dashed lines denote the approximated heights for the layers of the solar atmosphere (reprinted from Gary, 2001).

$$\alpha \nabla \cdot \mathbf{B} + \mathbf{B} \cdot \nabla \alpha = 0, \quad (1.9)$$

$$\mathbf{B} \cdot (\nabla \alpha) = 0. \quad (1.10)$$

Equation (1.10) implies that the α value is constant along each field line. To solve \mathbf{B} we need to take curl on Equation (1.7):

$$\nabla \times (\nabla \times \mathbf{B}) = \nabla \times (\alpha \mathbf{B}), \quad (1.11)$$

$$\nabla(\nabla \cdot \mathbf{B}) - \nabla^2 \mathbf{B} = \alpha(\nabla \times \mathbf{B}) + \nabla \alpha \times \mathbf{B}, \quad (1.12)$$

$$-\nabla^2 \mathbf{B} = \alpha^2 \mathbf{B} + \nabla \alpha \times \mathbf{B}. \quad (1.13)$$

When α takes the same value on each field line in the model, equation (1.13) becomes:

$$(\alpha^2 + \nabla^2)\mathbf{B} = 0. \quad (1.14)$$

Then, the solution of Equation (1.14) is called the linear force-free field (LFFF). The methods to derive LFFF include Green function (Chiu & Hilton, 1977) and Fourier method (Alissandrakis, 1981). When α is a function of location, it implies that each individual field line is assigned with a different α value. Equation (1.13) can, therefore, be rewritten into the form:

$$(\nabla^2 + \alpha^2)\mathbf{B} = \mathbf{B} \times \nabla\alpha. \quad (1.15)$$

The solution of Equation (1.15) is called the non-linear force-free field (NLFFF). It is worth noting that the case of $\alpha = 0$ corresponds to the solution of a potential field. Compared to the potential field, the advantage of LFFF and NLFFF is that they include the energy served as the driver of solar eruptions. As a result, using the LFFF or NLFFF model is expected to derive a more realistic solution which is in agreement with the measured magnetic structure; particularly, the magnetic configuration in the pre-erupt state is considered to be more representative with the NLFFF model. Although NLFFF seems to be the most suitable approach for analyzing the coronal magnetic field among all kinds of force-free models, the drawback of the NLFFF model is that the equation is non-linear; thus, it cannot be solved analytically, and some numerical techniques are required.

So far, various approaches have been developed to derive an NLFFF magnetic field solution. For instance, vertical integration method (Nakagawa, 1974, Wu et al., 1990); this method directly integrates the magnetic field upward in the vertical direction with the α value inferred from the photospheric measurement. Although the method is simple to implement, it is found to be ill-posed owing to no restrictions are imposed on the top and side boundaries (Wiegmann & Sakurai, 2012). The Grad-Rubin method (Sakurai, 1981), which has been improved by Amari et al. (2010) and Wheatland & Regnier (2009), is another technique to calculate NLFFF. In this method, the α inferred from the photospheric measurements is distributed according to the following equation:

$$\mathbf{B}^k \cdot \nabla\alpha^k = 0, \quad (1.16)$$

which is updated according to

$$\nabla \times \mathbf{B}^{k+1} = \alpha^k \mathbf{B}^k, \quad (1.17)$$

and

$$\nabla \cdot \mathbf{B}^{k+1} = 0, \quad (1.18)$$

where k is the iteration number and \mathbf{B}^0 is the potential field extrapolated based on the vertical

component magnetogram. The whole procedure is repeated until the magnetic field does not vary any more. Another widely used method is the so-called MHD-relaxation method (Metcalf et al., 2008, Schrijver et al., 2008, Wiegmann, 2008). The term “relaxation” comes from the concept that relaxing the unstable magnetic field toward the force-free state. In this thesis, we apply an MHD-relaxation method extended based on the scheme developed by (Inoue et al., 2014b), which is described in detail in §2.3.1.

1.3 CME-initialization model

The recognition that all the observed solar eruptions are manifestations of the same energy-release process is now generally accepted; however, one of the most important questions is still waiting for a conclusive answer: when a solar eruption occurs, what determines if an MFR can erupt away from the Sun? To date, there have been many attempts to answer this question.

First, we divide solar eruptions into two categories: in the case that there is only flares are detected during the solar energetic events, some studies refer to as “failed events”, or “confined events” as we use in this study (Moore et al., 2001), implying that an MFR (or coronal material) failed to escape from the solar surface (e.g., Alexander et al., 2006, Filippov, 2020, Ji et al., 2003, Kuridze et al., 2013, Kushwaha et al., 2015, Liu et al., 2009, Török & Kliem, 2005). Conversely, we refer to the event with CMEs are detectable as “eruptive events”.

Intuitively, a large amount of energy released during a solar eruption could imply that there has been more free energy stored in the MFR system, hence the CME is more likely to erupt. One could expect that a flare with higher peak SXR flux will have more probability to be accompanied by a CME since the X-ray intensity is one of the manifestations for the energy release. Previous studies showed that the eruptive events tend to have higher peak flux in the soft X-ray (SXR) observation (e.g., Andrews, 2003, Harrison, 1995, St. Cyr & Webb, 1991, Wang, 2002, Yashiro, 2005). In addition, a long-duration emission could also suggest that a relatively large amount of free energy has been released. Some studies have indicated that flares with longer duration have a higher probability of being eruptive events (e.g., Cui et al., 2018, Harrison, 1995, Kahler, 1992, Kahler et al., 1989). However, many exceptions indicate that flare properties measured from *GOES* observations is not associated to the CME-eruptivity of a flare. For instance, Harra et al. (2016) found that among 42 analyzed X-class flares, there are not clear discriminators between the eruptive events and confined events when considering the event duration and GOES classification; Toriumi et al. (2017) statistically analyzed 51 \geq M5-class flare events, finding that flare intensity and duration are not sufficient conditions to produce eruptive events.

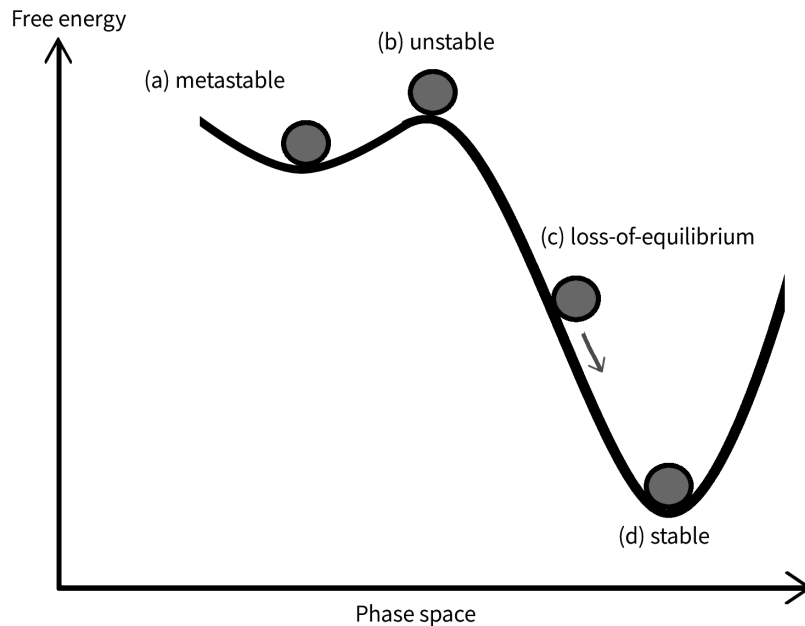


Figure 1.7: Schematic diagram of the evolution of a system moves from (a) a metastable state, through (b) a state of unstable, (c) the loss-of-equilibrium, and finally achieves the (d) stable state.

Instead of the *total energy* that has been stored and released during the eruption, an MFR’s mechanical equilibrium seems to play an important role when determining the CME’s eruptivity. The “free (magnetic) energy”, which is responsible for the solar eruption activities, can be used to quantify the equilibrium state of a certain magnetic structure. The free energy is theoretically defined as the energy contributed by the electric currents, thus the free energy is routinely estimated by subtracting the energy stored in the NLFFF (or LFFF) with the potential field. It is suggested that a magnetic field configuration with a large amount of free energy stored is susceptible to magnetic reconnection (Krall et al., 1982, Machado et al., 1988, Metcalf et al., 1995, Silva et al., 1996, Tanaka & Nakagawa, 1973); studies have also shown that non-potential structures are positively related to solar-eruption occurrence (*e.g.*, Jing et al., 2010, Thalmann & Wiegmann, 2008, Thalmann et al., 2008). The common features of free magnetic energy pile-up include shear and twist, hence the field lines with these profiles are usually considered non-potential, which are frequently found before the eruptions.

In the schematic illustrations showing the phase space of an MFR system (Figure 1.7), the free energy is shown as a function of the phase space transformation. The (a) *metastable* is a

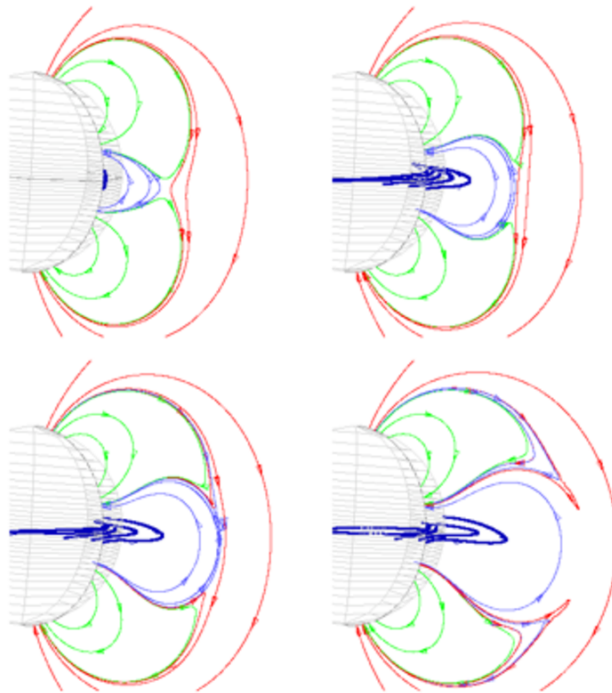


Figure 1.8: Schematic diagram of the magnetic breakout model (reprinted from Antiochos et al., 1999).

state at the local minimum of the free energy. Such a state is stable against small perturbations. With free energy continuously piling up in the system, the system gradually moves to the state of (b) *unstable*. At the above two states, magnetohydrodynamic (MHD) instability could destabilize the system, causing the energy release and triggering solar eruptions. When the energy is significantly piled up in a system, the system is away from an equilibrium state and more likely to erupt due to being more susceptible to magnetic reconnection. This state is called (c) *loss-of-equilibrium* (or *loss-of-stability*). Finally, the system achieves (d) a *stable* equilibrium state, corresponding to a global minimum of the free energy. In the context of the equilibrium state, an MFR can erupt under two kinds of conditions: (1) the system achieves the state of loss-of-equilibrium through accumulating sufficient free energy (Forbes, 2000); (2) the system is in the state of metastable or unstable equilibrium with adequate free energy, then the MFR is destabilized by the MHD instability (Sturrock et al., 2001).

To date, several models have been proposed to explain the scenario of an MFR's onset. One of the famous models is the so-called “break-out model” (Antiochos et al., 1999), as shown in

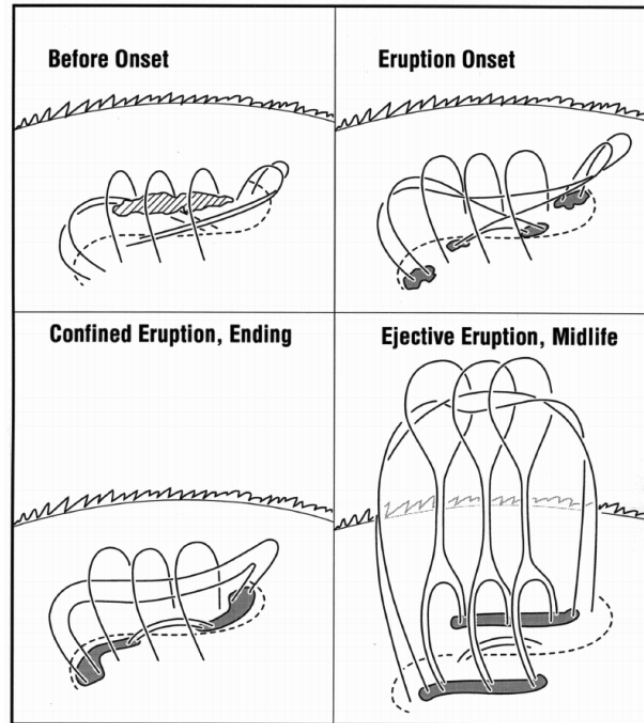


Figure 1.9: Schematic diagram of the tether cutting model (reprinted from Moore et al., 2001).

Figure 1.8. According to this model, a quadrupolar configuration with a null point is comprised of two bipole arcades and the overlying field with the same polarity, and one central bipole with the opposite polarity is between two low lying arcades. When the central flux system experiences a shear motion, the lifting of the flux system will subsequently suppress the overlying arcade, and then magnetic reconnection occurs at the null point above the shear arcade. The rising of the shear arcade and the accompanied reconnection can also form and erupt the MFR drastically. Such reconnection will weaken the straddling field lying on the MFR, facilitating the MFR’s ascending motion and producing CMEs. The observational evidence of the break-out model includes the null points above the source region (Aulanier et al., 2000) and the quadrupolar magnetic field evidenced by the locations of prominence (Tang, 1987); moreover, many numerical studies have applied this model for analyzing solar eruptions (*e.g.*, Archontis & Török, 2008, Doyle et al., 2019, MacTaggart & Hood, 2009, Wyper et al., 2018). Even though the break-out model is feasible to explain the formation of CMEs, the “onion-peeling” reconnection does not guarantee that the MFR can successfully escape from the solar surface; the confined case might occur when the overlying

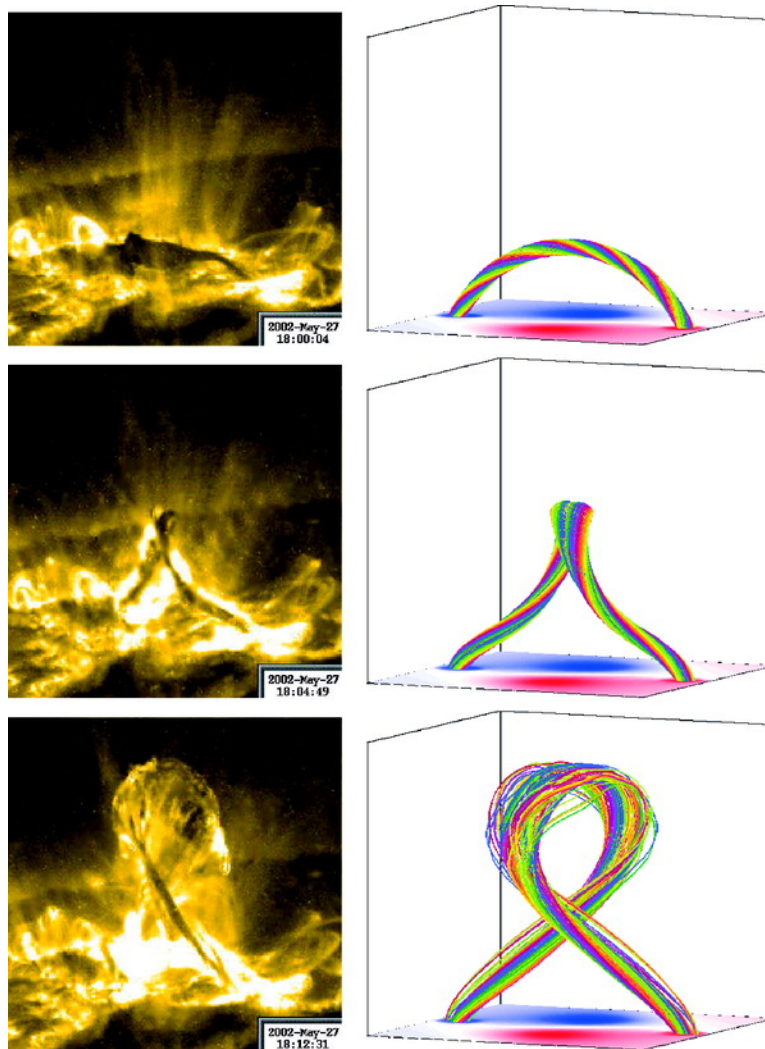


Figure 1.10: Right panels: Simulation of the kink instability in the sun; left panels: observations by *TRACE* 195 Å (reprinted from Török & Kliem, 2005).

flux is strong enough to constraint the lifting core (Guo et al., 2010). Another famous model is the so-called “tether-cutting model” (Moore et al., 2001), which has been supported by some coronal observations (e.g., Chen et al., 2014, Liu et al., 2013, Xue et al., 2017). Figure 1.9 depicted the scenario of the reconnection. In this model, the strongly shear magnetic arcades are almost aligning with the PIL, with the potential-like envelope magnetic arcades overlying on them. The tether-cutting reconnection occurs between the two sheared arcades, forming and erupting an MFR above

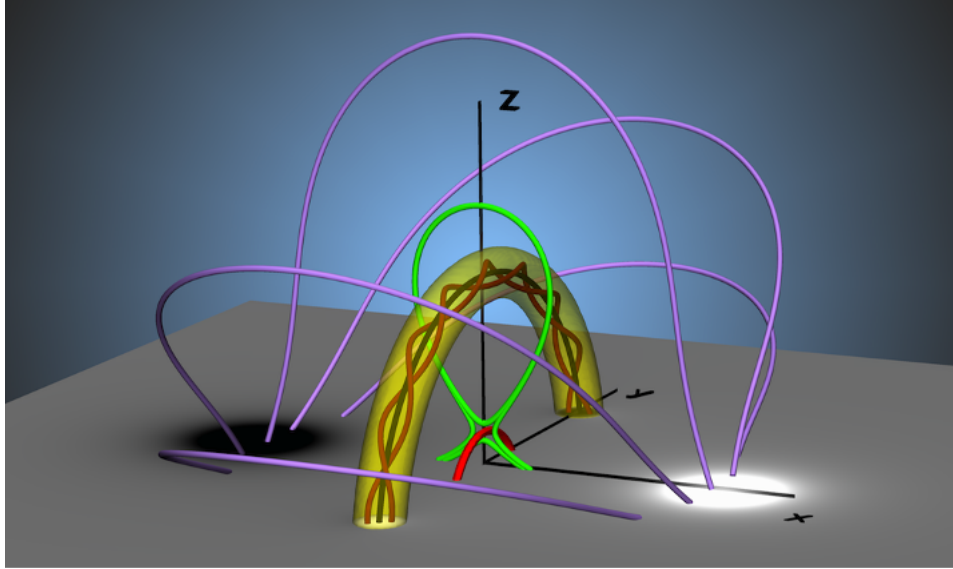


Figure 1.11: Titov-Démoulin model comprises of a flux rope (current channel) and the overlying field (reprinted from Kliem et al., 2014).

the reconnection spot. Following the reconnection outflow, the foot-fieldlines connecting the MFR is elongated outwardly and being straddling by the overlying magnetic. If the overlying magnetic is strong enough, then the eruption becomes confined (with no CME is detected); in contrast, if the overlying field is too weak to hold the rising MFR, then the CME erupts.

In the breakout model and the tether-cutting model, the pre-eruption magnetic structure is a sheared core field instead of a helical MFR. However, the sheared core field is believed to reconnect into an MFR during the eruption. Although both models can conceptually explain why a flare is seen without the following CMEs, they do not indicate the threshold that leads to the instability of the associated MFR. Acting as an efficient way to transfer an MFR to the loss-of-equilibrium state, MHD-instability is frequently discussed when arguing the stability of the MFR; especially, it provides a way to *quantitatively* determine the state of stability for an MFR.

The Kink Instability (KI; Rust & Kumar, 1996, Sakurai, 1976) describes that when the magnetic twist (winding of magnetic field lines around an axis) in an MFR exceeds a critical value, the twist abruptly converted to magnetic writhe (the winding or deforming of the axis itself), and the MFR will erupt. The numerical study of the KI is shown to be able to reproduce the observed erupting MFR, as shown in Figure 1.10. The necessary twist for triggering the instability has been denoted to between 2π to 6π when the line-tying effect is under consideration (Hood & Priest, 1979).

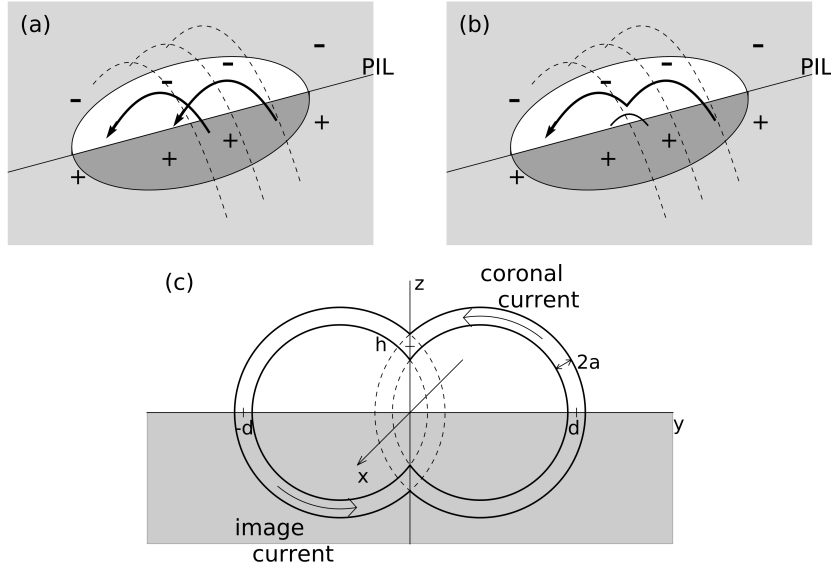


Figure 1.12: Schematic diagram of the double arc instability (reprinted from Ishiguro & Kusano, 2017).

Nevertheless, KI does not consider the effect of the external field, which may provide additional confinement to the MFR. Falconer et al. (2002) analyzed several global nonpotentiality measurements and their corresponding correlations to the CME productivity, finding that the larger global twist indicates higher CME productivity. However, Leamon et al. (2003) used the mean value of the force-free parameter as a proxy for the twist in their prediction method, and they found that it was not a sufficient condition for producing CMEs. The Torus Instability (TI; Démoulin & Aulanier, 2010, Kliem & Török, 2006) assumes that a semi-circular current is located where the magnetic field gradually decays with height. When the MFR has ascended to a height where the external magnetic field decreases quickly enough than a certain criterion, the ring current would be destabilized by the TI and experience an ascending motion. Figure 1.11 presents a Titov-Démoulin model, which comprises a toroidal MFR (current channel) and the overlying field lines. In this circuit system, the equilibrium is achieved by the balance of downward Lorentz force coming from the external magnetic field and hoop force generated from the ring current (Titov & Démoulin, 1999). The decay rate of the background field is characterized by the so-called “decay-index” (n),

which is defined as:

$$n = -h \frac{\partial \ln B}{\partial \ln h}, \quad (1.19)$$

where h denotes the height measured from the solar surface, and the corresponding threshold is given by $n > 1.5$ (Bateman & Grimm, 1979, Kliem & Török, 2006). To date, TI has been extensively used by numerous researchers discussing the CME-initiation mechanism (*e.g.*, Baumgartner et al., 2018, Fan & Gibson, 2007, Guo et al., 2010, Inoue et al., 2013, Jing et al., 2015, Liu, 2008, Nindos et al., 2012, Wang et al., 2017). It is worth noting that Myers et al. (2015) performed a laboratory experiment which presents a comprehensive analysis of the stability host by MFRs against KI and TI simultaneously. Also, its observational counterpart has been investigated by Jing et al. (2018). These studies revealed that some MFRs could be failed-torus, which means MFRs are kink-stable but have exceeded the torus threshold and fail to erupt. The results imply that TI is probably not a sufficient condition for an MFR's eruption.

Another recently proposed MHD instability is the Double Arc Instability (DAI; Ishiguro & Kusano, 2017). DAI aims to investigate the instability of a double-arc loop formed through the tether-cutting reconnection placing in a toroidal magnetic field. DAI is a counterpart of TI; thus, the equilibrium state is also achieved by the force balance of the suppression arising from the external field and the hoop-force originating from the loop. Figure 1.12 demonstrates the basic settings of the double-arc loops, where the loop is characterized by the height of the joint point (h) *i.e.*, the height where two semi-circular loops connect. Ishiguro & Kusano (2017) indicates that this double-arc loop is unstable when a parameter κ exceeds a certain threshold. Here, κ is defined as

$$\kappa = T_w \frac{\phi_{\text{rec}}}{\phi_{\text{tot}}}, \quad (1.20)$$

where T_w is the twist of a magnetic loop and $\phi_{\text{rec}}/\phi_{\text{tot}}$ is the fraction of the reconnected flux over the total flux crossing over the considered PIL. A previous study showed that the threshold of κ is in the range of 0.08 to 0.175, depending on the configuration of the external magnetic field. Compared to TI, the ring current is found to be more easily to erupt in DAI; Ishiguro & Kusano (2017) found that the double-arc loop can even become unstable in the background field without magnetic strength decreasing. Muhamad et al. (2018) verified the DAI with the observations combining the NLFFF extrapolation, showing the feasibility of DAI in determining the eruption's onset condition.

Overall, we have introduced several fundamental models above, which are related to our research, in this section. One can realize that the models mentioned above are almost the same in nature: they are based on the MFR's interrelation with the immediate vicinity. As a result, correctly identifying the location and volume of a MFR may help us deduce CME's triggering mechanism.

With an overview of the so far progress regarding the CME's generation, we content to propose the motivation and objective of this study in the next subsection.

1.4 Motivation and scientific objective

Even though the aforementioned MHD instabilities are feasible to provide a picture of the CME triggering mechanism, it is still challenging to analyze actual ARs by applying these theories. The issue of whether these models are feasible to analyze the realistic observations arouses our scientific interests. Here, we address several fundamental problems regarding the observational analysis of the CME-initialization mechanisms.

First, there is still no specific definition of an MFR; it is, therefore, nontrivial to accurately identify an MFR from a magnetic field construction, as well as subsequently quantifying the reconnected flux related to it. Flare-ribbon-related brightening could be a good indication of MFRs; however, flare ribbons only appear after the eruption's onset, which provides no information regarding the erupt-imminent structure. Presently, approaches used to infer the presence of an MFR and estimate the amount of event-related magnetic reconnection are based primarily on the magnetic twist number. For instance, Muhamad et al. (2018) used the magnetic flux associated with field lines displaying twist over a certain threshold as the approximation of the reconnected flux contributed by an MFR. Duan et al. (2019) and Liu et al. (2016) rendered a channel with the twist number over a certain threshold as the representation of MFRs. Signatures of MFRs in magnetic field structures can be based on a topological definition, such as requiring bald patch separatrix surface (Gibson & Fan, 2006); this definition was applied by Green & Kliem (2009) to interpret the soft X-ray sigmoid observation. Additionally, Pagano et al. (2019) proposed the "flux rope ejection metric" which includes an estimate of both magnetic field twist and Lorentz force, to evaluate the possibility of an MFRs' presence. In short, identifying the signatures of MFRs before solar eruptions is still under debate, with numerous methodologies under investigation, especially for the question of identifying the frontier that separates an MFR itself from its immediate environs and their respective contribution to the eruption.

Second, another important question is how to separate the *real* strapping field acting on MFRs from the non-interacting field in the observation data? A simplified way is to take the magnetic field across the entire AR as the confinement source, which was used by Toriumi et al. (2017). Without considering the real geometry of an MFR, some studies used height to divide the MFR regime from its immediate surrounding since the MFR is supposed to be located in a lower height (Cheng et al., 2011, Liu, 2008, Sun et al., 2015, Thalmann et al., 2015, Wang & Zhang, 2007). However, it seems

that these approaches are probably not robust to estimate the instability, owing to the fact that only the toroidal field strapping on the MFR is theoretically responsible for the confinement based on MHD instabilities. When estimating the decay index across a domain, the general approach approximates the background by the potential field extrapolated from the magnetogram. The strapping field is routinely estimated by the horizontal component of the potential field (*e.g.*, a similar approach was made by Chintzoglou et al., 2017, Jing et al., 2018). Besides, Duan et al. (2019) improved the method by a more specific estimation of the decay index. First, the direction of an MFR’s ejection is identified by examining the solar coronal observations. The decay index is then calculated aligned with this trajectory, which is the direction that the straddling force is expected to apply. To sum up, how to correctly find the magnetic field that is really strapping the target MFR is still an issue that remains unclear.

Third, another feature that has not been considered in the TI or DAI is the magnetic field’s topology, which may be crucial for an event’s eruptivity. Some studies suggest that an open-field structure can facilitate the lifting of an MFR and lead to the formation of CMEs; as opposed to a closed configuration that will instead “strap down” a rising MFR. For instance, DeRosa & Barnes (2018) found that the intense flares ($\geq X$ -class) tend to occur with CMEs in ARs near open magnetic field-line bundles. Thalmann et al. (2015) studies a confined-event productive AR, suggesting that the nearby open field may facilitate the CME eruption. Furthermore, Chintzoglou et al. (2017) analyzed the magnetic field during a failed eruption event, suggesting that the topology of the ambient magnetic destroys a rising MFR-like structure. Hence, we believe that the magnetic field’s geometrical profiles also play an essential role in determining an eruption’s eruptivity.

In response to the three fundamental questions mentioned above, the major objective of this study is to propose a new parameter that may be used to evaluate the capability of generating CMEs. The parameter will require the topological information of magnetic field structures, and it is based on the balance between the ascending force and the suppression force working on the MFR. In this work, we present a full statistical approach, demonstrating that this newly proposed parameter is capable of characterizing an AR that can generate an eruptive event.

Chapter 2

Event List, Data, and Method

In the previous chapter, we have introduced the physical subject of this work, which is to study the initialization of coronal mass ejections (CMEs) in the context of solar flares; the approaches to derive the pre-event information of the coronal magnetic field is, therefore, required in this study. Before presenting the process of the analysis and results of our works, it is necessary to describe the methods and data used in this work, which allows us for a convenient description of the analysis.

The event list used in this study is shown in §2.1. The tools applied in this study includes observational data provided by NASA’s spacecraft *Solar Dynamics Observatory* (SDO) and an extrapolating technique based on the nonlinear force-free field (NLFFF) model. These methods are outlined in §2.2 and §2.3, respectively. With these approaches, we derive the coronal magnetic field data of all energy-release events in the event list, analyzing their pre-event magnetic configurations. Furthermore, we carry out the linear discriminant analysis introduced in §2.4 to relate the CME-triggering mechanism to the magnetic field properties of active regions (ARs).

2.1 Event list

In this study, we use the event list originally proposed by Toriumi et al. (2017). The data set was initiated by selecting the major flares that occurred in the period 2010 May to 2016 April. These flares all have *GOES* SXR peak magnitudes in 1-8 Å bandpass $\geq 5 \times 10^{-5} \text{W} \cdot \text{m}^2$ (M5.0). To reduce the effects from distortions due to projection effects, Toriumi et al. (2017) only included the events located within 45° of disk center. Finally, 51 flare events from 29 active regions are arranged in Table 2.1. The CME association of each events are determined by reference to the CME

catalog provided by the Solar and Heliospheric Observatory (SOHO)/Large Angle Spectroscopic Coronagraph¹. The eruptive events are identified such that the CME onset time derived from the linear fitting to the height-time measurement according to the catalog reasonably agrees with the flare onset time. Among these 51 flare events, 33 flares are eruptive and 18 events are confined. The CME-association of each event is also presented in Table 2.1. Toriumi et al. (2017) indicated that the flare-ribbon magnetic flux normalized to the flux in the entire AR could somehow distinguish the eruptive and confined events. This finding motivates the major part of this research –which is to study the CME-eruptivity based on the balance between the non-potential structure and the surrounding confinement. In this study, we attempt to refine the definition for estimating the balance and demonstrate our proposed scheme’s feasibility by comparing to the results shown in Toriumi et al. (2017). As a result, we apply an identical event list for presenting a comparative result.

¹https://cdaw.gsfc.nasa.gov/CME_list/

Event#	GOES Start Time ^a	GOES Class ^b	Position ^c	NOAA# ^d	CME ^e
1	2011-02-13T17:28	M6.6	S20E05	11158	Y
2	2011-02-15T01:44	X2.2	S20W10	11158	Y
3	2011-03-09T23:13	X1.5	N08W11	11166	N
4	2011-07-30T02:04	M9.3	N14E35	11261	N
5	2011-08-03T13:17	M6.0	N16W30	11261	Y
6	2011-08-04T03:41	M9.3	N16W38	11261	Y
7	2011-09-06T01:35	M5.3	N13W07	11283	Y
8	2011-09-06T22:12	X2.1	N14W18	11283	Y
9	2011-09-07T22:32	X1.8	N14W31	11283	Y
10	2012-01-23T03:38	M8.7	N33W21	11402	Y
11	2012-03-07T00:02	X5.4	N18E31	11429	Y
12	2012-03-07T01:05	X1.3	N15E26	11429	Y
13	2012-03-09T03:22	M6.3	N15W03	11429	Y
14	2012-03-10T17:15	M8.4	N17W24	11429	Y
15	2012-05-10T04:11	M5.7	N12E22	11476	N
16	2012-07-02T10:43	M5.6	S17E06	11515	Y
17	2012-07-04T09:47	M5.3	S17W18	11515	N
18	2012-07-05T11:39	M6.1	S18W32	11515	N
19	2012-07-12T15:37	X1.4	S13W03	11520	Y
20	2013-04-11T06:55	M6.5	N07E13	11719	Y
21	2013-10-24T00:21	M9.3	S09E10	11877	Y
22	2013-11-01T19:46	M6.3	S12E01	11884	Y
23	2013-11-03T05:16	M5.0	S12W17	11884	N
24	2013-11-05T22:07	X3.3	S12E44	11890	Y
25	2013-11-08T04:20	X1.1	S13E13	11890	Y
26	2013-11-10T05:08	X1.1	S13W13	11890	Y
27	2013-12-31T21:45	M6.4	S15W36	11936	Y
28	2014-01-07T10:07	M7.2	S13E13	11944	N
29	2014-01-07T18:04	X1.2	S12W08	11944	Y
30	2014-02-04T03:57	M5.2	S14W07	11967	N
31	2014-03-29T17:35	X1.0	N10W32	12017	Y
32	2014-04-18T12:31	M7.3	S20W34	12036	Y
33	2014-09-10T17:21	X1.6	N11E05	12158	Y
34	2014-09-28T02:39	M5.1	S13W23	12173	Y
35	2014-10-22T01:16	M8.7	S13E21	12192	N
36	2014-10-22T14:02	X1.6	S14E13	12192	N
37	2014-10-24T21:07	X3.1	S22W21	12192	N
38	2014-10-25T16:55	X1.0	S10W22	12192	N
39	2014-10-26T10:04	X2.0	S14W37	12192	N
40	2014-10-27T00:06	M7.1	S12W42	12192	N
41	2014-11-07T16:53	X1.6	N17E40	12205	Y
42	2014-12-04T18:05	M6.1	S20W31	12222	N
43	2014-12-17T04:25	M8.7	S18E08	12242	Y
44	2014-12-18T21:41	M6.9	S11E10	12241	N
45	2014-12-20T00:11	X1.8	S19W29	12242	Y
46	2015-03-10T03:19	M5.1	S15E39	12297	Y
47	2015-03-11T16:11	X2.1	S17E22	12297	Y
48	2015-06-22T17:39	M6.5	N13W06	12371	Y
49	2015-06-25T08:02	M7.9	N12W40	12371	Y
50	2015-08-24T07:26	M5.6	S14E00	12403	N
51	2015-09-28T14:53	M7.6	S20W28	12422	N

^a The start time of the flare according to *GOES* catalog.

^b Flare class from the *GOES* flare catalog.

^c Flare location from the *GOES* flare catalog.

^d Active region number assigned by NOAA.

^e Y: eruptive event; N: confined event

Table 2.1: Event list for analysis.

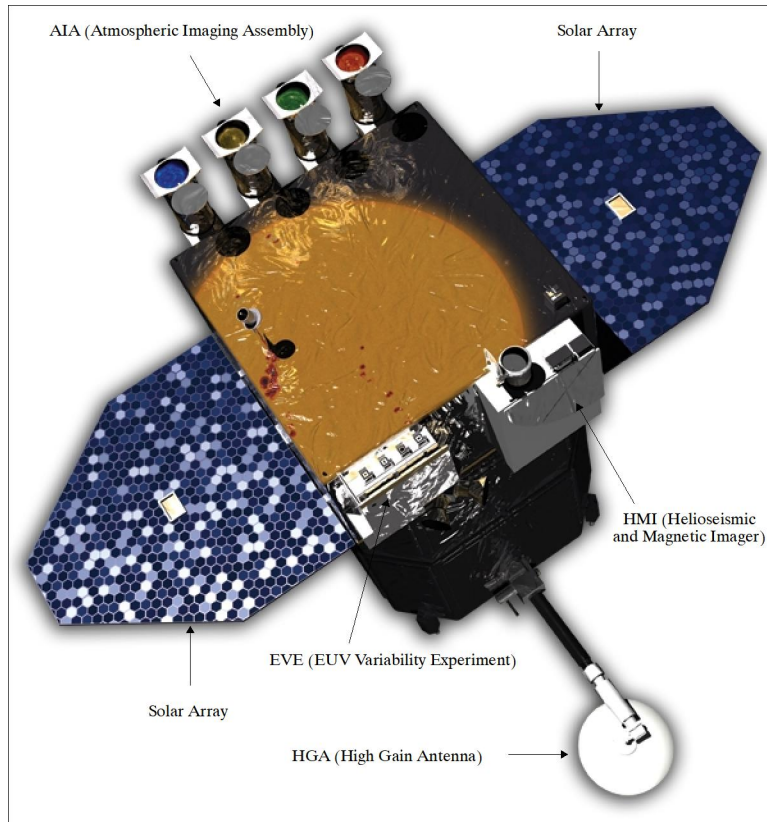


Figure 2.1: Top view of the Solar Dynamics Observatory spacecraft (credit: NASA).

2.2 SDO spacecraft

SDO is a solar observation mission launched by NASA in February 2010, aiming to understand the Sun's influence on the Earth and near-Earth space. SDO is located at the Geosynchronous orbit, at which the Earth-to-Sun observation is available continuously in contact with its ground station in New Mexico, USA. The instruments onboard SDO include the *Helioseismic and Magnetic Imager* (HMI; Schou et al., 2012), the *Atmospheric Imaging Assembly* (AIA; Lemen et al., 2011), and the *Extreme Ultraviolet Variability Experiment* (EVE; Woods et al., 2010), which are shown in Figure 2.1. The HMI and the AIA data are mainly used in the analysis; thus, we will focus on these two instruments in this section.

The HMI instrument is designed to measure polarization states Stokes vectors $\mathbf{I} = (I, Q, U, V)$ using the Zeeman effect, where I stands for the total intensity; Q and U quantify the linearly

polarized fraction of an electromagnetic wave; and V describes the circular polarization. The HMI full-disk measurement is with the resolution of $1''$ per pixel using the 6173 \AA Fe I spectral line.

In this thesis, special emphasis is given to the magnetogram translated from the detected polarized light. The line-of-sight magnetogram is one of the HMI data products; it is available at a 45-second cadence (`hmi.M_45s`) and a 12-minutes cadence (`hmi.M_720s`). The Spaceweather HMI Active Region Patches (SHARPs) is a more advanced product generated by automatically tracking each AR as it rotates across the face of the solar disk. The SHARP data is calculated from the photospheric vector magnetogram data and produced at a 12-minute cadence. The process to generate the vector magnetogram data is achieved by using the Very Fast Inversion of the Stokes Vector code, which assumes a Milne-Eddington model of the solar atmosphere (Borrero et al., 2011). The 180° ambiguity in the transverse component of the image-plane vector is resolved using a minimum energy algorithm (Leka et al., 2009, Metcalf, 1994). For the `hmi.sharp_cea_720s` data series, the vector magnetic field data has been remapped to a Lambert Cylindrical Equal-Area (CEA) projection and decomposed into B_r , B_θ , and B_ϕ components and their associated uncertainty estimations. Another featured HMI product is the HMI synoptic charts (Liu et al., 2017), which are mainly used to represent a full sphere with magnetic vectors on the photosphere. Synoptic charts are produced using 12-minute cadence full-disk vector magnetograms remapped to Carrington coordinates. The full resolution of such a synoptic chart is 3600×1440 pixels. The horizontal axis corresponds to the longitude in degrees, where the vertical axis is co-aligned in sine latitude.

In this study, the magnetic field measurement obtained by the HMI is used as the input of the coronal field extrapolation. Particularly, SHARP data and HMI synoptic charts enable us to analyze the coronal field in a spherical coordinate, which is a proper way of constructing the solar coronal magnetic field.

The AIA instrument is an imager, which consists of four generalized Cassegrain telescopes. Each of the telescope can detect photons by CCD chips with 4096×4096 pixels. AIA can provide full-disk observations of the Sun's atmosphere in multiple wavelengths at $1.5''$ spatial resolution and 12-second cadence, except for the observations of the ultraviolet channels, which are at 24-second cadences. Table 2.2 lists the major emission lines observed by AIA and their characteristic emission temperatures, and the region of solar atmosphere at which the ions may be observed. With the observations taken at a variety of bandpasses, the AIA enables us to observe the Sun's atmosphere with coverage from the solar chromosphere to the solar corona. For the sake of examining the topology of the coronal magnetic structure and confirming the validity of our extrapolated coronal model field, we include the observation of the plasma in corona obtained by AIA instrument equipped on SDO, particularly for the 171 \AA and 94 \AA , which captures the geometries of the coronal loops

outside the core region and the flaring coronal loops, respectively. Moreover, the measurement in 1600 Å bandpass is implemented in this thesis to map the solar-flare-ribbon related locations and extent.

Channel	Primary ion(s)	Region of atmosphere	Characteristic temperature log(T)
4500 Å	continuum	photosphere	3.7
1700 Å	continuum	temperature minimum, photosphere	3.7
304 Å	He II	chromosphere, transition region	4.7
1600 Å	C IV + cont.	transition region, upper photosphere	5.0
171 Å	Fe IX	quiet corona, upper transition region	5.8
193 Å	Fe XII, XXIV	corona and hot flare plasma	6.2, 7.3
211 Å	Fe XIV	active-region corona	6.3
335 Å	Fe XVI	active-region corona	6.4
94 Å	Fe XVIII	flaring corona	6.8
131 Å	Fe VIII, XXI	transition region, flaring corona	5.6, 7.0

Table 2.2: The wavelength channels of AIA and the the primary emission lines observed by AIA (the information listed in this table is adopted from Lemen et al. (2011)).

The SDO data described in this chapter is available on Joint Science Operations Center (JSOC)² at Stanford University. One can also find more information about the data and download data on the JSOC database.

2.3 Coronal magnetic field construction

In order to investigate the magnetic field structure that favors CME's onset, the information of the three-dimensional magnetic configurations in the Sun's atmosphere is required in this research, particularly the magnetic field data at the pre-event phase. Progress in analyzing explosive phenomena has been highly dependent upon the constructed coronal field, which is routinely calculated by extrapolating the photospheric magnetic field. In the previous section, we have provided an overview

²<https://jsoc.stanford.edu/>

of the photospheric magnetogram data measured by the SDO spacecraft. Here, continuously, we describe the detail of the extrapolating technique that will apply on the SDO magnetograms, which is the aforementioned *MHD-relaxation method*, as well as the relevant validations for the yielded NLFFF model data.

2.3.1 MHD relaxation method

MHD relaxation method means an initial non-equilibrium state is relaxed toward an equilibrium state. In the case of NLFFF extrapolation, the method does not apply any NLFFF equation directly; instead, it evolves the initial magnetic field until the final state at which all the boundary conditions are fulfilled. Mikic et al. (1988) first applied this procedure to derive the NLFFF; Jiang & Feng (2012), McClymont & Mikic (1994), Mikic et al. (1988) then utilized the potential field as the initial state for driving the relaxation. Of note, the MHD relaxation method does not guarantee a unique NLFFF solution. Also, for any given initial field, it cannot ensure that there is a force-free state to which the field can relax. Therefore, validation of the resulting NLFFF is necessary such that further analysis based on it is practical. In this thesis, we use a scheme of MHD-relaxation method developed by Inoue et al. (2014b), which solves a set of resistive MHD-like equations and derive the NLFFF solution of the coronal magnetic field through a fitting process. In this study, the method was extended to work in spherical coordinates as required for this study.

The MHD-relaxation method performed in this study requires the vector magnetogram as the lower boundary condition. The input magnetic vector data is the three components of the magnetic field (B_r , B_θ , B_ϕ), where the SHARP CEA magnetogram and the HMI synoptic charts are used in this study. As the synoptic charts are generated after every Carrington Rotation (~ 27 days) is completed, we replace the target region with the SHARP data to ensure accuracy within the area under immediate consideration. The vertical component is used for extrapolating the potential field, and the horizontal components are used as the constraint during the relaxation process. Figure 2.2 demonstrates the technique used in this study to construct the lower boundaries for the PFSS model. First, we take a SHARP magnetogram of the target AR and lower its spatial resolution to be consistent with the HMI synoptic chart by using `BILINEAR` in IDL. Then, we take two HMI synoptic charts. One covers the target AR, and another one covers the next Carrington rotation when the Carrington longitude of the target AR's center is less than 180° (using the synoptic chart at the one Carrington rotation before when the longitude of the target AR is $> 180^\circ$). At this step, the two synoptic charts are put into a single synoptic map that covers 360° in longitude with the target AR is placed at the center (as shown in Figure 2.2 (c)). This modified HMI synoptic map is served as the lower boundary of the PFSS model in this study.

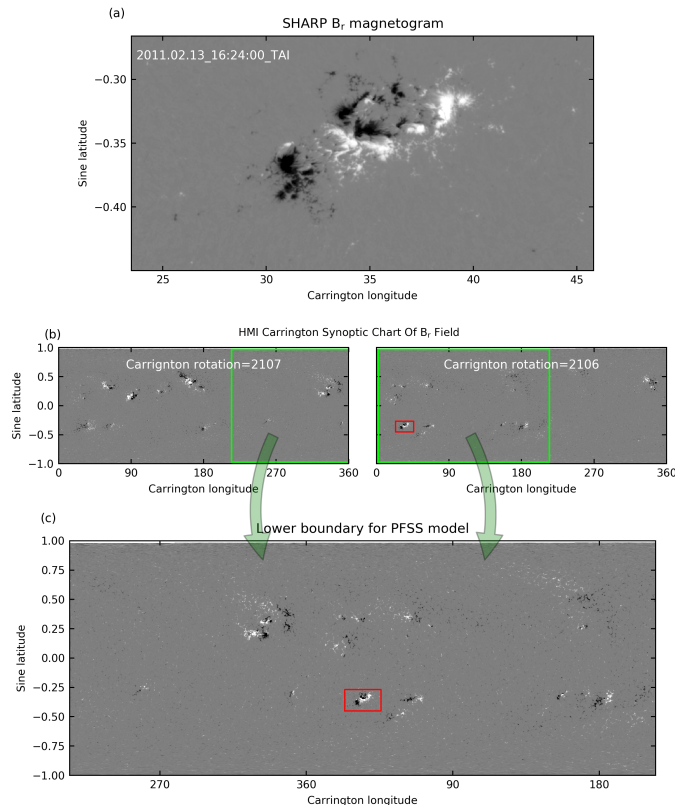


Figure 2.2: The data and technique used to create the lower boundary of the PFSS model (demonstrated by event #1 listed in Table 2.1), which includes: (a) an original SHARP magnetogram data of B_r component; (b) two synoptic charts at Carrington rotations covering the observation time of SHARP data and the next Carrington rotation, respectively. The green rectangles denote the area used for generating the maps showing in (c); (c) a remapped synoptic map is embedded with the SHARP data lowered to the resolution consistent with the synoptic map (denoted by the red box). The magnetic field is saturated at ± 300 Gauss. The red rectangles in (b)-(c) represent the field-of-view of the SHARP data.

The potential field is required as the initial condition and boundary condition of the extrapolation, for which the potential field source-surface (PFSS) model (Altschuler & Newkirk, 1969, Shiota et al., 2008) is initiated using the modified HMI synoptic chart of the radial magnetic field. The PFSS model can resolve the magnetic field at a spherical coordinate, which is a proper coordinate to reconstruct the coronal magnetic field because a planar representation could be improper with a large AR. The model assumes that the solar magnetic field beyond the “source surface

($r = R_{\text{ss}}$, usually at 2.5 solar radii) are open and radial, that is, $B_\phi(R_{\text{ss}}) = B_\theta(R_{\text{ss}}) = 0$ and $\mathbf{B}(R_{\text{ss}}) = B_r(R_{\text{ss}}) \hat{r}$. With the inner boundary placed at the photosphere and the outer boundary at the source surface, the PFSS solves the Laplacian equation (corresponding to Equation (1.6)) in *spherical polar coordinates*, where the solution of Equation (1.6) can be expressed as in the form of spherical harmonics:

$$\begin{aligned} \psi(r, \theta, \phi) = R_\odot \sum_{n=1}^{\infty} \sum_{m=0}^n P_n^m(\theta) \left\{ \left[c_n^m \left(\frac{r}{R_\odot} \right)^n + (1 - c_n^m) \left(\frac{R_\odot}{r} \right)^{n+1} \right] g_n^m \cos m\phi \right. \\ \left. + \left[d_n^m \left(\frac{r}{R_\odot} \right)^n + (1 - d_n^m) \left(\frac{R_\odot}{r} \right)^{n+1} \right] h_n^m \sin m\phi \right\}. \end{aligned} \quad (2.1)$$

The solution is presented in terms of the Legendre Polynomials $P_n^m(\theta)$, which are functions of the colatitude (θ). The R_\odot indicates the solar radius; c_n^m and d_n^m are the constants that $c_n^m = d_n^m = -[(R_{\text{ss}}/R_\odot)^{2n-1} - 1]^{-1}$ when value of R_{ss} is fixed; the g_n^m and h_n^m are known as Legendre coefficients, which are given by:

$$\begin{Bmatrix} g_n^m \\ h_n^m \end{Bmatrix} = \frac{2n+1}{4\pi(n+1)} \int_0^\pi \int_0^{2\pi} B_r(R_\odot, \theta, \phi) P_n^m(\theta) \begin{Bmatrix} \cos m\phi \\ \sin m\phi \end{Bmatrix} \sin\theta \, d\theta \, d\phi. \quad (2.2)$$

Consequently, the magnetic field B_r , B_θ , and B_ϕ at ($R_{\text{ss}} > r \geq R_\odot, \theta, \phi$) can be obtained by:

$$\begin{aligned} B_r = -\frac{\partial\psi}{\partial r} = \sum_{n=1}^{\infty} \sum_{m=0}^n \left[(1 - c_n^m)(n+1) \left(\frac{R_\odot}{r} \right)^{n+2} - n c_n^m \left(\frac{r}{R_\odot} \right)^{n-1} \right] P_n^m(\theta) \\ \times (g_n^m \cos m\phi + h_n^m \sin m\phi), \end{aligned} \quad (2.3)$$

$$\begin{aligned} B_\theta = \frac{-1}{r} \frac{\partial\psi}{\partial\theta} = -\sum_{n=1}^{\infty} \sum_{m=0}^n \left[(1 - c_n^m) \left(\frac{R_\odot}{r} \right)^{n+2} + c_n^m \left(\frac{r}{R_\odot} \right)^{n-1} \right] \frac{dP_n^m(\theta)}{d\theta} \\ \times (g_n^m \cos m\phi + h_n^m \sin m\phi), \end{aligned} \quad (2.4)$$

$$\begin{aligned} B_\phi = -\frac{1}{r \sin\theta} \frac{\partial\psi}{\partial\phi} = \frac{1}{\sin\theta} \sum_{n=1}^{\infty} \sum_{m=0}^n m \left[(1 - c_n^m) \left(\frac{R_\odot}{r} \right)^{n+2} + c_n^m \left(\frac{r}{R_\odot} \right)^{n-1} \right] P_n^m(\theta) \\ \times (g_n^m \sin m\phi - h_n^m \cos m\phi). \end{aligned} \quad (2.5)$$

We are, therefore, able to infer the magnetic structure of solar magnetic field with PFSS model according to Equation (2.3)-(2.5), with a modified HMI magnetic synoptic chart is used as input. It is worth noting that we are resolving a boundary value problem; thus, the solution is unique with a given boundary condition (the magnetogram vertical component). The PFSS model is calculated using a 1024-order spherical harmonic series expansion from the lower boundary (the modified synoptic chart) to the source surface. With the derived PFSS model, we cropped out the wedge whose boundary was where the SHARP data were embedded into the synoptic chart, and the resolution at the lower base of this domain is $0.0025 R_\odot$ per cell. This cropped data cube is the initial condition of the extrapolation. The horizontal components of the SHARP magnetograms (B_ϕ and B_θ), which are the boundary condition for relaxation, are interpolated to be consistent with the grid of the initial data cube at its bottom layer.

From the initial PFSS wedge-shape cube, the MHD-relaxation method gradually evolve the magnetic field in the whole domain through a set of MHD-like equations. which are:

$$\rho = |\mathbf{B}| \quad (2.6)$$

$$\frac{\partial \mathbf{v}}{\partial t} = -(\mathbf{v} \cdot \nabla) \mathbf{v} + \frac{1}{\rho} \mathbf{J} \times \mathbf{B} + \nu \nabla^2 \mathbf{v}. \quad (2.7)$$

$$\frac{\partial \mathbf{B}}{\partial t} = \nabla \times (\mathbf{v} \times \mathbf{B} - \eta \mathbf{J}) - \nabla \phi, \quad (2.8)$$

$$\mathbf{J} = \nabla \times \mathbf{B}. \quad (2.9)$$

$$\frac{\partial \phi}{\partial t} + c_h^2 \nabla \cdot \mathbf{B} = -\frac{c_h^2}{c_p^2} \phi, \quad (2.10)$$

where \mathbf{B} is the magnetic flux density, \mathbf{v} is the velocity, ν is a fictitious viscosity, \mathbf{J} is the electric current density, and ρ is the pseudo density. The pseudo density is assumed to be proportional to $|\mathbf{B}|$ in equation (2.6) in order to ease the relaxation by equalizing the Alfvén speed in space. The Equation (2.7) is the equation of motion, where the thermal pressure is neglected due to the zero- β assumption. The clearing potential equation (2.10) introduced by Dedner et al. (2002) plays a crucial role in avoiding deviation from $\nabla \cdot \mathbf{B} = 0$, where c_h^2 and c_p^2 is related to the coefficient of advection and diffusion, respectively.

In this thesis, the magnetic field (\mathbf{B}) is normalized by B_0 , which is equals to 3957 Gauss;

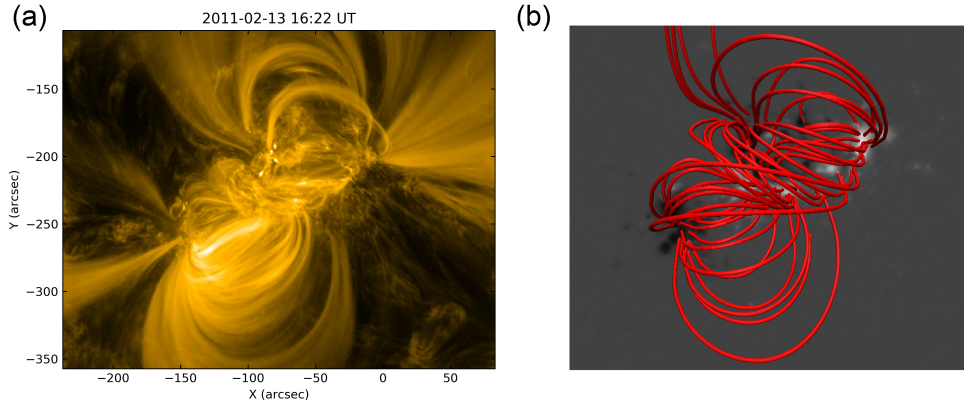


Figure 2.3: (a) SDO/AIA 171 Å observation of AR 11158 at 13 February 2011 16:22 UT. (b) NLFFF extrapolation result of AR11158. Red lines represent selected magnetic field lines from the NLFFF extrapolation.

the unit length L_0 is given by $0.0025 R_\odot$ at the lower base of the domain per cell. The density (ρ), time, and electric current (\mathbf{J}) are normalized by $\rho_0 = |B_0|$, $V_A \equiv B_0/(\mu_0\rho_0)^{1/2}$, and $J_0 = B_0/\mu_0 L_0$. In accordance with Inoue et al. (2014b), c_h^2 and c_p^2 used in this study are set to 0.04 and 0.01, respectively. The non-dimensional viscosity (ν) is a constant equals to 10^{-3} . The magnetic diffusivity (η) in Equation (2.8) is defined as:

$$\eta = \eta_0 + \eta_1 \frac{|\mathbf{J} \times \mathbf{B}| |\mathbf{v}|^2}{|\mathbf{B}|^2}, \quad (2.11)$$

where $\eta_0 = 5.0 \times 10^{-4}$ and $\eta_1 = 1.0 \times 10^{-3}$.

The computation requires magnetograms of all three components (B_ϕ , B_θ , B_r), which can act as the constraint to ensure the correctness of the NLFFF constructions. We stop the iteration when the best-fitting solution for all physical variables is achieved. The Lorentz force and the solenoidal condition within the numerical box are evaluated at the final step (see §2.3.2). Finally, we can numerically derive the three-dimensional coronal magnetic field. The numerical scheme we used in this study is the Runge–Kutta–Gill scheme with fourth-order accuracy for the integrals and a central finite difference with second-order accuracy for the spatial derivatives.

For each event, the vector magnetograms of the AR prior to the target flare for roughly 1 hour are served as the input of the NLFFF extrapolation. Figure 2.3 shows an example of the reconstructed coronal magnetic field, where the major magnetic field structures reconstructed by

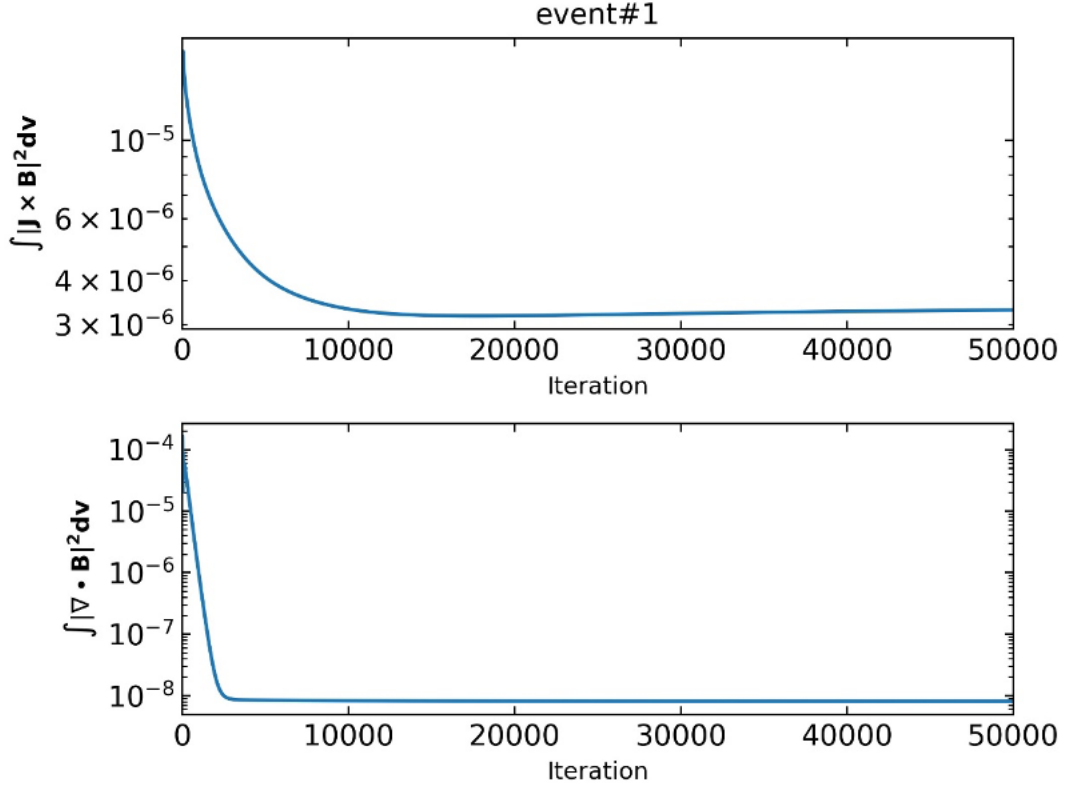


Figure 2.4: Profiles of $\int |\mathbf{J} \times \mathbf{B}|^2 dv$ and $\int |\nabla \cdot \mathbf{B}|^2 dv$ during the relaxation time for event #1 in this study. The values are presented in the normalized quantities.

the NLFFF model are well consistent with the coronal observations provided by SDO/AIA by the visual inspection.

2.3.2 Validity of NLFFF extrapolation

The validity of NLFFF should be separated into three parts: one is to check that if the computation converges to a steady solution; the second one is to check that if the solution is in a force-free state; the last one is the validation against the images of coronal loops.

To check that if the extrapolation is converged into a field which is consistent with the force-free assumption, first, we examined the profiles of Lorentz force and solenoidal condition during the

relaxation time. Figure 2.4 shows the Lorentz force and $\nabla \cdot \mathbf{B}$ integrated within the numerical box for event #1. During the calculation's relaxation time, it is required that the quantities do not only decrease to small numbers, but also show steady profiles; thus the step at which minimum subsequently appears after the relaxation process begins is not the outcome we want. Such profiles are also shown in other 50 events; thus, we can confirm that all the extrapolated results are well converged into certain solutions.

As the MHD-relaxation does not guarantee that the extrapolation results can achieve a force-free state, it is necessary to evaluate the Lorentz force remaining within the numerical domain and confirm the solenoidal condition at the final iteration step. To confirm that NLFFF extrapolations are consistent with a force-free field, we evaluated the force-freeness and solenoidal condition of all extrapolated result through calculating $\text{CW} \sin \theta$ metrics and $|f_i|$ metrics. The values of these domain-averaged metrics across all analyzed events are shown in Table 2.3. The $\text{CW} \sin \theta$ metric is the current weighted average of $\sin \theta$, where θ is the angle between the magnetic and current vector. The data points with S/N ratio ($|\mathbf{B}_i|/\sigma(\mathbf{B}_i)$) ≥ 3 is denoted to be current-free when calculating the metrics. $|f_i| = |(\nabla \cdot \mathbf{B})_i|/(6|\mathbf{B}_i|/\Delta x)$ indicates the absolute fractional flux ratio at the pixel i , where Δx is the grid spacing.

An ideal force-free and divergence-free field requires $\text{CW} \sin \theta = 0$ and $|f_i| = 0$. The value of $\text{CW} \sin \theta$ is typically less than 0.4, while the span of $|f_i| = 0$ could range in the scale between $[10^{-8}, 10^{-4}]$ (see, *e.g.*, DeRosa et al. 2015, 2009, Jing et al. 2018, Schrijver et al. 2008). With comparing the values shown in the previous works, the small numbers of these two quantities shown in Table 2.3 suggest a consistency with the force-free and divergence-free condition in our extrapolation results.

Finally, regarding the validation against the images of coronal loops, we have conducted a visible check for the major characteristics of the coronal loops through the AIA images taken at the close time; we found that only the reconstructed magnetic field in event #29 is significantly inconsistent with the coronal observation, which will be discussed in §3.2.4. Moreover, some previous studies have already conducted the same NLFFF extrapolation method and already compared the results to the SDO/AIA observations (*e.g.*, Inoue et al., 2016, 2014a, Kang et al., 2019, 2016, Muhamad et al., 2018). Hence we expect that the MHD-relaxation method can be feasible to reproduce the coronal magnetic structure that we are interested in.

Event#	CW sin θ	$ f_i $ (10^{-6})
1	0.07	19.59
2	0.05	8.86
3	0.05	3.42
4	0.11	4.24
5	0.10	4.43
6	0.11	4.28
7	0.11	1.84
8	0.13	4.39
9	0.13	2.56
10	0.12	5.69
11	0.10	7.86
12	0.10	7.94
13	0.09	4.23
14	0.11	6.45
15	0.07	4.88
16	0.10	3.05
17	0.10	3.34
18	0.10	3.07
19	0.07	5.45
20	0.08	2.42
21	0.09	3.61
22	0.09	4.36
23	0.09	5.35
24	0.06	5.16
25	0.05	3.61
26	0.06	2.52
27	0.10	3.55
28	0.04	8.38
29	0.04	7.27
30	0.06	3.10
31	0.13	5.67
32	0.09	2.64
33	0.09	6.15
34	0.10	2.56
35	0.03	3.06
36	0.03	3.31
37	0.03	3.46
38	0.03	3.17
39	0.03	3.14
40	0.03	3.44
41	0.15	2.67
42	0.05	5.38
43	0.04	55.06
44	0.04	2.00
45	0.04	29.09
46	0.13	3.53
47	0.10	4.45
48	0.04	10.26
49	0.06	6.11
50	0.06	3.63
51	0.06	4.08

Table 2.3: NLFFF model extrapolation metrics.

2.4 Linear discriminant function analysis

In this study, we aim to explore if two groups, which are eruptive events and confined events in this thesis, are statistically different on the basis of a specific measurement. Linear discriminant function analysis (DA; Leka & Barnes, 2003) is a statistical method that can quantify how exclusive these two groups are according to their measures of a parameter (e.g., Andersen et al., 1999, Kendall et al., 1983), thus inform the performance of the algorithm. In this thesis, linear DA is applied to test the distinguishing ability of the hypothesis that we will propose in the study.

DA builds a discriminant function that can classify which population the object is most likely to belong to, *i.e.*, maximize the correct rate of classifying analyzed events into two excluded groups. The first step for constructing the discriminant function is to estimate the probability density function of each group. For our cases, given two populations with $l = e$ (eruptive), c (confined), f_l is the probability density function for population l , which is defined as:

$$P(\mathbf{x}_a < \mathbf{x} < \mathbf{x}_b) = \int_{\mathbf{x}_a}^{\mathbf{x}_b} f_l(\mathbf{x}) d\mathbf{x}, \quad (2.12)$$

where $P(\mathbf{x}_a < \mathbf{x} < \mathbf{x}_b)$ is the probability that a measurement falls between \mathbf{x}_a and \mathbf{x}_b . Typically, the true probability density function (f_l) of a population is unknown, and so it must be estimated from the samples.

Now we want to know, for instance, the probability that an observed solar eruption belongs to the eruptive group ($l = e$) is measured with properties \mathbf{x} . By using Bayes's theorem, the probability can be expressed as:

$$P_e(\mathbf{x}) = \frac{q_e f_e(\mathbf{x})}{q_e f_e(\mathbf{x}) + q_c f_c(\mathbf{x})}, \quad (2.13)$$

where q_l is the prior probability of belonging to population l , which is estimated as the sample size of the population l (n_l).

The location of the discriminant function is assigned at where the two possibility distribution functions are equal to each other, *i.e.*, $q_e f_e(\mathbf{x}) = q_c f_c(\mathbf{x})$. This implies that the discriminant boundary is located where the two outcomes are predicted to occur at the same probability. In practice, based on certain measures \mathbf{x} , an observed solar eruption at a measure of \mathbf{x} is consequently classified into the eruptive population and confined population as below:

- $q_e f_e(\mathbf{x}) \geq q_c f_c(\mathbf{x}) \Rightarrow$ predict an eruptive events.
- $q_e f_e(\mathbf{x}) < q_c f_c(\mathbf{x}) \Rightarrow$ predict a confined events.

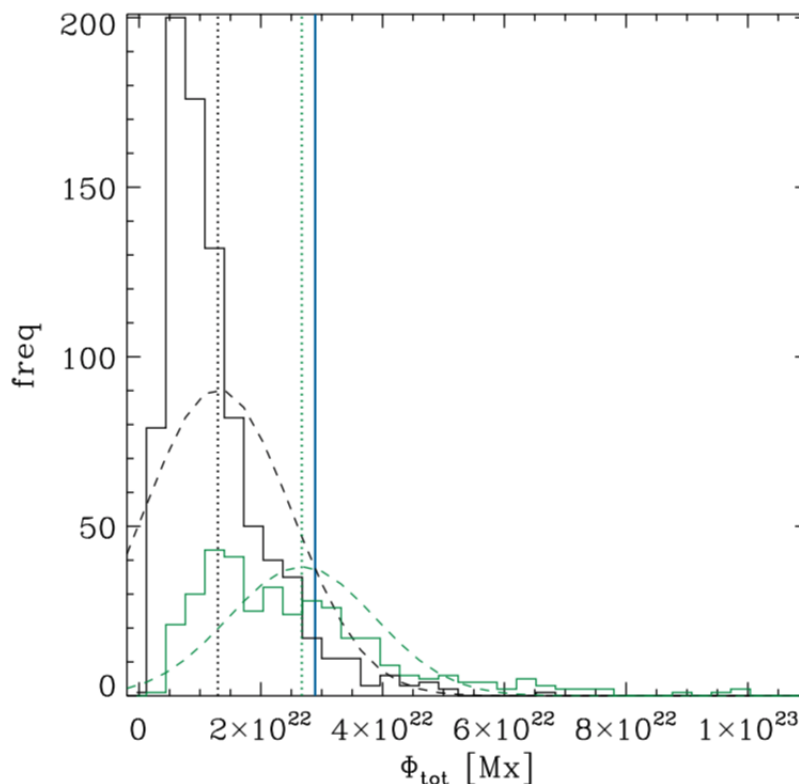


Figure 2.5: An example of showing the linear DA results based on the measures of magnetic flux (Φ_{tot}) adopted from Leka & Barnes (2003). The green/black histograms stand for the samples of flare-eruptive/flare-quiet ARs. The smoothed dashed curves colored in green/black represent the fitted densities. The vertical dashed lines demonstrate the mean values of flare-eruptive (green) and flare-quiet (black) ARs. A blue vertical solid line marks the values corresponding to two fitted curves that are intercepting with each other, which stands for the resulting discriminant function.

To sum up, with some measurements \mathbf{x} of an event, the discriminant function determines the population to which the event is most likely to belong. DA can thus be a powerful tool to validate our CME-eruptivity distinguishing algorithm, which is the objective of this thesis.

In the case of the linear DA, the analyzed events are samples taken from two populations that the probability density functions ($f_l(\mathbf{x})$) are assumed to be normal distributions with the same covariances but different means. The technique estimates the probability function of the populations by fitting the samples with the parametric Gaussian distribution function, and serves the fitted

function as the approximation of the true probability density. Given $i = 1, \dots, n_l$ measurements $\{x_{ik}^{(l)}\}$, of variables $k = 1, \dots, p$ in groups $l = e, c$, the multivariate Gaussian probability distribution used to represent the population probability density is given by:

$$\hat{f}_l(\mathbf{x}) = \frac{|\mathbf{C}|^{-1/2}}{(2\pi)^{p/2}} \exp\left[-\frac{1}{2}(\mathbf{x} - \bar{\mathbf{x}}^{(l)})' \mathbf{C}^{-1}(\mathbf{x} - \bar{\mathbf{x}}^{(l)})\right] \quad (2.14)$$

and the linear discriminant function is given by

$$f(\mathbf{x}) = \mathbf{x} \mathbf{C}^{-1}(\bar{\mathbf{x}}^{(e)} - \bar{\mathbf{x}}^{(c)}) - \frac{1}{2}(\bar{\mathbf{x}}^{(e)} + \bar{\mathbf{x}}^{(c)}) \mathbf{C}^{-1}(\bar{\mathbf{x}}^{(e)} - \bar{\mathbf{x}}^{(c)}) - \log\left(\frac{q_c}{q_e}\right), \quad (2.15)$$

where $\bar{\mathbf{x}}^{(l)}$ is the mean of the measurements in group l , and \mathbf{C}^{-1} is the inverse of the covariance matrix,

$$\mathbf{C} = \frac{n_e \mathbf{C}^{(e)} + n_c \mathbf{C}^{(c)}}{n_e + n_c - 2}, \quad (2.16)$$

with $\mathbf{C}^{(l)}$ the covariance matrix for population l , which is estimated from the samples as

$$C_{ij}^{(l)} = \sum_{k=1}^p (x_{ik}^{(l)} - \bar{x}_k^{(l)})(x_{jk}^{(l)} - \bar{x}_k^{(l)}) / (n_l - 1). \quad (2.17)$$

Figure 2.5 shows an example of the probability forecasts based on the linear DA with a single measurement is analyzed, which is adopted from Leka & Barnes (2007). The histograms show the original populations of flaring (green) and non-flaring (black) events. The point at which the two fitted probability functions are equal is shown with a vertical blue line that corresponds to the discriminant boundary's location. An AR with a measured value of the total magnetic flux (Φ_{tot}) falling to the right of the discriminant boundary would be classified as flare-imminent; for a measurement falling to the left, the AR would be predicted to be flare-quiet. One may be concerned that Gaussian distributions may not represent the true population distributions. For example, magnetic flux is a purely positive quantity and hence is not well represented by a perfect Gaussian distribution. Nevertheless, Leka & Barnes (2007) have discussed how results may vary by relaxing the assumptions of linear DA, and argued that linear DA is appropriate for small sample sizes.

Observation	Predicted	
	Yes	No
Yes	Hits (n_{11})	Misses (n_{12})
No	False alarms (n_{21})	Correct negatives (n_{22})

Table 2.4: Example of a classification table.

Since we have assumed the true population probability densities to be normal distributions with equal covariance matrices, we can, therefore, quantify the difference of the two fitted Gaussian distributions. To do this we may use, for instance, the Mahalanobis distance, which is a normalized measure of the distance between the sample means, and is defined as:

$$D^2 = (\bar{\mathbf{x}}^{(e)} - \bar{\mathbf{x}}^{(c)})^\top \mathbf{C}^{-1} (\bar{\mathbf{x}}^{(e)} - \bar{\mathbf{x}}^{(c)}). \quad (2.18)$$

A significant Mahalanobis distance between the two samples indicates that they are likely drawn from different populations. Another quantity that can be inferred from the linear DA is the probability that the samples come from different populations,

$$T^2 = \frac{n_e n_c}{n_e + n_c} D^2, \quad (2.19)$$

which has Hotelling's T^2 -distribution with $n_e + n_c - 2$ degrees of freedom (Kendall et al., 1983). This quantity can be used to express the possibility that the two samples come from two distinct populations.

Having established a discriminant function at which the two probability density functions are equal to each other, *i.e.*, where the two outcomes are predicted to occur with the same probability, we can present how well the function performs at classifying the two sets of samples by constructing a classification table, or a contingency table, which shows the binary, categorical classifications. As aforementioned, the threshold we use to construct the classification table is generally the value when two probability densities are equal. Table 2.4 presents a classic example of a classification table; the four combinations of a classification table are:

- *Hits* (n_{11}) - event predicted to occur, and observed to occur.
- *Misses* (n_{12}) - event predicted as not occur, but observed to occur.

- *False alarm* (n_{21}) - event predicted to occur, but did not occur.
- *Correct negatives* (n_{22}) - event predicted as not occur, and did not occur.

The relative accuracy of the classification table can be evaluated by a variety of categorical statics, which are computed from the elements in the table; for instance, the correct rate (CR) and True Skill Statistic (TSS or HKSS; Hanssen & Kuipers, 1965). CR is one of an intuitive way to determine the accuracy of the classification, which implies the fraction of the correct classification:

$$\text{CR} = \frac{n_{11} + n_{22}}{n_{11} + n_{12} + n_{21} + n_{22}}. \quad (2.20)$$

A perfect classification refers to $\text{CR} = 1$ and a completely incorrect classification lead to $\text{CR} = 0$. Nevertheless CR is a simple and intuitive score, it can be misleading when the ratio of Yes- and No-events ($N_{\text{Yes}}/N_{\text{No}}$) is extremely unbalanced. TSS is a widely used skill score that can also judge the accuracy of the classification, which is not sensitive to differences in the size of $N_{\text{Yes}}/N_{\text{No}}$. It is defined as:

$$\text{TSS} = \frac{n_{11}}{n_{11} + n_{12}} - \frac{n_{21}}{n_{21} + n_{22}}. \quad (2.21)$$

The skill is normalized so a perfect classification should correspond to $\text{TSS} = 1$; instead, a zero value indicates no skill is demonstrated in the classification. Of note, Bloomfield et al. (2012) denoted that the best TSS typically occurs when the chosen threshold can make $n_{21}/n_{12} \simeq N_{\text{Yes}}/N_{\text{No}}$.

It is worth noting that with a single realization using all data points, each data point is used to classify itself which will tend to underestimate the frequency of the incorrect predictions (Hills, 1966). To remove this bias, we perform cross-validation: we remove one object from the samples and establish the discriminant boundary, then classify the excluded event. For a set with n samples, the procedure is repeated for $n - 1$ turns to finally provide an unbiased classification table. With this unbiased classification table, in the same manner as what we have mentioned above, the corresponding CR and TSS can then be derived. Considering the small sample sizes (51 events) used in this study, cross-validation is employed by default in this study in order to minimize the bias in the skill scores.

Chapter 3

A New Parameter from Coronal Magnetic Field Models to distinguish Eruptive-Flare Producing Solar Active Regions

It is widely regarded that the possibility of any given flare event to produce an eruption could be inferred by the equilibrium of the erupting-core structure, which is referred to magnetic flux ropes (MFRs) in most of the cases, and the magnetic field structure in its immediate environs. One can imagine that the MFR is confined in a magnetic “cage”, if the cage is strong compared to the rope, it can confine the rope; however, when the cage is too weak to constraint the MFR, a coronal mass ejection (CME) could onset. Although the concept has been investigated and verified by numerous studies in the past (e.g. Liu, 2008, Sun et al., 2015, Thalmann et al., 2015, Toriumi et al., 2017, Wang & Zhang, 2007), the method by which to quantify how deeply the core structure is buried in the background field is still a topic of active research.

The results presented in Toriumi et al. (2017) motivate major parts of this study. Toriumi et al. (2017) statistically analyzed 51 \geq M5-class flare events, finding that neither the magnetic flux within the entire AR nor the flare-ribbon-related patterns are not sufficient conditions to produce eruptive events; whereas the flare-ribbon associated flux normalized to the flux across the total AR shows a relatively large discrepancy between two groups. The results demonstrate that it is more appropriate to use a *ratio* than imposing a single direct measurement when dealing with the CME-initialization

problem. Certainly, although one may argue that using post-eruption information could not allow us to perform a CME forecast, we believe that the findings shed light on the physical process of CME formation and is worthwhile to be pursued. By adopting the identical event list, a systematic analysis is performed using the nonlinear force free field (NLFFF) construction in this study, which enables us to deduce the magnetic field structure that might drive a CME's onset.

The major objective of this study is to propose a new parameter which may be used to evaluate the capability of triggering a CME eruption by also considering the topological information of magnetic field structures, and the balance between the ascending force and the suppression force. The newly introduced parameter, which we call r_m , is used to reflect such balance. A statistical approach is implemented in this study to test r_m 's ability of differentiating the eruptive/confined events for r_m . Moreover, we test out the hypothesis for approximating the MFR via the information inferred from NLFFF construction, in order to obtain the actual *volume* of an MFR which is necessary for the CME-eruptivity estimation.

This chapter contains the first part of our major analysis, which is the statistical study on the eruptive/confined events using the newly-proposed parameter: r_m . In this chapter, we first present the theoretical concept of r_m , as well as the approaches to derive r_m from observational data in §3.1. We then present the analysis of how to identify the MFR and discuss the hypothesis about which field lines can contribute to the suppression toward MFRs in §3.2. Finally, §3.3 gives the summary and conclusions of this study.

3.1 A new parameter: r_m

This section describes how the r_m parameter is computed via reconstructed NLFFF magnetic field. The physical meaning of r_m is first given in §3.1.1, in particular the methodology used to derive the corresponding values in each event listed in Table 2.1. Acting as one important component in r_m , the twist number (T_w) not only provides information of the locus of MFRs, but also informs the *range* of an area that we should take account when estimating r_m . The method to compute the T_w and the relevant knowledge of T_w in the context of solar-eruption analysis is shown in §3.1.2.

3.1.1 Concept of r_m parameter

The balance between the outward force that drives the eruption and the inward force that restricts the eruption can be conceptually expressed as:

$$r = \frac{F_{\text{driving}}}{F_{\text{suppress}}}, \quad (3.1)$$

where F_{driving} is the upward force acting on a flux rope formed by magnetic reconnection and F_{suppress} is the downward-directed force which confines the eruption. Since the NLFFF model assumes that all the forces are vanishing across the domain, it is challenging to estimate the amount of force directly from the NLFFF construction. As introduced in §1.2, the magnetic force is dominant among other forces in the solar corona, we propose a hypothesis that force-balance parameter can be approximated by the ratio between corresponding magnetic flux in the two systems:

$$r_m = \frac{\Phi_{\text{driving}}}{\Phi_{\text{suppress}}}, \quad (3.2)$$

such that a larger value of r_m indicates a higher possibility that an event will be eruptive. In this research we will explore whether this kind of parameter can help us infer whether there will be an eruptive event associated with the target reconnected MFR.

Figure 3.1 shows a diagram of an MFR above the photosphere and the surrounding magnetic field structure. The force that drives the eruption is regarded to be generated by the hoop-force contributed by the MFR. The upward force will let solar material escape from the low solar atmosphere and thus lead to a CME. The source of this driving force most likely arises from the hoop force generated by the electric current flowing in the MFR. Since the current is suggested to be formed with the magnetic reconnection in this model, Φ_{driving} can be approximated by $\Phi_{\text{reconnect}}$. To measure the reconnected flux from the observations, we must use another proxy to represent $\Phi_{\text{reconnect}}$. Démoulin & Aulanier (2010) suggested that twisted field lines are more likely to cause internal magnetic reconnection and trigger the solar eruption. Furthermore, some studies have indicated that the flare ribbon patterns match the foot points of the highly twisted field lines (Inoue et al., 2015, 2013, 2011). The statistical analysis implemented by Kazachenko et al. (2017) showed that the energy release of a flare, *i.e.*, the reconnected energy, is strongly correlated with the magnetic flux co-spatial with the flare ribbons, and the region swept by the flare ribbons has been shown to have a quantitative relationship with the magnetic reconnection process (Priest & Forbes, 2002, Qiu, 2009). Hence the highly twisted field lines should be a good proxy of reconnected field lines. For instance, Muhamad et al. (2018) analyzed the flare-eruptivity of the ARs using DAI (see §1.3).

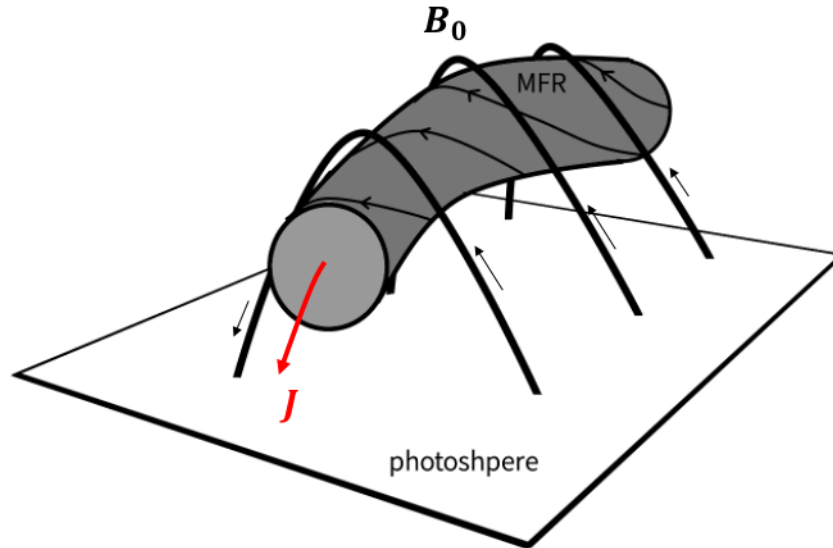


Figure 3.1: A schematic diagram of an MFR (shaded cylinder) suspended in the solar corona, with surrounding coronal field (\mathbf{B}_0) is depicted. The red arrow indicates the current (\mathbf{J}) flowing through the MFR.

The value of κ , which is a parameter used to evaluate the instability (see Equation (1.20)), requires the information of the reconnected location and area. To infer the value of κ before the eruption, the field lines with twist number larger than a certain threshold are utilized to approximate the reconnected flux; the parameter κ is then modified into κ^* based on such approximation. The results suggest that κ^* could be an indicator for the onset of a solar eruption event. Moreover, it implies that using highly twisted magnetic field to detect the reconnection in the pre-eruption phase is a feasible technique.

Regarding the denominator in Equation (3.2), we assume that the field lines which suppress the core region are mainly located nearby that region, and we refer to these field lines as “surrounding field lines”. According to the definition given in Kuperus & Raadu (1974), the strapping force (Lorentz force generated by $\mathbf{J} \times \mathbf{B}_0$ in Figure 3.1) can balance with the upward hoop-force originating from the MFR. Here we argue that the highly twisted field lines themselves can also generate the

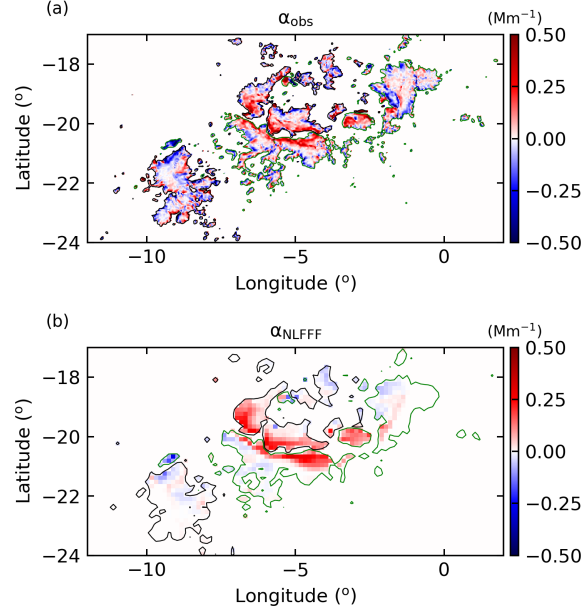


Figure 3.2: The distribution of α at photosphere (a) estimated with the SHARP magnetogram directly (α_{obs}) and (b) calculated based on the NLFFF magnetic field data (α_{NLFFF}). The values are presented in blue-red colored shading. Green (black) contours indicate radial magnetic field component at 250 Gauss (-250 Gauss). Note that the resolution of (a) is identical to the original SHARP data, whereas (b) is the degraded, lower boundary of the NLFFF data.

Lorentz force to confine the eruption, we hence modify (3.2) to:

$$r_m = \frac{\Phi_{T_w \geq T_c}}{\Phi_{\text{surrounding}} + \Phi_{T_w \geq T_c}}, \quad (3.3)$$

where $\Phi_{T_w \geq T_c}$ indicates the magnetic flux at the foot points of those field lines that have a twist value (T_w) over certain threshold (T_c); the definition and physical meaning of T_w will be introduced in §3.1.2. $\Phi_{\text{surrounding}}$ denotes the magnetic flux of the surrounding field lines. In our definition, $\Phi_{\text{surrounding}} + \Phi_{T_w \geq T_c} = \Phi_{\text{suppress}}$. To calculate the corresponding magnetic flux we integrate the vertical magnetic field component over the area where the coronal footpoints root in the photosphere.

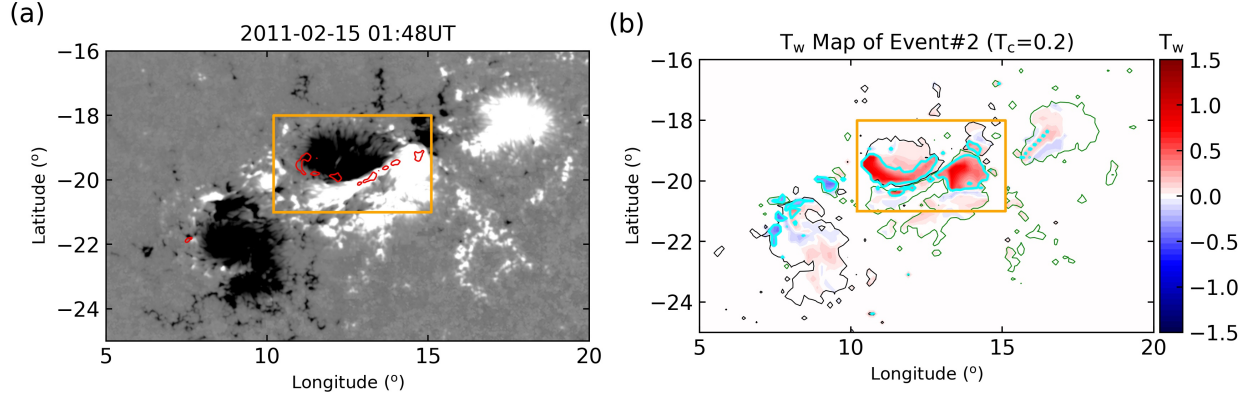


Figure 3.3: (a) AIA 1600Å emission captured at 15 February 2011 01:48 UT shows flare ribbons patterns (red contours) overlaid on a SHARP magnetogram at the same time (saturated at ± 500 Gauss). The white shading represents the positive value while the black shading represents the negative value. The threshold used to highlight the emission patterns is the intensity that is equal to or larger than the mean value for 20σ (standard deviation) at a quiet-Sun time. (b) Twist map for AR 11158 calculated from NLFFF extrapolation for event #2 in Table 2.1, which is taken at 15 February 2011 00:48 UT. The cyan contours are the foot prints of the field lines twist higher than 0.2 turns ($|T_w| \geq 0.2$). The green (black) contours indicate the magnetic field at 250 Gauss (-250 Gauss). An orange square in (a)&(b) highlights the region under consideration for r_m estimation.

3.1.2 Magnetic twist and highly twisted region

With the NLFFF extrapolation method introduced in §2.3, we can obtain the 3D magnetic field dataset and further calculate the corresponding twist number T_w . T_w can measure how many turns of two close field lines wind about each other (Berger & Prior, 2006), which is computed as:

$$T_w = \frac{1}{4\pi} \int \alpha dl. \quad (3.4)$$

Here, dl is a line element along a field line and α is the associated force-free parameter, which is defined by:

$$\alpha = \frac{\nabla \times \mathbf{B} \cdot \mathbf{B}}{|\mathbf{B}|^2}. \quad (3.5)$$

T_w is derived by integrating α over all of the voxels along each field line from one footpoint to the other. Apart from using NLFFF model to approach α and T_w , past studies have used a variety of methods to derive the values directly from the observation. For instance, Rust & Kumar (1996) used the ratio of length to width of an MFR; Leka & Skumanich (1999) estimated α from the magnetogram with:

$$\alpha_{\text{obs}} = \mu_0 J_z / B_z = (\nabla \times \mathbf{B}_h) / B_z, \quad (3.6)$$

where J_z is the signed magnitude of radial component of current, B_z is the signed magnitude of the radial magnetic field, and \mathbf{B}_h is the horizontal magnetic field vector.

For the data set used in this study, a comparison of α inferred from the observed magnetogram (α_{obs}) and the reconstructed NLFFF data (α_{NLFFF}) is shown in Figure 3.2. The value of α_{obs} is estimated with Equation (3.6), and the distribution of α_{NLFFF} is generated by assigning the α of field lines at the foot points. In Figure 3.2, which demonstrates the photospheric α distribution in event #1, we can find that α_{obs} is apparently more noisy, especially at the region corresponding to weak α_{NLFFF} . Even though the overall profiles are fairly different between α_{obs} and α_{NLFFF} , the locations at which maximum magnitudes concentrate are well consistent with each other (e.g., at longitude/latitude -5,-20). It should be noted that Leka et al. (2005) have evaluated the peak α value derived directly from the magnetogram (α_{peak}), suggesting that the α_{peak} is capable of recovering the twist value located near the MFR's axis. The comparison presented here demonstrates that applying α_{NLFFF} can also recover α around the axis. In a force-free construct, the α parameter is constant along each field line; in practice, we linearly integrate the α along the the field lines and divide by the field line length, making the α at the conjugate footpoints agree with the NLFFF assumptions, therefore each footpoint can then have a unique T_w assigned.

T_w can be an approximation of the winding of field lines about an axis field line without resorting to the MFR's axis, but only under certain conditions. Liu et al. (2016) have proved that Equation (3.4) can be a reliable approximation of the classical definition (see Berger & Prior, 2006, Equation (12)) when T_w locates near to the axis of a nearly cylindrically symmetrical MFR (*i.e.*, where T_w is concentrating). Moreover, Leka et al. (2005) used a ‘‘blind test’’ to verify the method of directly deriving T_w from the magnetogram, suggesting that only the T_w in the vicinity near an MFR's axis can be recovered, which is at the location of the local maximum $|T_w|$. We consequently apply T_w to search for the possible locus of MFRs in this analysis. For each NLFFF construction, we trace the field lines from multiple locations within each pixel on the lower boundary and compute the corresponding T_w at each derived field lines. In this case, we can derive a map of twist numbers (which is dubbed ‘‘twist map’’) by assigning the T_w of each field lines at the footpoints that thread on the photosphere. With such twist map, we can infer the locus at which MFR are rooting, and

calculate some necessary quantities that will be used in this analysis.

As mentioned in §3.1.1, the estimation of r_m requires estimation of both the flux of the highly twisted field lines ($\Phi_{T_w \geq T_c}$) and the flux of the field lines that surround them. As a result, this parameter strongly depends on the selection of the highly twisted field lines. Generally, MFR models describe a group of coherent twisted structures that wind around a common axis, building a flux rope which is then related to an eruptive eruption. The region where this MFR roots on the photosphere will form a pair of highly twisted regions conjugate along a polarity inversion line (PIL). However, in some active regions, there may simultaneously exist multiple, separated highly twisted regions which represent different ropes. Since in this situation the field-lines wind around a different axis and would be responsible for different eruptions, we should not simply include all the regions with $T_w \geq T_c$ in case we incorrectly involve other regions unrelated to the targeted event. To correctly identify the targeted flux rope that should be used for the estimation of r_m for a particular event, we additionally take into account that flare's ribbon location to find the appropriate flux rope's footpoint region. Only field lines that have connectivity inside this region will be identified as the targeted flux rope for calculating r_m . We traced the field lines from each resolution element, or pixel location, in the lower boundary of the NLFFF data. In these extrapolated field lines there may be a few field lines that obey the threshold but connect away from the main body of the MFR. We avoid including these field lines since they do not contribute to the main volume of the MFR.

Figure 3.3 presents an example of the footpoint-area identification in the context of multiple possible twisted-region candidates. Figure 3.3 (a) shows the initial brightening of flare ribbons inferred from SDO/AIA 1600 Å observations at 01:48UT. We highlight the region under consideration where ribbons appeared in the corresponding twist map at pre-flare time (Figure 3.3 (b)). As the twist value along a field line is uniquely assigned, the field lines across the PIL form a pair of conjugate patches in negative and positive polarity fields, which represent the footprints of the MFR. In Figure 3.3 (b), we find the pair of highly twisted patches with a similar shape to the flare ribbons, which will be selected to analyze the corresponding eruptivity in this study. In Figure 3.4, we show all selected highly twisted regions (with $T_c = 0.2$) that are used to estimate the subsequent r_m parameter values.

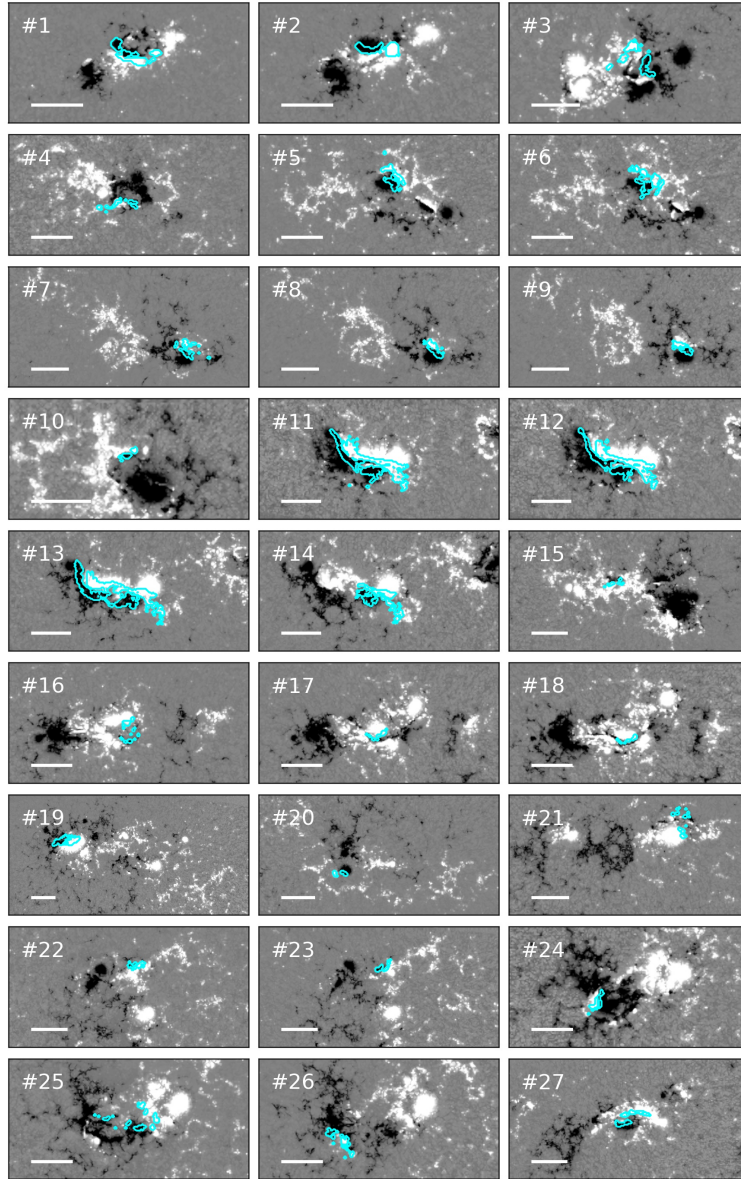
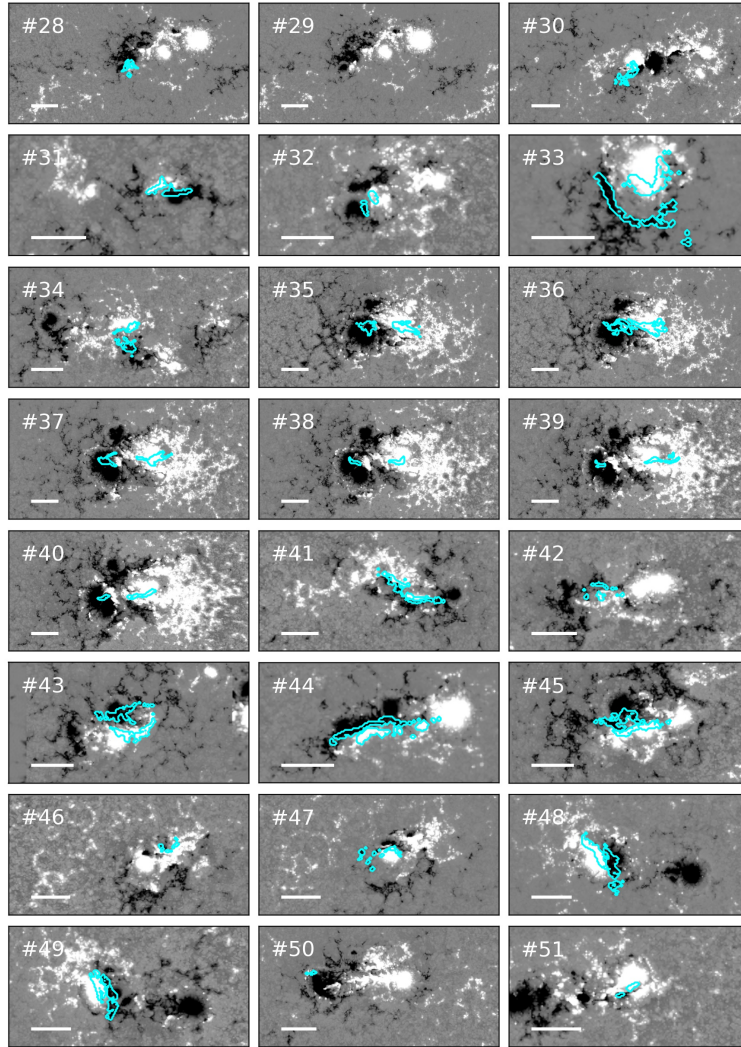


Figure 3.4: All events from Table 2.1 with the highly twisted flux used for analysis indicated. Background images are the B_r component which provides the boundary for the NLFFF extrapolation (saturated at ± 500 Gauss). The cyan contours indicate the regions selected to estimate the $\Phi_{T_w \geq T_c}$. Thick white line indicates the corresponding length of 50 Mm in the CEA projection.

**Figure 3.4:** (*cont.*)

When calculating the magnetic flux or any other physical quantities, in weak-field regions the large uncertainties for α makes the estimations of the twist values unreliable, hence we only consider the data where the radial component of the magnetic field strength is over 250 Gauss. The threshold of 250 Gauss is a somewhat conservative, but otherwise arbitrary, threshold above which the derived magnetic flux was not sensitive.

3.2 Results and Discussion

3.2.1 Comparison of highly twisted magnetic flux and flare-ribbon magnetic flux

The magnetic field structure in the pre-flare phase has been reconstructed through NLFFF extrapolation for 51 analyzed flare events. Following the method described in §3.1.2, we derived the highly twisted magnetic flux based on different thresholds (T_c) in order to find the most appropriate threshold value that can best represent the reconnected magnetic flux. We compare the magnetic flux in the highly twisted area to the magnetic flux co-spatial with the flare ribbons (Φ_{Ribbon}) provided by Toriumi et al. (2017). According to Toriumi et al. (2017), Φ_{Ribbon} is the magnetic flux at the region swept by the ribbon observed in SDO/AIA 1600 Å. The pixels for inclusion are selected by the criteria of 40 standard deviation higher than the average 1600 Å intensity in the quiet-Sun area. $\Phi_{T_w \geq T_c}$ is the magnetic flux corresponding to the field lines with $T_w \geq T_c$ within the considered region. The calculated $\Phi_{T_w \geq T_c}$ with different T_c value are listed in Table 3.1. We also evaluated the expected sensitivity of $\Phi_{T_w \geq T_c}$ to the uncertainty in the magnetic boundary data through a Monte Carlo analysis. In this analysis, we repeated the same extrapolation on event #1 using 16 different sets of magnetic data in which we artificially add the error of observations at each pixel multiplied by a Gaussian-weighted random number with unity variance. One can refer to Appendix B for further information of the uncertainty estimations applied in this thesis. The derived uncertainties of $\Phi_{|T_w| \geq 0.2}$, $\Phi_{|T_w| \geq 0.3}$, $\Phi_{|T_w| \geq 0.4}$ and $\Phi_{|T_w| \geq 0.5}$ are quoted in Table 3.1. Figure 3.5 shows the scatter plots of $\Phi_{T_w \geq T_c}$ and Φ_{Ribbon} with different T_c values. We used a linear correlation coefficient (CC) and the slope of the linear fit (r) to evaluate whether $\Phi_{T_w \geq T_c}$ well represents the reconnected flux. we use T_c starts from 0.2 to choose the highly twisted regions of interest; because when $T_c = 0.1$, the blobs obtained with the thresholding method applying on the twist map encompass the entire AR and can hardly be isolated from each other with a visual inspection. The related discussion is presented in Appendix A. According to the results listed in Table 3.1 and shown in Figure 3.5, we find that both $\Phi_{|T_w| \geq 0.2}$ and $\Phi_{|T_w| \geq 0.3}$ are highly correlated with Φ_{ribbon} but in the case of $\Phi_{|T_w| \geq 0.2}$, the value of r is much closer to 1. This suggests that the twisted flux well represents the ribbon flux when using threshold of 0.2. Combining the results of CC and r , we conclude that $\Phi_{|T_w| \geq 0.2}$ is the most representative for reconnected flux. With the criteria set at $T_c = 0.2$, we can identify highly twisted regions in the vicinity of the initial flare ribbons for all but one of the 51 events; the exception is studied in §3.2.4.

Following the same concept, Muhamad et al. (2018) used a much higher value of T_c to represent the reconnection flux. According to Muhamad et al. (2018), different T_c values were tested and the

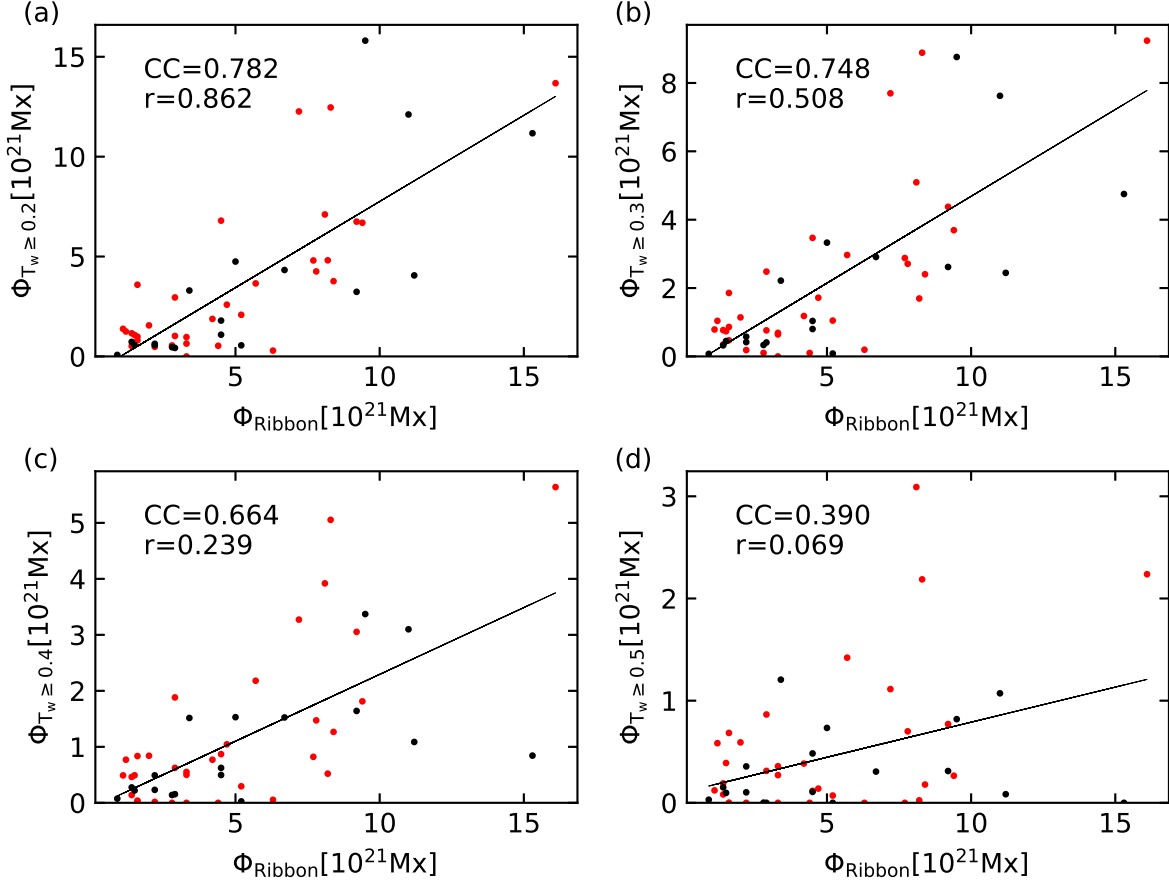


Figure 3.5: Scatter plots present the comparison of the magnetic flux within the twisted region ($\Phi_{T_w \geq T_c}$) and the magnetic flux within the ribbon region (Φ_{Ribbon}) as calculated by Toriumi et al. (2017) for all 51 events. Red (black) dots represent eruptive (confined) events. A straight line shows the result of a linear fit, while the correlation coefficient (CC) and the slope of regression line (r) are shown at the top left. Note the varying y -scale.

most appropriate threshold was determined by examining the variation of κ^* with time during the flare eruption. The authors concluded that $T_c = 0.5$ was the most representative criteria for the reconnected field lines as κ^* drastically decreased after the flare occurs. However, in our study we find that $T_c = 0.5$ is not a suitable threshold under the assumption that $\Phi_{\text{reconnect}} \simeq \Phi_{\text{Ribbon}}$. We suggest that such a discrepancy results from the different purposes of the two studies. We believe that the reconnected flux we estimate in this study focuses on “all” field lines that reconnected

after the flare onset and contribute to the flux rope. Moreover, the flux estimated by Muhamad et al. (2018) corresponds to field lines that trigger the onset of the flare instead of all field lines provided by the magnetic field in the immediate vicinity. Figure 3.6 explains our theorem: the red field lines are those with twist value over 0.5 and the yellow field lines are less twisted. According to tether cutting model proposed by Moore et al. (2001), the core of the flux rope is formed by the inner reconnection of these strongly twisted field lines, which is illustrated in Figure 3.6 (a). These red field lines are where the initial reconnection begins, after which the less twisted field lines will also reconnect and become involved in the formation of the flux rope in the later phase (see Figure 3.6 (b)). The double-arc instability focuses on the beginning phase of the flare (*i.e.*, the triggering mechanism of the flare) therefore the higher-altitude twisted field lines (red field lines in Figure 3.6) are much more important. In this case a higher threshold is required to select these field lines. However the question we want to solve here is whether the formed flux rope itself will be accelerated against the Sun or not. As such we focus on the strength of this uplifting motion (estimated by $\Phi_{|T_w| \geq 0.2}$ in this study) and whether it can over-take the suppressive forces provided by the magnetic field in the immediate environs. We therefore use a smaller value of T_c to include all the field lines in the immediate vicinity (both the yellow and red field lines shown in Figure 3.6).

Event#	$\Phi_{ T_w \geq 0.2}$ $\pm 0.6\%$ (10^{20}Mx)	$\Phi_{ T_w \geq 0.3}$ $\pm 0.9\%^a$ (10^{20}Mx)	$\Phi_{ T_w \geq 0.4}$ $\pm 2.3\%$ (10^{20}Mx)	$\Phi_{ T_w \geq 0.5}$ $\pm 2.5\%$ (10^{20}Mx)
1	29.52	24.81	18.82	8.65
2	36.54	29.68	21.8	14.21
3	17.93	10.38	4.96	1.07
4	7.27	3.24	2.75	1.51
5	18.77	11.83	7.7	3.84
6	25.9	17.17	10.44	1.39
7	13.8	7.88	4.9	1.22
8	15.53	11.41	8.41	5.91
9	12.48	10.41	7.7	5.84
10	2.91	1.95	0.54	0
11	136.77	92.38	56.39	22.38
12	124.61	88.86	50.53	21.87
13	122.62	76.97	32.72	11.13
14	37.66	24.03	12.67	1.79
15	6.31	5.77	4.91	3.56
16	4.8	1.85	0.17	0
17	4.61	3.34	1.4	0
18	4.24	4.08	1.54	0
19	67.46	43.77	30.53	7.71
20	5.51	1.02	0	0
21	6.42	6.42	5.52	2.71
22	10.24	7.62	6.24	3.13
23	5.67	4.49	2.21	0.97
24	10.74	7.36	4.92	3.9
25	8.05	4.72	0.39	0
26	9.88	8.62	8.35	6.84
27	20.83	10.49	2.95	0.71
28	10.87	8.01	6.24	4.83
29	0	0	0	0
30	33	22.16	15.15	12.05
31	11.57	7.69	4.62	1.9
32	5.33	1.01	0	0
33	48.11	16.95	5.2	0.24
34	35.88	18.57	0.29	0
35	121.1	76.24	30.99	10.72
36	158.06	87.6	33.71	8.19
37	111.71	47.51	8.43	0
38	40.56	24.44	10.87	0.84
39	32.33	26.17	16.41	3.11
40	43.25	29.09	15.25	3.06
41	42.54	27.09	14.72	7
42	5.55	0.85	0.26	0
43	67.96	34.68	8.69	1.17
44	47.47	33.28	15.3	7.33
45	66.9	36.92	18.13	2.65
46	5.16	3.48	1.39	0.82
47	9.66	6.89	5	3.58
48	71.05	50.94	39.19	30.91
49	48.04	28.77	8.21	0
50	0.75	0.75	0.75	0.3
51	5.66	4.18	2.31	1.03
CC ^b	0.782	0.748	0.664	0.39
r ^c	0.862	0.508	0.239	0.07

^a The uncertainties are presented assuming all magnetic fluxes estimated in event #1 are representative.

^b Correlation coefficient between $\Phi_{T_w \geq T_c}$ and Φ_{Ribbon} .

^c Slope of the linear regression line of $\Phi_{T_w \geq T_c}$ and Φ_{Ribbon} .

Table 3.1: Highly twisted flux based on different T_c

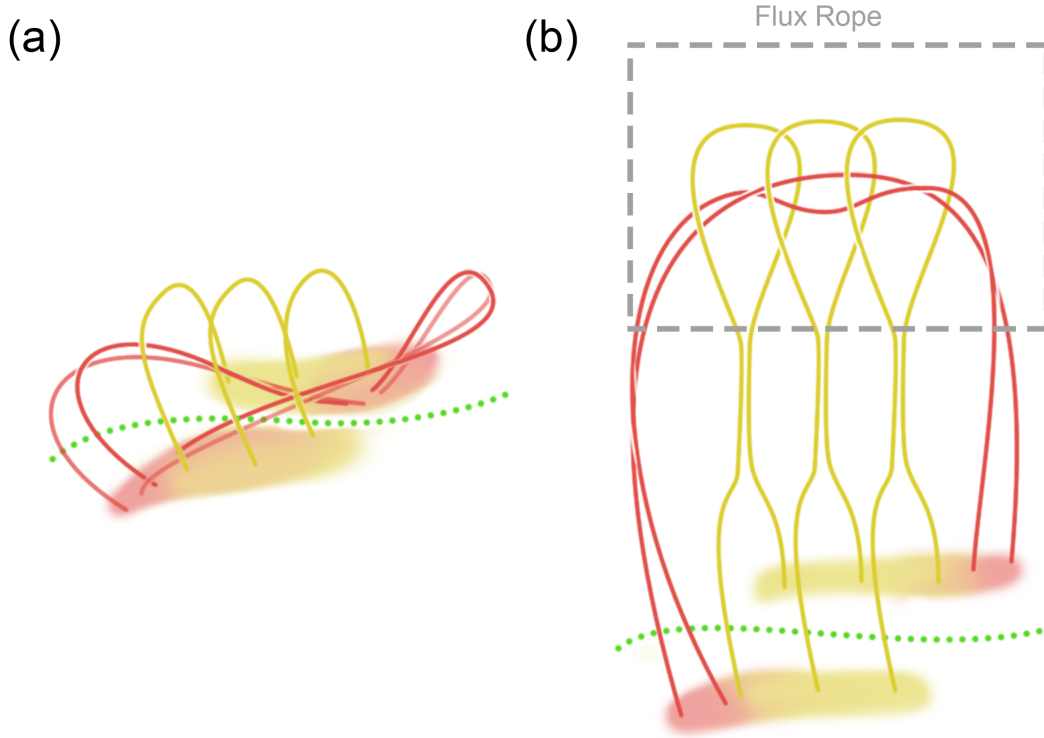


Figure 3.6: Schematic showing the topology of the field lines (a) before the onset of the eruption and (b) after the flare ribbons form. Red curves and red footpoints represent the highly twisted field lines which undergo tether cutting reconnection and evolve into the magnetic flux rope. Yellow curves and their yellow footpoints are the slightly twisted field lines which strap the highly twisted field lines.

3.2.2 Overlying field and wall Field

The definition of $\Phi_{\text{surrounding}}$ is still not well constrained since it has not been revealed yet what kind of field lines will provide suppression force to the eruption. In this study, we will propose several possible hypotheses about its composition and use linear DA to test which is the most robust.

We defined surrounding field lines as those outside the core region which that provide inward force to prevent the escape of the formed MFR structure. The surrounding field lines may comprise a few components, as described by two hypotheses: first, there are numerous studies suggesting that overlying field can suppress the upward ascending eruption. (*e.g.*, Démoulin & Aulanier, 2010,

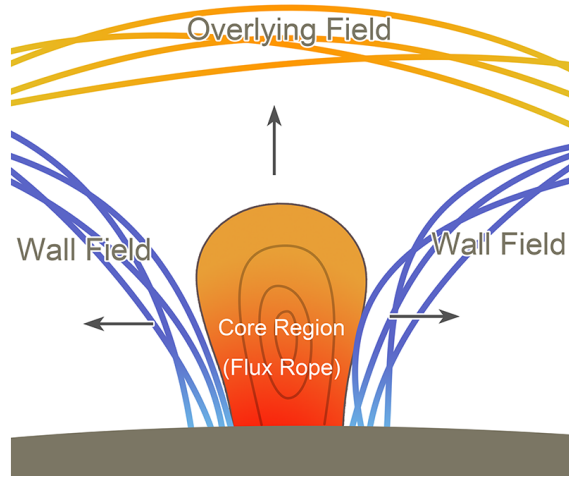


Figure 3.7: Schematic for overlying field lines and wall field lines. The red area located in the center represents the expanding core structure of the eruption. Black arrows indicate the expansion direction. Yellow and Blue curves schematically show the relative location of the overlying field lines and wall field lines, respectively.

Kuperus & Raadu, 1974, Sun et al., 2015, Wang & Zhang, 2007) We propose that $\Phi_{\text{surrounding}}$ may be the flux corresponding to field lines that lie above the highly twisted region ($\Phi_{\text{surrounding}} = \Phi_{\text{overlying}}$).

Our second hypothesis is based on the fact that the lifting of the core region will need to push out the lateral field to make a wide channel. We propose that the strength of the field lines which form a fence around the core region will also relate to the eruptivity. We refer to these field lines as “wall” field lines and the term $\Phi_{\text{surrounding}}$ will be composed of the overlying field *and* the wall field ($\Phi_{\text{surrounding}} = \Phi_{\text{overlying}} + \Phi_{\text{wall}}$). The topologies of these field lines are explained in Figure 3.7, where wall field lines are those with one footpoint either beneath or near the growing core region of an eruption.

After obtaining $\Phi_{T_w \geq T_c}$ and $\Phi_{\text{surrounding}}$, r_m is calculated according to Equation (3.3). It is worth mentioning that some studies estimate the similar quantities by calculating the transverse magnetic field across the PIL at higher altitude and the lower altitude, and estimate their ratio, which is similar to the concept of r_m (Liu, 2008, Sun et al., 2015, Thalmann et al., 2015, Toriumi et al., 2017, Wang & Zhang, 2007). However, to precisely evaluate the balance and correctly define the morphology of the surrounding field, we attempt to select the field lines based on topological definition instead of only considering altitude. Regarding these two hypotheses, we will use linear

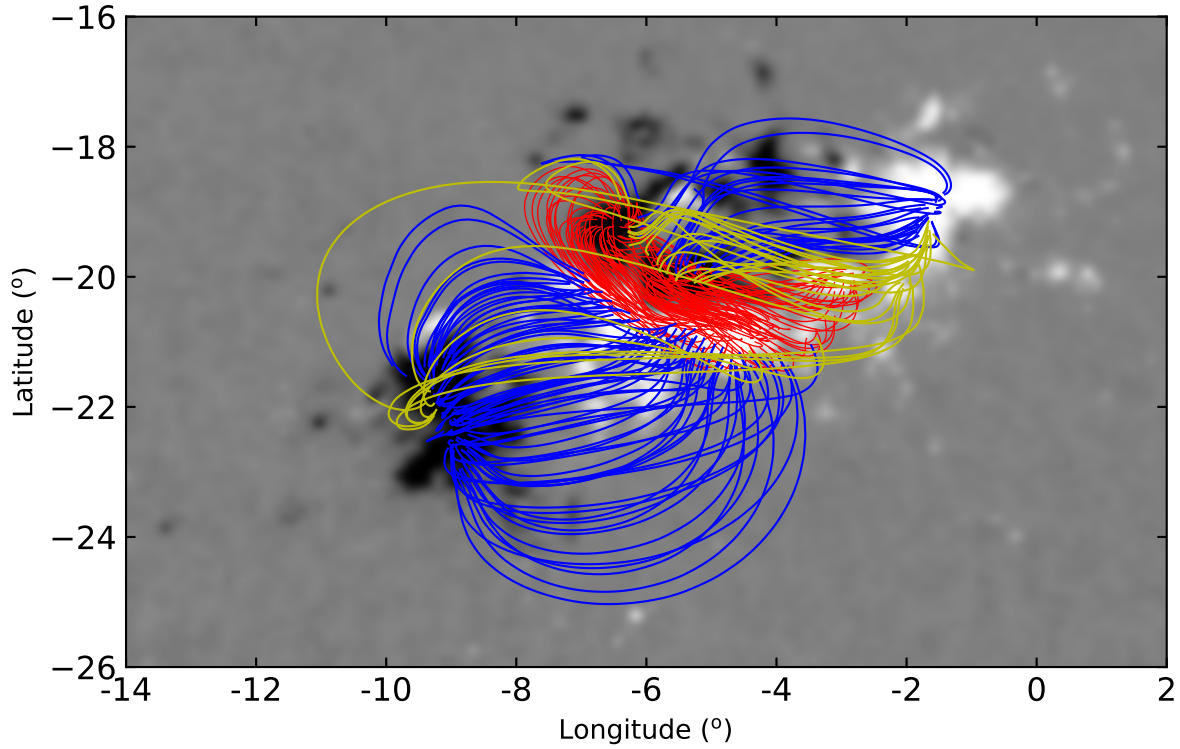


Figure 3.8: Curves illustrate the field lines selected according the thresholds described in §3.2.2. Following the color scheme in Figure 3.7, shown are the overlying field lines (yellow), highly twisted field lines (red), and wall field lines (blue). The field lines are projected along the direction of gravity. The background is the interpolated photospheric magnetogram (saturated at ± 500 Gauss) which is served as the lower boundary condition of this event #1.

DA to test which is the most robust. This technique can provide some metrics to help us judge the performance of r_m in distinguishing eruptive events and confined events, and also help us check which hypothesis can better separate two groups.

In our first hypothesis, the surrounding field lines are actually the overlying field lines. To select the overlying field lines we project all field lines derived from NLFFF extrapolation onto the photosphere, choosing those that intersect the highly twisted field lines in the direction of

gravity. We also remove those field lines that lie totally beneath the highly twisted field lines. The corresponding magnetic flux is then integrated over the relevant footpoints on the photosphere. As the threshold 0.2 for the highly twisted region can well represent the reconnected flux, we determine the overlying field lines based on this threshold as well. The overlying field lines for event #1 are plotted as the yellow curves in Figure 3.8. In the second hypothesis, the field lines near the core region are also included in $\Phi_{\text{surrounding}}$. This type of field line will only have one footpoint near or possibly inserted beneath the highly twisted field lines, as shown in Figure 3.7. We thus define the wall field as those field lines that with only one footpoint located near to the projection of highly twisted field line, and the threshold of distance from footpoint to core region is 10 Mm. We establish this distance by maximizing essentially all metrics calculated from the linear DA when only that variable is varied. Figure 3.8 shows the topology of these projected wall field lines in event #1. After deriving $\Phi_{\text{surrounding}}$, the r_m parameter is calculated separately based on the two hypotheses. We refer to the r_m value estimated according to hypothesis 1 as r_m^o and that estimated according to hypothesis 2 as r_m^{o+w} . Table 3.2 lists all derived r_m^o and r_m^{o+w} across all analyzed events.

Event#	$\Phi_{ T_w \geq 0.2}$ $\pm 0.6\%$ (10^{20}Mx)	$\Phi_{\text{overlying}}$ $\pm 9.8\%$ (10^{20}Mx)	Φ_{wall} $\pm 1.3\%$ (10^{20}Mx)	r_m^{a} $\pm 2\%$	$r_m^{\text{a+w b}}$ $\pm 1\%$
1	29.52	6.45	51.29	0.82	0.34
2	36.54	8.21	93.55	0.82	0.26
3	17.93	40.15	25.65	0.31	0.21
4	7.27	9.31	11.23	0.44	0.26
5	18.77	16.16	24.53	0.54	0.32
6	25.90	12.52	32.70	0.67	0.36
7	13.80	5.61	16.74	0.71	0.38
8	15.53	6.57	16.19	0.70	0.41
9	12.48	13.48	17.50	0.48	0.29
10	2.91	17.32	3.78	0.14	0.12
11	136.77	144.36	17.88	0.49	0.46
12	124.61	144.58	24.63	0.46	0.42
13	122.62	107.94	12.76	0.53	0.50
14	37.66	52.18	27.03	0.42	0.32
15	6.31	18.58	36.44	0.25	0.10
16	4.80	6.91	15.36	0.41	0.18
17	4.61	21.47	65.38	0.18	0.05
18	4.24	24.13	68.58	0.15	0.04
19	67.46	75.98	77.16	0.47	0.31
20	5.51	5.22	13.45	0.51	0.23
21	6.42	7.16	14.06	0.47	0.23
22	7.45	12.13	22.97	0.38	0.18
23	5.67	14.17	9.54	0.29	0.19
24	10.74	28.55	59.92	0.27	0.11
25	12.31	68.21	12.64	0.15	0.13
26	9.88	25.97	25.87	0.28	0.16
27	20.83	15.55	43.14	0.57	0.26
28	10.87	62.11	48.35	0.15	0.09
29	0.00	0.00	0.00	0.00	0.00
30	33.00	31.23	61.51	0.51	0.26
31	11.57	4.49	3.17	0.72	0.60
32	5.33	15.32	13.09	0.26	0.16
33	48.11	67.60	15.24	0.42	0.37
34	35.88	35.54	61.11	0.50	0.27
35	121.10	137.76	185.04	0.47	0.27
36	158.06	132.80	202.44	0.54	0.32
37	111.71	98.00	187.26	0.53	0.28
38	40.56	89.32	186.15	0.31	0.13
39	35.74	44.45	197.15	0.45	0.13
40	43.25	52.51	239.52	0.45	0.13
41	42.54	38.69	29.68	0.52	0.38
42	5.55	29.71	21.26	0.16	0.10
43	67.96	21.99	52.87	0.76	0.48
44	47.47	33.83	19.79	0.58	0.47
45	66.90	81.90	45.94	0.45	0.34
46	5.16	0.56	11.31	0.90	0.30
47	9.66	14.35	63.24	0.40	0.11
48	71.05	65.79	20.47	0.52	0.45
49	48.55	73.60	31.12	0.40	0.32
50	0.75	12.59	11.73	0.06	0.03
51	5.66	22.75	46.91	0.20	0.08

^a r_m calculated based on hypothesis 1 ($\Phi_{\text{surrounding}} = \Phi_{\text{overlying}}$).

^b r_m calculated based on hypothesis 2 ($\Phi_{\text{surrounding}} = \Phi_{\text{overlying}} + \Phi_{\text{wall}}$).

Table 3.2: Estimations related to r_m .

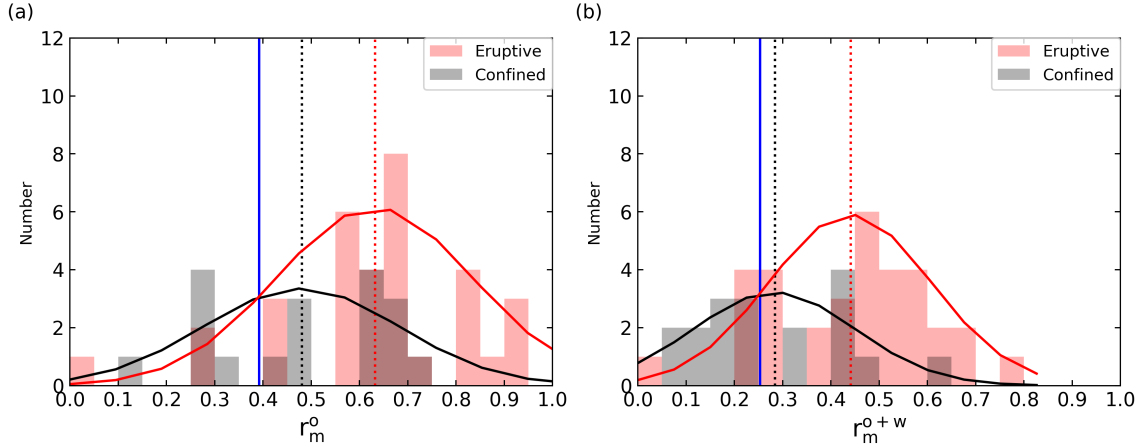


Figure 3.9: Linear DA results of r_m^o and r_m^{o+w} . Red (Black) histogram represents the eruptive (confined) flares. Overlaid red (black) curves are the Gaussian probability density functions (PDFs) for eruptive (confined) flares. Red (black) vertical dash lines indicate the mean value of r_m for eruptive (confined) events. The point at which the two probability distribution functions are equal is denoted by the blue vertical line.

3.2.3 DA results

DA results for r_m based on the two hypotheses are shown in Figure 3.9. The overlaid curves are the estimated probability density functions. The vertical blue line indicates the location where two probability densities are equal (which implies the probability of eruptive flare is 50%) and it defines our discriminant boundary. Samples which lie to the right (left) of the boundary are assumed to be eruptive (confined) since the corresponding probability density function lies above the confined (eruptive).

This shows that higher r_m is in fact related to a higher probability of producing an eruptive flare, in both hypotheses. The metrics derived using DA are listed in Table 3.3. The higher value of the probability that two samples are from different populations for r_m^{o+w} implies that using r_m^{o+w} may better distinguish the two populations than r_m^o . Despite the relatively high probabilities, however, the small sample sizes mean that the values are insufficient to definitively state that two distributions are from distinct populations. In parallel, the Mahalanobis distance for the sample PDFs is higher for r_m^{o+w} , again implying that the underlying populations of r_m for confined events *vs.* eruptive events becomes more exclusive when using r_m^{o+w} to discriminate the events. The

classification tables constructed with $n - 1$ cross-validation are presented in Tables 3.4 and 3.5. The correct rates and TSS statistics yielded from the classification tables are summarized in Table 3.3. Both of these two metrics are higher when using $r_m^{\text{o+w}}$, indicating an improved classification ability when Φ_{wall} is included in the calculation of r_m^{o} .

To test the reliability of the resulting metrics from the DA, we estimate the corresponding uncertainties by performing Monte Carlo and Bootstrap algorithm on our dataset. The detail of the error estimations is described in Appendix B. The mean values and standard deviations derived from the two kinds of error estimations provide the metrics and their uncertainties based on these two methods as summarized in Table 3.3. The expected small errors provided by Monte Carlo method here is because the uncertainties in the magnetic flux we derived in §3.2.1 are inherently small. The small uncertainties do not change the fitted PDFs as well as the discriminant function drastically, hence the DA results do not vary substantially. Compared to Monte Carlo method, Bootstrap method measures the uncertainties from the sampling process, thus we can expected it will provide a relative large error due to the small sample size used in this study. We should consider the error provided by Monte Carlo methods as a lower bound, and the error from the Bootstrap method as an upper bound on the uncertainty estimates for the DA results.

Parameter	Mehod	Statistical Metrics			
		Probability (%)	MD ^a	CR ^b	TSS
r_m^{o}	Original	94	0.63	0.65	0.15
	Monte Carlo	93.9±0.4	0.63±0.02	0.66±0.01	0.17±0.02
	Bootstrap	84.5±17.4	0.59±0.41	0.67±0.07	0.14±0.18
$r_m^{\text{o+w}}$	Original	96.9	0.85	0.73	0.37
	Monte Carlo	96.9±0.2	0.85±0.02	0.73±0.01	0.38±0.02
	Bootstrap	89.8±12.7	0.78±0.57	0.69±0.07	0.20±0.19
$ \Phi _{\text{Ribbon}}/ \Phi _{\text{AR}}$	Original	97.2	0.88	0.67	0.07

^a Mahalanobis distance for the sample PDFs.

^b Correct rate of the classification table.

Table 3.3: DA results (with $n - 1$ cross-validation) of r_m^{o} and $r_m^{\text{o+w}}$

Observation	Predicted	
	Eruptive	Confined
Eruptive	27	6
Confined	12	6

Table 3.4: Classification table (with $n - 1$ cross-validation) for r_m^o

Observation	Predicted	
	Eruptive	Confined
Eruptive	27	6
Confined	8	10

Table 3.5: Classification table (with $n - 1$ cross-validation) for r_m^{o+w}

We also carried out DA on $|\Phi|_{\text{Ribbon}}/|\Phi|_{\text{AR}}$ provided by Toriumi et al. (2017). Due to the limited information available, we did not perform the error analysis on this parameter. The resulting metrics are shown in Table 3.3. The Mahalanobias distance and the probability derived based on $|\Phi|_{\text{Ribbon}}/|\Phi|_{\text{AR}}$ are comparable with the results of r_m^{o+w} ; however, the correct ratio and TSS derived based on $|\Phi|_{\text{Ribbon}}/|\Phi|_{\text{AR}}$ are significantly smaller than those derived based on r_m^o and r_m^{o+w} . This implies that the classification tables based on r_m^o and r_m^{o+w} can provide better classifying ability than using $|\Phi|_{\text{Ribbon}}/|\Phi|_{\text{AR}}$. As a result, we can statistically conclude that using r_m^{o+w} to classify the potential for eruptivity out performs using $|\Phi|_{\text{Ribbon}}/|\Phi|_{\text{AR}}$.

Through linear discriminant analysis we find that neither r_m^o nor r_m^{o+w} are perfectly able to differentiate eruptive from non-eruptive events, although r_m^{o+w} may differentiate the events better. To examine one possibility of why this is the case, we next examine one of the incorrectly classified events in detail.

3.2.4 An exceptional event: X1.2 flare on 2014 January 7

Although we can identify the highly twisted region in most of the events, for the X1.2 flare on Jan 7 2014 (event #29 in our event list) that peaks at 18:32 UT, we failed to reconstruct any highly twisted region where flare ribbons appear, which contradicts our assumption that a highly twisted

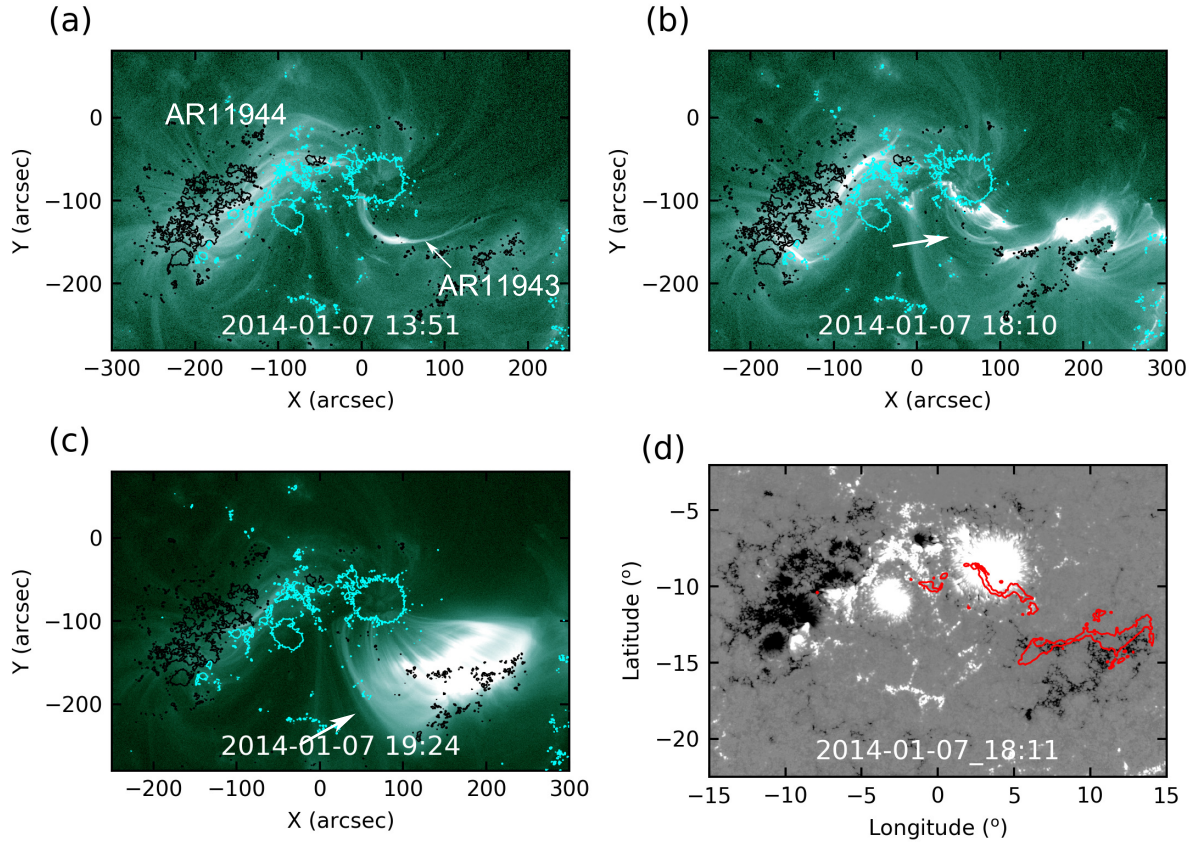


Figure 3.10: (a)-(c) are the SDO/AIA 94 Å observations of AR11944 and AR11943 at three different times. The overlaid contours present the HMI magnetograms in the line of sight direction. The photosphere magnetic field of -500 Gauss and 500 Gauss are marked by black and cyan contours, respectively. (a) The sigmoid which trigger the flare eruption captured one day before the eruption (Jan 6 08:15UT). A white arrow indicates the position of the sigmoid. (b) The eruption of the sigmoid structure. The flaring location is indicated by a white arrow. (c) The post flare arcade came up after the CME and flare erupted. (d) Ca II H line emission (highlighted by the same threshold mentioned in Figure 3.3) shown by the red contours overlaid on SHARP magnetogram data. The white and black shading corresponds to positive and negative polarities, respectively.

region will trigger the flare eruption. The flare occurred at S12W08 and was accompanied by a very fast CME: the projected speed achieved $\cong 2400\text{km/s}$ (Möstl et al., 2015). Figure 3.10 (a)-(c) show

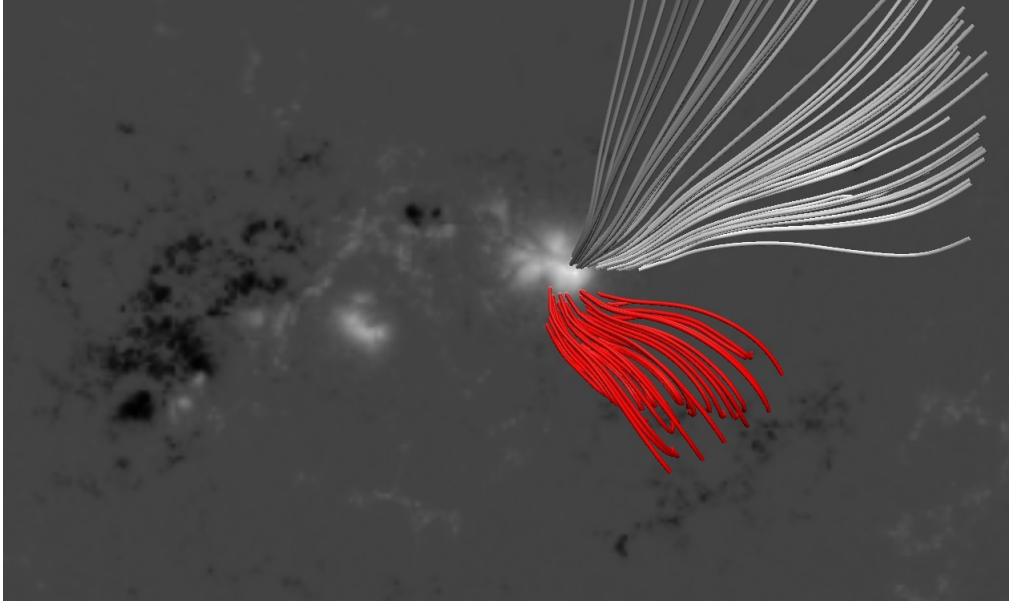


Figure 3.11: Selected NLFFF reconstruction of coronal field lines for event #29 at Jan 7 17:00 UT. The white field lines stand for the open field lines nearby the core region, while the red field lines are the reconstructed field lines where the initial flaring starts.

the evolution of this event as seen by SDO/AIA 171Å observations. The flaring position is roughly located between two ARs: AR11944 and AR11943. A coronal sigmoid links the two ARs and can be clearly seen on Jan 7 13:51UT (indicated by the arrow shown in Figure 3.10 (a)), about one day before the flare onset. The sigmoid gets faint just before the flare onset thus we can hardly recognize the corresponding field line structures until the sudden brightening of the flare onset. Figure 3.10 (b) shows the moment the sigmoid erupts (indicated by the white arrow). After the eruption, a post flare arcade connecting the two ARs is formed (white arrow in Figure 3.10 (c)) and the flare ribbons are observed afterwards (red contours shown in Figure 3.10 (d), from AIA 1600Å observation).

To further examine the magnetic structure of this event, we again compare the NLFFF results to the coronal structure as seen in AIA 171Å observations. The selected extrapolated field lines plotted in Figure 3.11 present the magnetic field structure in the core region (red field lines) and the open field lines (white field lines). A bundle of open field lines is consistent with the structure captured in AIA 171Å yet the red field lines are less twisted than seen in Figure 3.10, implying that the extrapolation did not correctly reproduce the sigmoid which is expected to initiate the eruption.

We speculate that the NLFFF extrapolation fails to capture the real coronal topology of this AR prior to this event. One possible reason is that the MHD-relaxation finds the best-fit answer according to the observation at photosphere but in this case the flare location is not near well-measured sunspots and the measurements may be poor. Secondly, the target flux rope has an extremely large spatial scale which implies it may also extend to very high altitude, out of the normal bounds for the NLFFF extrapolation. Wang et al. (2015) also studied this AR and event, and tried to reconstruct the coronal field using a different NLFFF extrapolation method and boundary condition. The authors found that the flux rope which was supposed to be ejected and become the CME could not be reconstructed. They suggested that the flux rope was a very dynamic structure, and a model based on a static snapshot could not fully capture the real magnetic field structure.

3.3 Summary and Conclusion

In this study, we study a parameter with the goal of helping determine the potential for eruptivity of a flare. Among 51 analyzed flares with classification $\geq M5.0$, the coronal magnetic field structures are analyzed via NLFFF coronal magnetic field models prior to the event. We tested the hypothesis that eruptivity can be expressed as the equilibrium balance between the force that accelerates CME material and the downward force that confines any eruption. By using a parameter r_m to relate the balance of upward- and downward-directed forces, we tested the hypothesis that the force balance can be approximated by the ratio of the reconnected magnetic flux over the suppression flux. We conclude that r_m can provide a moderate ability for distinguishing the eruptive and confined events. We note that while we aimed to apply this parameter to CME forecasting, its predictive ability is restricted since it can only be determined when the information of flare ribbon location is provided (i.e., after the event has begun).

To estimate the reconnected flux before the eruption, we use the highly twisted flux as the proxy of the reconnected flux. As Muhamad et al. (2018) indicated that this technique will be sensitive to the threshold (T_c) chosen to define the highly twisted flux, we compared the highly twisted flux varies with different T_c to the ribbon flux in order to confirm the most appropriate T_c . It turns out that using a much lower threshold than expected ($T_c = 0.2$) may provide a proxy for the reconnection flux. This finding can be explained by the tether cutting model proposed by Moore et al. (2001) since the model predicts that the less twisted field lines will reconnect and build up the core region in the later phase of the eruption. Not only are the values of the highly twisted regions sufficiently representative of the ribbon flux, we find that the footpoints of these field lines are spatially consistent to the ribbon pattern, which agrees with the results of a case study in Inoue

et al. (2011).

In this study, we evaluate the ratio between repulsive force and the suppression force based on a morphological identification. According to the topological properties of field lines, two hypotheses are proposed and tested. By testing our hypotheses of the surrounding field lines, we found that not only the overlying field lines but also the the wall field can confine the eruption process. Through discriminant analysis (Figure 3.9), we demonstrate that by including the term Φ_{wall} , the eruptive events and confined events become more separated in the r_m parameter space. Furthermore, the classification performance (Tables 3.4 and 3.5) indicate that including the contribution of wall field could improve the results.

However, there is a large degree of overlap between the two small sample sets. We suggest several factors that may reduce the difference between two groups: first, even as we have confirmed the structures computed by the NLFFF extrapolations by comparing the models to coronal observations, there might still be some invisible structures not yet captured by the NLFFF models because they do not follow the force-free assumptions (*e.g.*, event #29 from Table 2.1). An inaccurate model will lead to an incorrect estimation of r_m . Second, as the selection of highly twisted region relies on manually identifying the target areas according to the flare ribbon locations, the overestimation/underestimation of $\Phi_{T_w \geq T_c}$ can cause an incorrect r_m . Finally, there may of course exist some other physical characteristics that haven't yet been revealed. For example, much larger context magnetic structures around the eruption site may affect its eruptivity, as discussed in DeRosa & Barnes (2018).

Chapter 4

Eruptivity in Solar Flares: The Challenges of Finding the Magnetic Flux Rope

In the previous chapter, a proposed parameter “ r_m ”, which is the ratio of the magnetic fluxes as defined to approximate the force balance of an erupt-imminent magnetic flux rope (MFR), is shown to independently be able to determine the association of a flare with an accompanying coronal mass ejection (CME), but only at a moderate level. In this context, three events originating from NOAA Active Region (AR) 12192 are failed to be correctly assigned by this parameter. It is worth noting that the solar active region 12192, while an extremely large AR, generated a succession of CME-less flares (Chen et al., 2015, Sun et al., 2015, Thalmann et al., 2015). The atypical AR consequently arose our great interests to investigate the reasons for causing the exceptional events originating from AR 12192.

In this chapter, we aim to investigate further the mechanism of CME-initialization through the three incorrectly-classified events as they appear in the r_m scheme. Recalling that r_m arises from the concept that a CME will erupt if the force that drives the eruption of MFR overtakes the magnetic confinement from its surroundings. We therefore postulate that there might be two major factors for causing the mis-classified events: first, the ratio of magnetic fluxes is improper to approximate the force balance; second, the imposed threshold ($|T_w| > 0.2$) cannot not capture the true structure of the erupting MFR. With the hypotheses above are tested, we apply the identical methodology as §3 used such that we can make a meaningful comparison with the conclusions from the previous

chapter.

This chapter covers the second part of the thesis, which is organized as follows: in §4.1, we review r_m and describe its failure to classify three confined events from NOAA AR 12192. In §4.2, we analyze what factor(s) cause these three mis-classified events, propose and apply different approaches that each deploy different descriptions of the relevant flux systems, and evaluate their classification results. Next, the results are discussed in §4.3 in the context of MHD instabilities and the flares’ behaviors. Finally, §4.4 summarizes and concludes this research.

4.1 Exceptional events under the r_m -scheme from NOAA AR 12192

NOAA Active Region 12192 appeared in 2014 October containing one of the largest sunspots of Cycle 24. It produced more than 140 flares larger than C1.0 class (Bamba et al., 2017). However, these events were atypical since no CME was reported to originate from the core of this AR, only from its periphery (Chen et al., 2015, Panesar et al., 2016, Thalmann et al., 2015). Table 4.1 lists the relevant flare data as recorded by the *Geostationary Operational Environmental Satellite (GOES)* for the “exceptional” flares, meaning three events from this region which the r_m scheme incorrectly classified as belonging to the “eruptive” population. In addition to these three mis-classified events, three other events from AR 12192, one M-class flare and two X-class events, were correctly classified as “confined”. The flares listed in Table 4.1 were also analyzed by Thalmann et al. (2015), where their homologous nature is presented: they are all similar in terms of the integrated properties of flare ribbons, the morphology of the ribbon patterns, and the huge separation between the two early-stage flare ribbons with no evidence of flare-ribbon progression in the lateral direction. Furthermore, Sun et al. (2015) found that AR 12192 had weak nonpotentiality, and Inoue et al. (2016) also concluded that the magnetic configuration prior to the X3.1 flare (event #37) was stable against the KI. The strong overlying magnetic confinement found for the Table 4.1 targets in these recent studies was found through the simple ratio of magnetic field strengths at differing altitudes (Jing et al., 2015, Sun et al., 2015, Thalmann et al., 2015).

In contrast to these studies, the results presented in §3 suggested that the events listed in Table 4.1 host sufficiently high values of r_m to be classified as eruptive. Figure 4.1 shows the Solar Dynamics Observatory (SDO) / Atmospheric Imaging Assembly (AIA) observations and the coronal magnetic fields reconstructed from NLFFF extrapolations for these events. Figure 4.1 (a)-(c) show SDO/AIA 94 Å images taken roughly 1 hour prior to the *GOES* flare start time (that is, the time we have used to construct the nonlinear force-free field; NLFFF magnetic field), whereas Figure 4.1 (d)-(e) present the AIA 94 Å observations taken at the *GOES* peak time listed in Table 4.1.

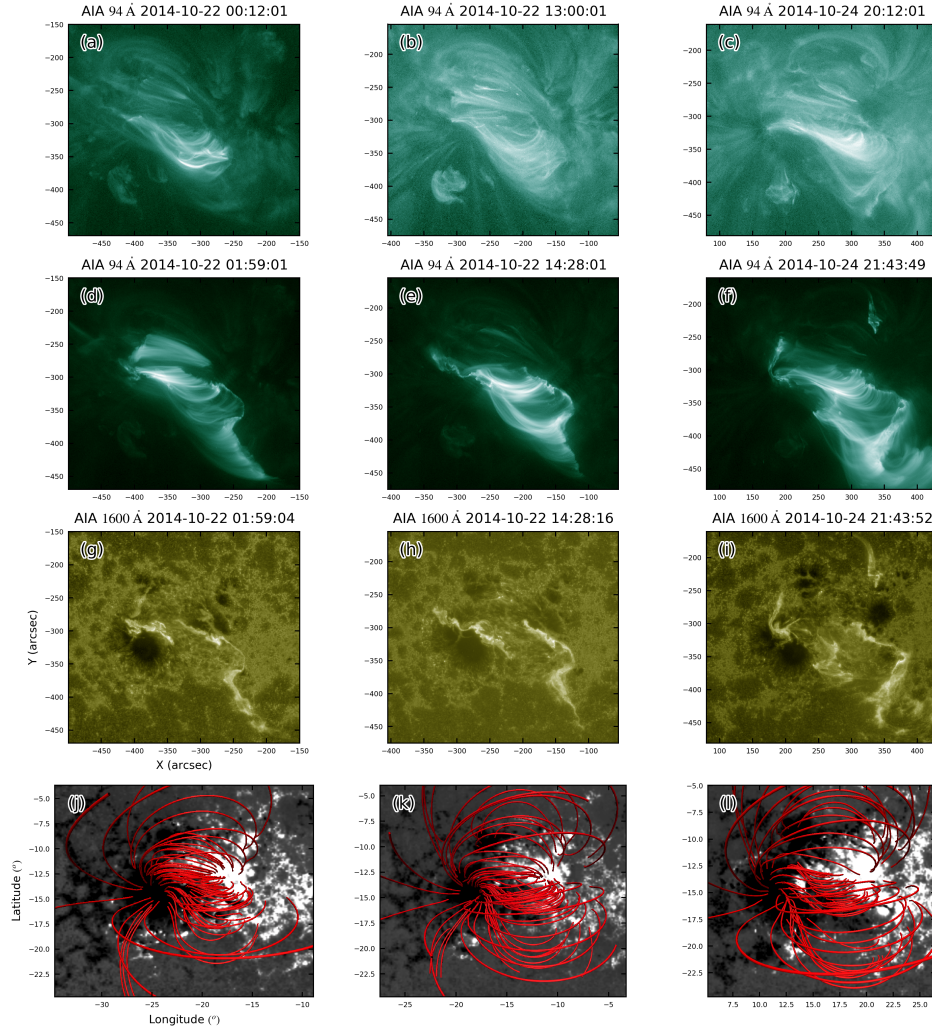


Figure 4.1: (a)-(c) SDO/AIA 94 Å observations of AR 12192 taken at time roughly one hour prior to the *GOES* flare start time of event #35, #36, and #37, respectively. (d)-(f) The same as in (a)-(c), but taken at the *GOES* flare peak time. (g)-(i) SDO/AIA 1600 Å observations on the same time and the identical FOV with (d)-(f). (j)-(l) NLFFF extrapolation results of AR12192 overlaid on SHARP magnetogram data (saturated at ± 500 Gauss). Red lines represent the selected magnetic field lines from the NLFFF extrapolation.

Event#	<i>GOES</i> Start Time ^a	<i>GOES</i> Peak Time ^b	<i>GOES</i> End Time ^c	<i>GOES</i> Class ^d
35	2014-10-22T01:16	2014-10-22T01:59	2014-10-22T02:28	M8.7
36	2014-10-22T14:02	2014-10-22T14:28	2014-10-22T14:50	X1.6
37	2014-10-24T21:07	2014-10-24T21:41	2014-10-24T22:13	X3.1

^a The start time of the flare according to *GOES* catalog.

^b The peak time of the flare according to *GOES* flare catalog.

^c The end time of the flare according to *GOES* flare catalog.

^d Flare class from the *GOES* flare catalog.

Table 4.1: r_m -exception events for analysis

In each image, one can see the hot coronal loops created through the flares. At the footpoints of these coronal loops, the corresponding emission can be observed in AIA 1600 Å passbands (Figure 4.1 (g)-(i)), implying that these coronal loops trace the magnetic structures where reconnection has occurred. Chen et al. (2015) confirmed that all of the X-class flares from this active region had similar flaring structures as seen in AIA 94 Å images. We see here, too, that the coronal loops visible in AIA 94 Å data and the related flare ribbons visible in 1600 Å images are morphologically similar among these flares, consistent with the homologous character discussed above. The overall twist value is generally less than one-half, consistent with the lack of any clearly visible sigmoidal structure, yet we can recognize inverse-S-shape structures in the SDO/AIA 94 Å images (Figure 4.1 (a)-(c)) and in the reconstructed NLFFF magnetic field (Figure 4.1 (j)-(l)). These structures provide evidence of a flux rope buildup (Green & Kliem, 2009, Green et al., 2011, Savcheva et al., 2012), and we suggest that the bright coronal loops indicate the core part of the flares. It is worth noting that the low-twist magnetic configurations presented in the NLFFF constructions shown here are consistent with the reconstructions by Inoue et al. (2016) and Jiang et al. (2016) using different NLFFF extrapolation schemes. Regarding the magnetic field above the core region, we have calculated the horizontal component of the magnetic field directly above the PIL at the height of 42 Mm to directly compare with the model used in Sun et al. (2015), and we find comparable horizontal field strengths. This implies that the cause(s) of the incorrect classification by r_m is not due to problems with the NLFFF model employed here.

4.2 Analysis

In this section, we explore factors that may have led to the incorrect eruptive-potential diagnosis of AR 12192 by the r_m parameter. Two hypotheses are presented here for testing: first, that the ratio of magnetic fluxes used as the approximation for the force balance (Equation (3.2)) could be better estimated by the ratio of other physical quantities. Second, we postulate that using the threshold $\Phi_{|T_w| \geq 0.2}$ cannot adequately approximate $\Phi_{\text{reconnect}}$ to which an MFR will contribute. In this section, we motivate and test these hypotheses.

4.2.1 Testing hypothesis #1: the r_τ parameter and r_κ parameter

As described above, r_m is defined as the ratio of magnetic flux of the footpoints of different bundles of field lines (see Equation (3.2)). Here we investigate whether the success of the eruptive assignment can be improved by replacing magnetic flux with other physical quantities.

Magnetic twist flux density (τ) was introduced by Kusano et al. (2020):

$$\tau = T_w |B_z|, \quad (4.1)$$

where B_z is the same radial (normal) magnetic field component used to calculate total flux (here we use the lower boundary of the NLFFF extrapolation, for which B_z is held fixed during relaxation), and T_w is the wind number (Equation (3.4)). Based on Equation (4.1), the “magnetic twist flux” (Φ_τ) is therefore computed as

$$\Phi_\tau = \int \tau dS, \quad (4.2)$$

where dS is a finite element in the surface integral on the photosphere. Φ_τ is used to estimate κ , a critical parameter used to evaluate the DAI (Ishiguro & Kusano, 2017). DAI is proposed to explain the onset of a double-arc coronal loop formed through tether-cutting reconnection (Moore et al., 2001), hence Φ_τ can be considered a measure of the capability for an AR to trigger an energetic event. Replacing the magnetic flux (Φ) in Equation (4.3) with the magnetic twist flux, we define a new parameter:

$$r_\tau = \frac{\Phi_{\tau \ T_w \geq T_c}}{\Phi_{\tau \ T_w \geq T_c} + \Phi_{\tau \ \text{surrounding}}}. \quad (4.3)$$

Where the Φ_τ relies on the field-line twist (T_w), thus we impose the threshold $T_c = 0.2$ and include only those footpoints for magnetic field lines with $|T_w| \geq T_c$; here $|T_w| \geq 0.2$ is for Φ_τ , and no such limit is used for $\Phi_{\tau \ \text{surrounding}}$. According to the theoretical definition of κ , the area integral for

calculating Φ_τ is taken over the region where the tether-cutting reconnection has extended (S_{rec}). A magnetogram cannot provide the information of the location and extent of S_{rec} independently, hence its implementation has varied: Muhamad et al. (2018) approximated S_{rec} as areas with associated field lines that have $T_w > 0.5$. Kusano et al. (2020) assumed that S_{rec} was a circular region centered at points along a PIL, calculating the corresponding κ value along the full PIL to find the location most unstable against DAI. Since our objective is to explore whether using other physical quantities can improve the assignment of eruptive or confined across all events, we vary only one thing at a time and consequently use the same area integral as in §3, specifically the area with $|T_w| \geq 0.2$. Similarly, when estimating Φ_τ overlying and Φ_τ wall, we apply the identical procedure for selecting those field lines, summarized as:

- *Highly twisted field*: fieldlines where $|T_w| \geq 0.2$; closed fieldlines lying near that PIL involved in the flare and hence near, but not necessarily cospatial with, the flare ribbons.
- *Overlying field*: closed fieldlines lying above the highly twisted region; excludes highly twisted field.
- *Wall field*: fieldlines with one foot point near the highly twisted field (≤ 10 Mm), and the other footpoint away from it, but still must be closed; excludes highly twisted field.

To avoid large uncertainties we only consider data where the radial component of the magnetic field strength exceeds 250 Gauss, a somewhat conservative but otherwise arbitrary threshold above which the derived magnetic flux was not sensitive.

As a further refinement, consider that the original definition of κ was given by the ratio of magnetic twist flux (Φ_τ) over the magnetic flux (Φ). We extend this to:

$$r_\kappa = \frac{\Phi_\tau T_w \geq T_c}{\Phi_{T_w \geq T_c} + \Phi_{\text{surrounding}}}, \quad (4.4)$$

which differs from Equation (4.3) in that the denominator in Equation (4.4) is Φ instead of Φ_τ . The parameters κ and r_κ are formulated from the concept that the magnetic flux (Φ) rather than the magnetic twist flux (Φ_τ) that should work to suppress eruption.

Thus we now have 3 different parameters, r_m , r_τ , and r_κ , all of which assume that field lines with large T_w can approximate the MFR's field lines. We group these parameters as the r -scheme for estimating the likelihood of a flare being an eruptive flare. One should note that all parameters are based on the ratio of the driving force to the suppressing force, as estimated using flux (or

twist flux) corresponding to twisted field lines (driving) in the numerator and flux (or twist flux) corresponding to field lines that could be involved with suppression in the denominator. We highlight the differences of the numerator and denominator sources of footpoint flux here:

- r_m^o : ratio of magnetic flux; numerator: field lines where $|T_w| \geq 0.2$; denominator: overlying field only.
- r_m^{o+w} : ratio of magnetic flux; numerator: field lines where $|T_w| \geq 0.2$; denominator: overlying field and wall field.
- r_τ^o : ratio of magnetic twist flux; numerator: field lines where $|T_w| \geq 0.2$; denominator: overlying field only.
- r_τ^{o+w} : ratio of magnetic twist flux; numerator: field lines where $|T_w| \geq 0.2$; denominator: overlying field and wall field.
- r_κ^o : ratio of magnetic twist flux over magnetic flux; numerator: field lines where $|T_w| \geq 0.2$; denominator: overlying field only.
- r_κ^{o+w} : ratio of magnetic twist flux over magnetic flux; numerator: field lines where $|T_w| \geq 0.2$; denominator: overlying field and wall field.

The quantities used to calculate Equations (4.3) and (4.4), and the resulting r_τ^o , r_τ^{o+w} , r_κ^o and r_κ^{o+w} are presented in Table 4.2, with the corresponding uncertainties quoted in the table header (see Appendix B for the estimation of uncertainty). The deduced uncertainties of the Φ results are generally less than 10%, although those for some Φ_τ parameters are larger, reaching just over 25%. We suggest that this is due to the propagation of errors through the NLFFF extrapolation, influencing those quantities involving the twist number (which is computed using the NLFFF construction). The zero values that appear in event #29 are due to there being no field lines in the flare-ribbon area that satisfy the threshold ($|T_w| \geq 0.2$); hence all values are assigned zero. The distributions of r_τ^o , r_τ^{o+w} , r_κ^o and r_κ^{o+w} are shown in Figure 4.2. We find that the average value of the eruptive events are always greater than the confined events in each parameter (which are denoted by the red and black dashed lines in Figure 4.2, respectively). Moreover, the values of r_τ are overall higher than r_κ , owing to the smaller denominator (see Equation (4.3)): the coronal field lines generally have $|T_w| < 1$, hence in general, $\Phi > \Phi_\tau$.

Event#	$\Phi_{T_w \geq T_c}$ $\pm 0.6\%^a$ (10^{20}Mx)	$\Phi_{\tau, T_w \geq T_c}$ $\pm 5.3\%$ (10^{20}Mx)	$\Phi_{\text{overlying}}$ $\pm 9.8\%$ (10^{20}Mx)	$\Phi_{\tau, \text{overlying}}$ $\pm 28.6\%$ (10^{20}Mx)	Φ_{wall} $\pm 1.3\%$ (10^{20}Mx)	$\Phi_{\tau, \text{wall}}$ $\pm 10.2\%$ (10^{20}Mx)	r_{τ}^a ^b $\pm 3.3\%$	r_{τ}^{a+w} ^c $\pm 6.7\%$	r_{κ}^d ^d $\pm 3.1\%$	r_{κ}^{a+w} ^e $\pm 5.1\%$
1	29.52	12.97	6.45	1.25	51.29	4.03	0.91	0.71	0.36	0.15
2	36.54	17.49	8.21	1.16	93.55	9.81	0.94	0.61	0.39	0.13
3	17.93	6.09	40.15	2.51	25.65	3.31	0.71	0.51	0.10	0.07
4	7.27	2.58	9.31	1.16	11.23	0.96	0.69	0.55	0.16	0.09
5	18.77	6.97	16.16	1.60	24.53	2.21	0.81	0.65	0.20	0.12
6	25.90	9.34	12.52	1.25	32.70	2.21	0.88	0.73	0.24	0.13
7	13.80	4.93	5.61	0.43	16.74	0.59	0.92	0.83	0.25	0.14
8	15.53	6.76	6.57	0.41	16.19	0.52	0.94	0.88	0.31	0.18
9	12.48	5.85	13.48	1.28	17.50	0.61	0.82	0.76	0.23	0.13
10	2.91	0.93	17.32	0.93	3.78	0.45	0.50	0.40	0.05	0.04
11	136.77	52.15	144.36	10.72	17.88	1.09	0.83	0.82	0.19	0.17
12	124.61	47.73	144.58	11.00	24.63	1.64	0.81	0.79	0.18	0.16
13	122.62	42.51	107.94	9.59	12.76	0.61	0.82	0.81	0.18	0.17
14	37.66	13.25	52.18	3.20	27.03	1.97	0.81	0.72	0.15	0.11
15	6.31	3.25	18.58	2.74	36.44	3.17	0.54	0.35	0.13	0.05
16	4.80	1.35	6.91	0.74	15.36	0.93	0.65	0.45	0.12	0.05
17	4.61	1.66	21.47	4.86	65.38	7.52	0.25	0.12	0.06	0.02
18	4.24	1.62	24.13	5.94	68.58	7.99	0.21	0.10	0.06	0.02
19	67.46	24.87	75.98	7.61	77.16	8.08	0.77	0.61	0.17	0.11
20	5.51	1.38	5.22	0.33	13.45	1.21	0.81	0.47	0.13	0.06
21	6.42	3.22	7.16	0.71	14.06	1.15	0.82	0.63	0.24	0.12
22	7.45	3.12	12.13	1.21	22.97	1.97	0.72	0.50	0.16	0.07
23	5.67	2.17	14.17	0.78	9.54	0.87	0.74	0.57	0.11	0.07
24	10.74	4.61	28.55	3.05	59.92	3.66	0.60	0.41	0.12	0.05
25	12.31	3.16	68.21	4.55	12.64	1.00	0.41	0.36	0.04	0.03
26	9.88	5.13	25.97	2.08	25.87	3.20	0.71	0.49	0.14	0.08
27	20.83	6.60	15.55	1.37	43.14	3.95	0.83	0.55	0.18	0.08
28	10.87	4.91	62.11	4.46	48.35	4.19	0.52	0.36	0.07	0.04
29	0	0	0	0	0	0	0	0	0	0
30	33.00	15.24	31.23	2.81	61.51	5.62	0.84	0.64	0.24	0.12
31	11.57	4.34	4.49	0.35	3.17	0.06	0.93	0.91	0.27	0.23
32	5.33	1.40	15.32	1.15	13.09	0.99	0.55	0.40	0.07	0.04
33	48.11	14.27	67.60	6.94	15.24	1.21	0.67	0.64	0.12	0.11
34	35.88	10.86	35.54	3.45	61.11	4.06	0.76	0.59	0.15	0.08
35	121.10	42.14	137.76	16.54	185.04	12.96	0.72	0.59	0.16	0.09
36	158.06	52.17	132.80	15.00	202.44	12.45	0.78	0.66	0.18	0.11
37	111.71	32.82	98.00	13.44	187.26	17.95	0.71	0.51	0.16	0.08
38	40.56	13.49	89.32	15.93	186.15	19.89	0.46	0.27	0.10	0.04
39	35.74	10.77	44.45	5.79	197.15	17.95	0.65	0.31	0.13	0.04
40	43.25	15.51	52.51	5.52	239.52	21.73	0.74	0.36	0.16	0.05
41	42.54	15.88	38.69	3.94	29.68	1.71	0.80	0.74	0.20	0.14
42	5.55	1.46	29.71	2.77	21.26	1.52	0.34	0.25	0.04	0.03
43	67.96	21.12	21.99	2.37	52.87	5.14	0.90	0.74	0.23	0.15
44	47.47	18.08	33.83	2.93	19.79	2.71	0.86	0.76	0.22	0.18
45	66.90	22.17	81.90	8.26	45.94	4.94	0.73	0.63	0.15	0.11
46	5.16	1.88	0.56	0.03	11.31	0.58	0.99	0.76	0.33	0.11
47	9.66	4.28	14.35	2.32	63.24	12.71	0.65	0.22	0.18	0.05
48	71.05	32.00	65.79	6.72	20.47	1.48	0.83	0.80	0.23	0.20
49	48.55	15.41	73.60	7.59	31.12	2.73	0.67	0.60	0.13	0.10
50	0.75	0.34	12.59	0.82	11.73	1.48	0.29	0.13	0.03	0.01
51	5.66	2.13	22.75	2.67	46.91	4.94	0.44	0.22	0.08	0.03

^a The uncertainties are presented assuming all magnetic fluxes estimated in event #1 are representative.

^b r_{τ} calculated based on hypothesis 1 ($\Phi_{\tau, \text{surrounding}} = \Phi_{\tau, \text{overlying}}$).

^c r_{τ} calculated based on hypothesis 2 ($\Phi_{\tau, \text{surrounding}} = \Phi_{\tau, \text{overlying}} + \Phi_{\tau, \text{wall}}$).

^d r_{κ} calculated based on hypothesis 1 ($\Phi_{\text{surrounding}} = \Phi_{\text{overlying}}$).

^e r_{κ} calculated based on hypothesis 2 ($\Phi_{\text{surrounding}} = \Phi_{\text{overlying}} + \Phi_{\text{wall}}$).

Table 4.2: Estimations related to r_{τ} and r_{κ}

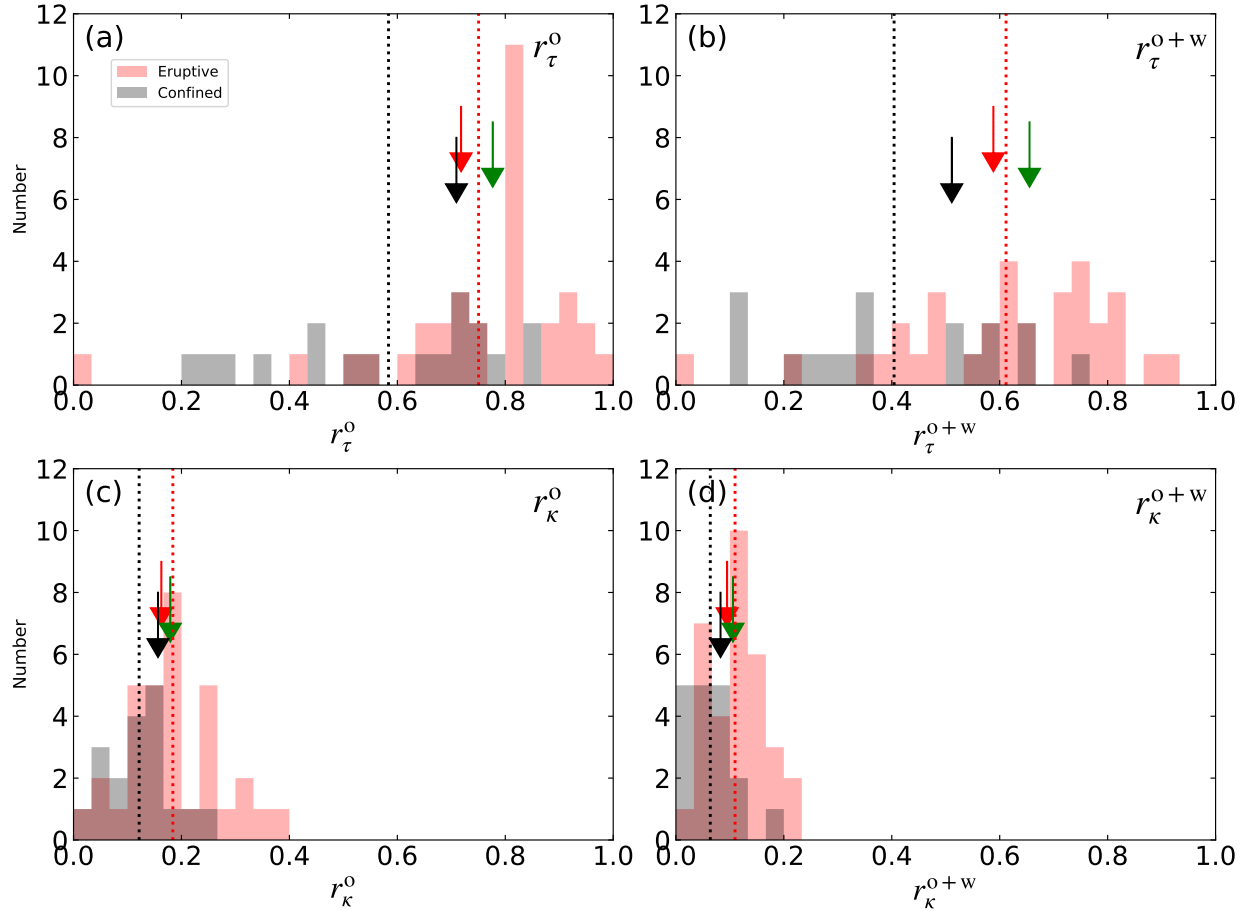


Figure 4.2: Histograms of (a) r_τ^o , (b) r_τ^{o+w} , (c) r_κ^o , and (d) r_κ^{o+w} for eruptive events (shaded red) and confined events (shaded grey). Red (black) vertical dash lines indicate the mean value of the variables for eruptive (confined) events. The arrows colored in red, green, and black indicate the value which events #35, #36, and #37 host, respectively.

With the resulting r_τ^o , r_τ^{o+w} , r_κ^o and r_κ^{o+w} across all 51 events, we test the ability of these variables to distinguish between eruptive and confined through the application of linear DA. The statistical metrics used to judge the discrimination of these variables are summarized in Table 4.3. The results from these statistical metrics demonstrate that the eruptivity can be classified using the parameters proposed here, however as acknowledged in §3, a large overlap of the two distributions implies that still-unknown physical mechanisms are involved in triggering energetic events.

Parameter	Mehod	Statistical Metrics			
		Probability (%)	MD ^a	CR ^b	TSS
r_m^o	Original	94%	0.63	0.65	0.15
	Monte Carlo	93.9% ±0.4	0.63±0.02	0.66±0.01	0.17±0.02
	Bootstrap	84.5±17.4%	0.59±0.41	0.67±0.07	0.14±0.18
r_m^{o+w}	Original	96.9%	0.85	0.73	0.37
	Monte Carlo	96.9±0.2%	0.85±0.02	0.73±0.01	0.38±0.02
	Bootstrap	89.8±12.7%	0.78±0.57	0.69±0.07	0.20±0.19
r_τ^o	Original	95.1%	0.7	0.71	0.24
	Monte Carlo	87.1±21.0%	0.74±0.41	0.70±0.04	0.21±0.13
	Bootstrap	86.0±18.3%	0.75±0.58	0.69±0.07	0.18±0.17
r_τ^{o+w}	Original	98.2%	1.03	0.76	0.43
	Monte Carlo	91.1±19.1%	0.98±0.47	0.71±0.04	0.29±0.15
	Bootstrap	93.0±10.4%	0.98±0.61	0.72±0.07	0.27±0.20
r_κ^o	Original	93.1%	0.59	0.68	0.21
	Monte Carlo	83.5±21.3%	0.52±0.26	0.66±0.04	0.09±0.12
	Bootstrap	84.9±16.7%	0.57±0.35	0.66±0.07	0.10±0.17
r_κ^{o+w}	Original	96.6%	0.82	0.67	0.28
	Monte Carlo	79.6±25.0%	0.52±0.33	0.66±0.04	0.11±0.16
	Bootstrap	89.7±12.9%	0.76±0.49	0.68±0.06	0.18±0.18

^a Mahalanobis distance for the sample PDFs.

^b Correct rate of the classification table.

Table 4.3: DA results (with $n - 1$ cross-validation) of the parameters in r -scheme

For each of the DA-produced metrics presented in Table 4.3, we provide uncertainties derived by Monte Carlo and 100-draw bootstrap algorithms. The Monte Carlo algorithm measures the uncertainties arising from the uncertainties in the observations, while the bootstrap measures the uncertainties generated by the sampling process (see Appendix B for further details on these two

techniques). A comparison of all metrics and their uncertainties are presented in Figure 4.3 (the q -parameters are discussed in §4.2.2). The rather large uncertainties in r_τ and r_κ implies that we have too small a sample size in this study to accurately estimate the true distributions of each population.

According to the metrics presented in Table 4.3 and Figure 4.3, we find that r_τ^{o+w} show larger values than other parameters: for example, the higher probability that two samples are from different populations suggests that using r_τ^{o+w} may better distinguish the eruptive from confined populations; although the value of the probability is still insufficient to definitively state that the samples are from distinct populations. The larger Mahalanobis distance, correct rate (RC), and True Skill Statistic (TSS, computed as with RC using a probability threshold of 0.5) all indicate that eruptive and confined events are more separated by the r_τ^{o+w} measure. In spite of the performance of r_τ^{o+w} being ostensibly superior to r_m^{o+w} , this does not guarantee that the latter is the best-performing variable, due to the small sample size and resulting large uncertainties (see Figure 4.3). In general, compared to the r_m^o and r_m^{o+w} parameters discussed in §3, all parameters listed in Table 4.2 remains at a “moderate” level in evaluating the eruptivity of the flares. Of note, the $n - 1$ cross-validation results show that the three targeted events (event #35, #36, and #37) are still classified as “eruptive” even with the newly refined parameters. In other words, the values of the newly-proposed parameters for these three events do not decrease compared to the other events, and according to the DA, approximating the force balance by other physical quantities, such as Φ_τ , cannot fix the classification errors in these three cases.

4.2.2 Testing hypothesis # 2 with the q-schemes: q_m , q_τ , and q_κ

Here we test the second hypothesis, “ $\Phi_{|T_w| \geq 0.2}$ cannot adequately approximate the $\Phi_{reconnect}$ which is contributed by an MFR”. We have shown that modifying the scheme of r_m to use the ratio of other physical quantities (*i.e.*, r_τ and r_κ), still resulted in the three targeted events being incorrectly classified as eruptive events. The problem now narrows to how to verify whether the threshold of $|T_w| \geq 0.2$ is a proper criterion for these targeted events. To do this, we test the option of instead using the flare-ribbon emission area, which is regarded to be a more direct approximation of the reconnected magnetic flux. It is widely regarded that flare ribbons are strongly related to magnetic reconnection, as it is the precipitation of the energetic particles released by magnetic reconnection which is believed to cause emission in H α line-center and the 1600 Å bandpass (Forbes, 2000, Qiu et al., 2012). The area “swept” by flare ribbons has a quantitative relationship to the magnetic reconnection progress (Priest & Forbes, 2002, Qiu et al., 2012). According to the well-known CSHKP “standard flare” model (Carmichael, 1964, Hirayama, 1974, Kopp & Pneuman,

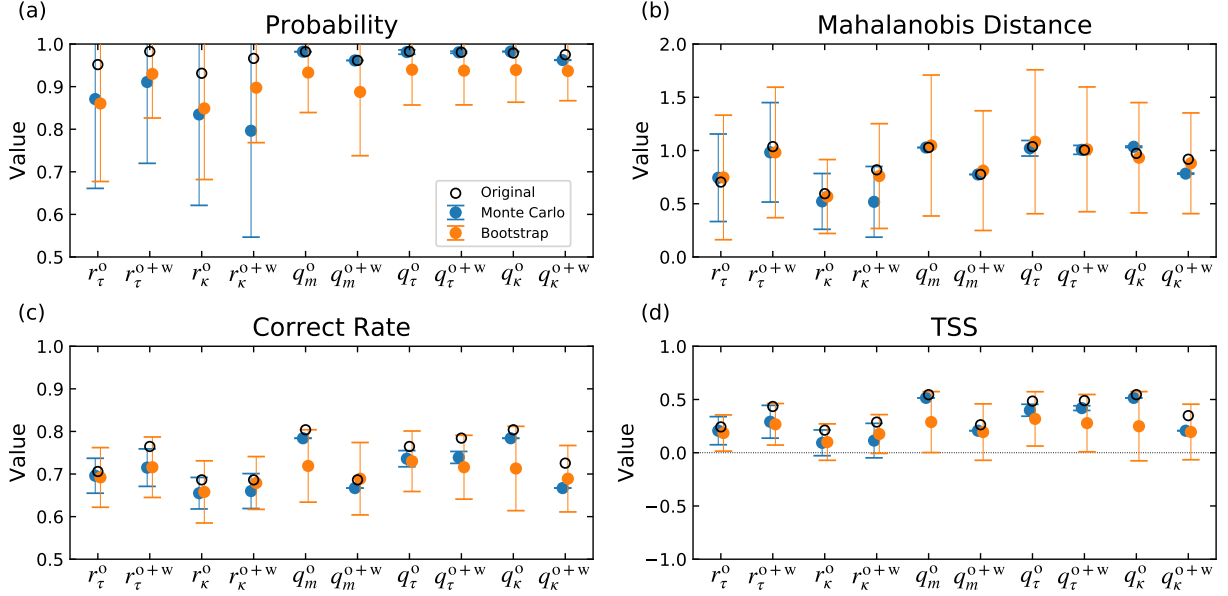


Figure 4.3: The comparison of the resulting DA metrics for r -scheme (r_τ^o , r_τ^{o+w} , r_κ^o , and r_κ^{o+w}) and q -scheme (q_m^o , q_m^{o+w} , q_τ^o , q_τ^{o+w} , q_κ^o and q_κ^{o+w}). The metrics are (a) The probability that two groups are sampled from two distinct populations; (b) Mahalanobis distance; (c) correct rate and (d) TSS. The non-filled black circles indicate the value yielded through the $n - 1$ cross-validation. The data points and the associated error bars colored in blue (orange) stand for the estimations yielded from the Monte-Carlo algorithm (bootstrap method). A horizontal dashed line in (d) divides the space of positive and negative skill for the classification.

1976, Sturrock, 1966), which was extended to 3-D by Longcope et al. (2007), the flare-ribbon area corresponds to where newly-reconnected field lines anchor on the solar surface. Based on the 3-D version of the CSHKP model, Kazachenko et al. (2017) showed the relation between peak X-ray flux and the flare-ribbon area's magnetic flux, demonstrating that the amount of energy released by magnetic reconnection can be directly deduced from the measurement of flare ribbon area and its associated magnetic flux.

By using the flare-ribbon-defined magnetic flux as a representation of the reconnected magnetic flux, we propose the q -scheme, which is a modified version of the aforementioned r -scheme. The q -scheme includes the parameters defined as follows:

$$q_m = \frac{\Phi_{\text{Ribbon}}}{\Phi_{\text{Ribbon}} + \Phi_{\text{surrounding,R}}}, \quad (4.5)$$

$$q_\tau = \frac{\Phi_\tau \text{ Ribbon}}{\Phi_\tau \text{ Ribbon} + \Phi_\tau \text{ surrounding,R}}, \quad (4.6)$$

$$q_\kappa = \frac{\Phi_\tau \text{ Ribbon}}{\Phi_{\text{Ribbon}} + \Phi_{\text{surrounding,R}}}, \quad (4.7)$$

where $\Phi_{\text{surrounding,R}}$ indicates that the surrounding field is defined based on the flare-ribbon area. We now have 6 new variables:

- q_m^o : ratio of magnetic flux; numerator: ribbon-associated-magnetic field; denominator: overlying field only.
- q_m^{o+w} : ratio of magnetic flux; numerator: ribbon-associated-magnetic field; denominator: overlying field and wall field.
- q_τ^o : ratio of magnetic twist flux; numerator: ribbon-associated-magnetic field; denominator: overlying field only.
- q_τ^{o+w} : ratio of magnetic twist flux; numerator: ribbon-associated-magnetic field; denominator: overlying field and wall field.
- q_κ^o : ratio of magnetic twist flux over magnetic flux; numerator: ribbon-associated-magnetic field; denominator: overlying field only.
- q_κ^{o+w} : ratio of magnetic twist flux over magnetic flux; numerator: ribbon-associated-magnetic field; denominator: overlying field and wall field.

It is important to note that the q -scheme approximates the MFR's footpoints by the area covered by flare ribbons as seen in 1600Å wavelengths, rather than the area of high field-line twist number as in the r -scheme. According to the 3-D version of the CSHKP model, during the flare-eruption process the newly-reconnected field lines in the immediate vicinity of a PIL are progressively incorporated into the reconnection, hence the brightening patterns gradually progress in space during the flare. We define as the flare-ribbon area all pixels that increased in brightness above a specified intensity threshold between the flare start time and end times as listed in the *GOES* catalog. The sensitivity of our analysis to the brightness threshold is discussed in Appendix C.

However, prior to constructing the mask, we remove the saturated pixels in the AIA 1600 Å channel images due to overexposure throughout the flaring period. We first remap the 24-s cadence 1600 Å AIA data sequence, from the CCD coordinates into the CEA projections, to match the HMI SHARP data used for the NLFFF extrapolation. We then follow the procedures described in

Kazachenko et al. (2017), but adjust the value of the threshold for identifying the saturated pixels (to $I_{sat} = 9000 \text{ counts} \cdot \text{s}^{-1}$). The temporal interpolation is performed over the time range from the *GOES*-listed start time to the end time.

Figure 4.4 shows the saturation-corrected image sequences for event #36. Before the saturation (Figure 4.4 (a)&(b)), the technique does not modify any pixel. During the phase of greatest saturation (Figure 4.4 (c)&(d)), only saturated pixels and their surroundings are replaced with the interpolated values. Images taken when the saturation just finished (Figure 4.4 (e)&(f)), show minimal changes to the major characteristics of the flare ribbons. The saturation-correction method is applied on each frame throughout the flaring phase for every event under analysis, providing automatically corrected AIA observation sequences for the 51 events. This approach is an image-processing technique with no consideration as to the physical effect on the chromosphere, we nevertheless use this approach since Kazachenko et al. (2017) demonstrated that this technique can give a reasonable accumulated light curve.

Finally, with these saturation-removed image sequences, we make a cumulative mask to preserve all pixels that brightened above the intensity threshold between the *GOES* start time and end time. We demonstrate in Figure 4.5 the construction of the flare-ribbon masks: (a) identify the pixels exceeding the intensity threshold, and shift the mask to be co-aligned with the lower boundary magnetogram used in NLFFF according to solar differential rotation, (b) degrade the spatial resolution to match the magnetogram that serves as the lower boundary for the NLFFF extrapolation (see §2.3), (c) remove small gaps appearing in the mask, smooth the boundaries, and assign regions with unique labels (partitions) using the `closing` function of the `skimage` module in Python (van der Walt et al., 2014), and (d) after partitioning, small patches with area less than 60 pixels (about $1.8 \times 10^{18} \text{ cm}^2$) are removed for a “sanitized” flare-ribbon mask. We perform this sanitizing process because field lines rooted in low-signal magnetic regions (noise-dominated areas) will bring considerable uncertainty to the determination of overlying and wall fields. We superimpose the processed mask on the lower boundary B_z of the NLFFF model for analysis.

We assume that fieldlines from footpoints associated with post-reconnection heating still have a direct relation to field lines in a model computed prior to any reconnection, justifying the use of a pre-event NLFFF model in conjunction with the flare-ribbon mask to identify field lines of interest. In Figure 4.5 (e), the selected flare-ribbon field lines are presented, specifically only those field lines with both footpoints anchored co-spatially with flare ribbons.

We include only these field lines in the analysis in order to approximate the reconnect-imminent field, because we assume that an MFR which formed before event-related reconnection will have conjugate footpoints located in opposite polarities but in the vicinity of the flare ribbons. The

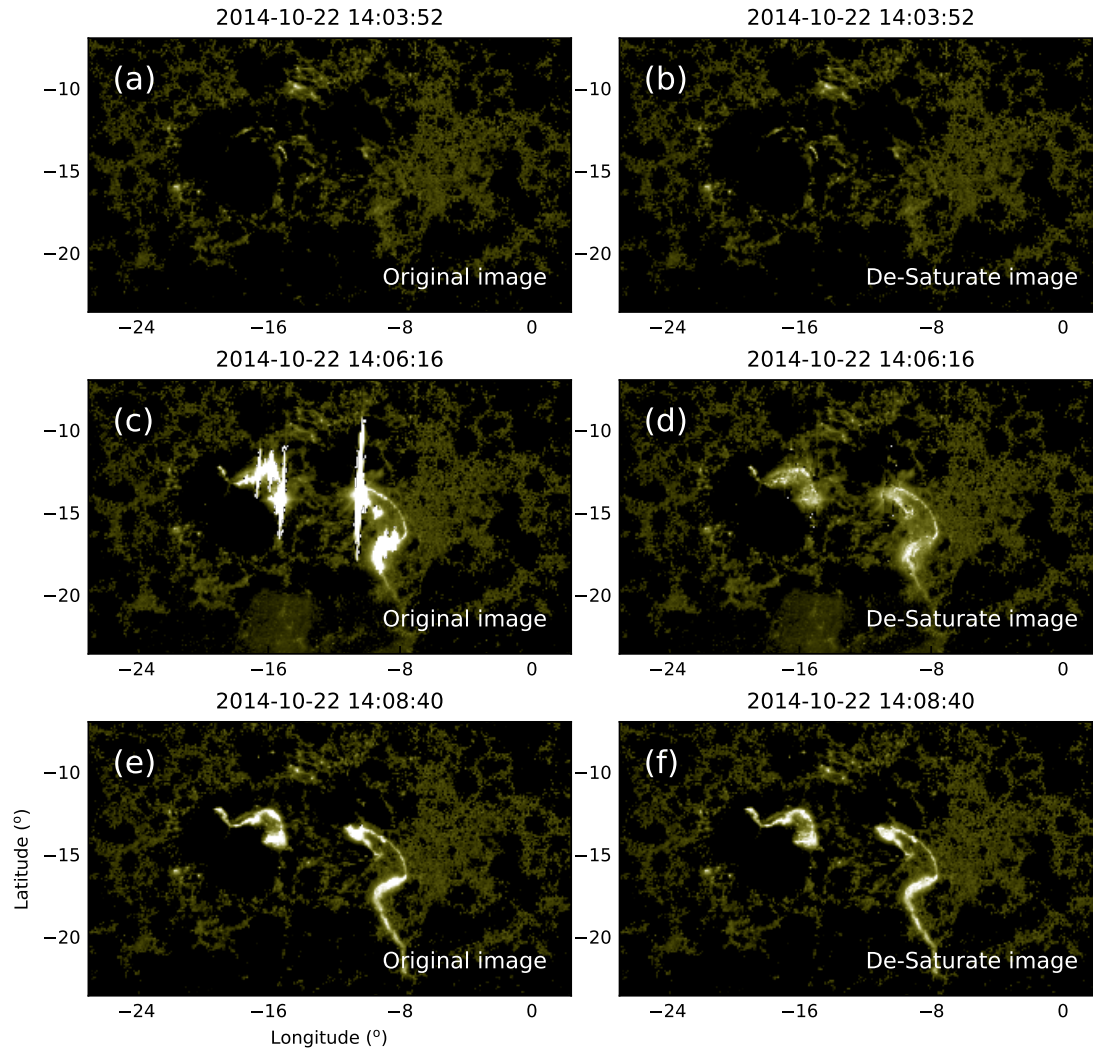


Figure 4.4: SDO/AIA 1600 Å images remapped into CEA projections shows the evolution of the flare ribbons on 22 October 2014 (event #36 in Table 4.1). Left column: original AIA image sequence. Right column: images after applying saturation-correction. (a)-(b) Snapshots of the flare ribbons at the initial phase, with no saturated pixels detected. (c)-(d) Snapshots of the flare ribbons when the largest number of saturated pixels are detected. (e)-(f) Snapshots of the flare ribbons during the gradual decay phase, again no saturated pixels are detected.

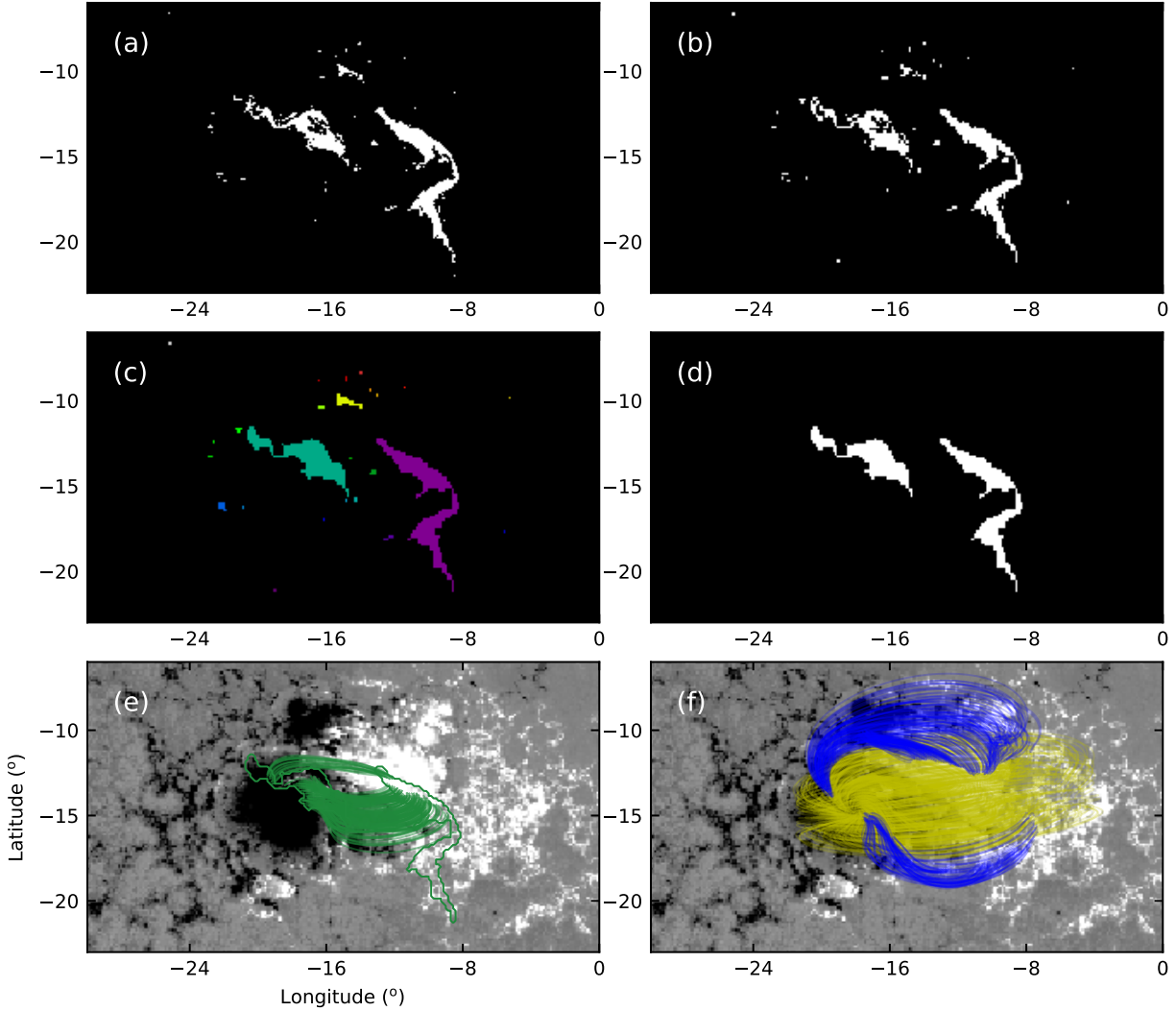


Figure 4.5: Deriving the Φ_{Ribbon} , $\Phi_{\text{Overlying,R}}$, and $\Phi_{\text{wall,R}}$, demonstrated on event #36. (a) Original flare-ribbon mask constructed from the de-saturated and re-mapped SDO/AIA 1600 Å observations. See text for details. (b) the flare-ribbon mask from (a) now degraded to the spatial resolution consistent with the lower boundary used in the NLFFF extrapolation; (c) the labeling result of the flare-ribbon mask; (d) sanitized flare-ribbon mask with only the main body of the flare ribbons retained; (e) field lines (green) which have both footpoints anchored in the proposed flare-ribbon mask (indicated by green contours); (f) field lines in the overlying field (yellow) and wall field (blue). All the maps are shown in the CEA projection.

corresponding overlying and wall field lines are consequently defined according to the description in §3.2.2 (see Figure 4.5 (f)). To summarize the definitions which will be applied in the q -scheme analysis:

- *Flare-ribbon-related field*: field lines with both field lines anchoring in the flare ribbons; closed field lines; no requirement on T_w .
- *Overlying field*: field lines lying above the flare-ribbon-related field; closed field lines; excludes flare-ribbon-related field; no requirement on T_w .
- *Wall field*: field lines with one foot point ≤ 10 Mm from the flare-ribbon-related field, the other footpoint $\gg 10$ Mm from any flare-ribbon-related field; closed field lines; excludes flare-ribbon-related field; no requirement on T_w .

Of note, although the highly-twisted field used in r -scheme also includes the information of flare ribbons, the major difference between these two schemes is that there is no restriction on T_w for the flare-ribbon-related field. Moreover, the footpoints of flare-ribbon-related fieldlines are coincident with the flare ribbons, whereas the highly-twisted fieldlines are roughly falling into the area at which ribbons appear. As both schemes involve the information of flare ribbons, there are some fieldlines selected by both r - and q -scheme to represent the MFR.

After determining the specific field lines targeted for analysis, the magnetic flux and magnetic twist flux are calculated with surface integration over the targeted footpoint pixels. The resulting q_m , q_τ , and q_κ are then inferred according to Equations (4.5), (4.6), and (4.7), respectively. The quantities used to derive q_m , q_τ , and q_κ are summarized in Table 4.4, and the associated uncertainties are quoted in the header as derived following the approaches described in Appendix B. Surprisingly, even though the identical technique is performed here, the error of each parameter is significantly smaller compared to what found for the r -scheme. We conclude that fluxes from the surface integral over the flare-ribbon area, are not sensitive to the observational uncertainties. Of note, in event #50, the value of flare-ribbon flux is zero as we failed to identify any field lines that have both footpoints anchored within the flare ribbons. The values of q parameters that have similar “null-set” issues are also assigned to zero.

The distributions of all the parameters in the q -scheme are presented in Figure 4.6 for the two populations, eruptive events and confined events. It appears that the eruptive events in general have greater values among all the q -scheme parameters. The mean values of the two populations indicate that the eruptive group always presents higher values than the confined group, across all q -scheme parameters. Even though q_κ now occupies a rather narrow parameter space, one can see

Event#	Φ_{Ribbon} $\pm 0.1\%$ (10^{20}Mx)	$\Phi_{\tau \text{ Ribbon}}$ $\pm 2.2\%$ (10^{20}Mx)	$\Phi_{\text{overlying, R}}$ $\pm 0.1\%$ (10^{20}Mx)	$\Phi_{\tau \text{ overlying, R}}$ $\pm 0.8\%$ (10^{20}Mx)	$\Phi_{\text{wall, R}}$ $\pm 0.1\%$ (10^{20}Mx)	$\Phi_{\tau \text{ wall, R}}$ $\pm 3.8\%$ (10^{20}Mx)	q_m^{a} $\pm 0.1\%$	$q_m^{\text{a+w b}}$ $\pm 0.1\%$	q_{τ}^{c} $\pm 1.4\%$	$q_{\tau}^{\text{c+w d}}$ $\pm 1\%$	q_{κ}^{e} $\pm 2.2\%$	$q_{\kappa}^{\text{e+w f}}$ $\pm 2.3\%$
1	8.30	3.14	20.38	8.48	44.67	3.50	0.29	0.11	0.27	0.21	0.11	0.04
2	45.64	14.94	40.63	8.96	16.78	0.92	0.53	0.44	0.63	0.60	0.17	0.15
3	14.79	4.02	60.79	8.63	19.82	3.88	0.20	0.16	0.32	0.24	0.05	0.04
4	16.94	3.75	8.51	0.71	16.16	2.04	0.67	0.41	0.84	0.58	0.15	0.09
5	23.64	5.46	18.14	4.60	37.33	3.91	0.57	0.30	0.54	0.39	0.13	0.07
6	27.44	8.14	17.92	2.65	33.82	2.66	0.60	0.35	0.75	0.61	0.18	0.10
7	4.60	1.63	2.59	0.90	9.76	0.98	0.64	0.27	0.65	0.46	0.23	0.10
8	18.12	7.04	7.30	0.46	16.87	0.55	0.71	0.43	0.94	0.87	0.28	0.17
9	15.98	6.19	14.44	1.30	16.80	0.52	0.53	0.34	0.83	0.77	0.20	0.13
10	1.79	0.14	18.28	0.56	25.88	1.34	0.09	0.04	0.20	0.07	0.01	0
11	131.81	33.50	84.21	10.83	37.03	7.79	0.61	0.52	0.76	0.64	0.16	0.13
12	47.88	13.08	71.75	13.60	77.19	7.88	0.40	0.24	0.49	0.38	0.11	0.07
13	46.71	14.13	53.56	8.40	51.56	5.16	0.47	0.31	0.63	0.51	0.14	0.09
14	46.12	12.12	57.88	4.77	37.70	3.77	0.44	0.33	0.72	0.59	0.12	0.09
15	16.13	4.65	43.27	5.16	34.19	3.31	0.27	0.17	0.47	0.35	0.08	0.05
16	3.41	0.88	8.53	1.19	8.35	0.54	0.29	0.17	0.43	0.34	0.07	0.04
17	13.80	2.56	35.33	6.86	70.29	8.85	0.28	0.12	0.27	0.14	0.05	0.02
18	8.14	2.06	38.34	8.15	79.55	7.53	0.18	0.06	0.20	0.12	0.04	0.02
19	5.26	0.46	36.10	2.11	56.69	14.85	0.13	0.05	0.18	0.03	0.01	0
20	11.22	1.86	8.84	0.38	6.39	0.43	0.56	0.42	0.83	0.70	0.09	0.07
21	4.35	1.12	9.66	2.66	7.14	0.83	0.31	0.21	0.30	0.24	0.08	0.05
22	4.04	1.62	14.10	2.28	16.17	1.34	0.22	0.12	0.42	0.31	0.09	0.05
23	4.66	1.60	16.72	1.35	11.81	0.63	0.22	0.14	0.54	0.45	0.07	0.05
24	27.66	5.14	28.37	3.18	63.51	3.72	0.49	0.23	0.62	0.43	0.09	0.04
25	11.52	4.37	27.66	4.07	22.11	1.36	0.29	0.19	0.52	0.45	0.11	0.07
26	10.75	5.09	27.46	2.55	23.57	3.11	0.28	0.17	0.67	0.47	0.13	0.08
27	47.26	11.07	23.77	1.71	42.26	3.46	0.67	0.42	0.87	0.68	0.16	0.10
28	23.86	5.74	103.20	10.76	40.52	6.22	0.19	0.14	0.35	0.25	0.05	0.03
29	8.68	0.52	16.30	1.15	4.75	0.47	0.35	0.29	0.31	0.24	0.02	0.02
30	17.40	4.62	79.06	16.06	53.15	6.12	0.18	0.12	0.22	0.17	0.05	0.03
31	17.88	5.27	7.01	0.48	1.99	0.02	0.72	0.67	0.92	0.91	0.21	0.20
32	28.01	2.95	13.21	0.48	15.64	1.70	0.68	0.49	0.86	0.57	0.07	0.05
33	29.71	6.07	30.93	2.28	16.92	2.57	0.49	0.38	0.73	0.56	0.10	0.08
34	14.01	3.35	43.32	5.08	75.17	5.04	0.24	0.11	0.40	0.25	0.06	0.03
35	35.59	10.71	178.15	37.27	71.60	13.86	0.17	0.12	0.22	0.17	0.05	0.04
36	44.71	9.58	176.49	36.43	69.59	9.73	0.20	0.15	0.21	0.17	0.04	0.03
37	72.95	14.83	217.94	45.29	72.11	8.95	0.25	0.20	0.25	0.21	0.05	0.04
38	26.00	8.12	116.91	22.65	122.12	16.99	0.18	0.10	0.26	0.17	0.06	0.03
39	33.38	7.90	140.76	24.69	128.72	10.51	0.19	0.11	0.24	0.18	0.05	0.03
40	42.55	7.64	170.47	27.69	81.90	7.99	0.20	0.14	0.22	0.18	0.04	0.03
41	59.80	16.07	57.91	5.47	36.95	1.79	0.51	0.39	0.75	0.69	0.14	0.10
42	48.34	5.43	34.81	2.58	14.42	1.02	0.58	0.50	0.68	0.60	0.07	0.06
43	0.43	0.03	15.04	4.26	37.99	7.70	0.03	0.01	0.01	0	0	0
44	29.13	11.70	29.56	4.75	39.20	4.46	0.50	0.30	0.71	0.56	0.20	0.12
45	54.51	16.15	107.57	14.93	50.70	5.32	0.34	0.26	0.52	0.44	0.10	0.08
46	7.95	2.08	1.16	0.15	11.31	0.58	0.87	0.39	0.93	0.74	0.23	0.10
47	20.60	7.38	15.46	5.84	33.08	4.38	0.57	0.30	0.56	0.42	0.20	0.11
48	59.35	22.26	72.64	13.97	33.23	2.46	0.45	0.36	0.61	0.58	0.17	0.13
49	76.99	18.10	72.55	7.43	15.48	0.95	0.51	0.47	0.71	0.68	0.12	0.11
50	0	0	5.60	0.34	4.72	0.69	0	0	0	0	0	0
51	8.41	2.06	29.09	4.19	47.92	4.75	0.22	0.10	0.33	0.19	0.05	0.02

^a $r_{m, \text{Ribbon}}$ calculated based on hypothesis 1 ($\Phi_{\text{surrounding}} = \Phi_{\text{overlying}}$).

^b $r_{m, \text{Ribbon}}$ calculated based on hypothesis 2 ($\Phi_{\text{surrounding}} = \Phi_{\text{overlying}} + \Phi_{\text{wall}}$).

^c $r_{\tau, \text{Ribbon}}$ calculated based on hypothesis 1 ($\Phi_{\tau \text{ surrounding}} = \Phi_{\tau \text{ overlying}}$).

^d $r_{\tau, \text{Ribbon}}$ calculated based on hypothesis 2 ($\Phi_{\tau \text{ surrounding}} = \Phi_{\tau \text{ overlying}} + \Phi_{\tau \text{ wall}}$).

^e $r'_{\tau, \text{Ribbon}}$ calculated based on hypothesis 1 ($\Phi_{\text{surrounding}} = \Phi_{\text{overlying}}$).

^f $r'_{\tau, \text{Ribbon}}$ calculated based on hypothesis 2 ($\Phi_{\text{surrounding}} = \Phi_{\text{overlying}} + \Phi_{\text{wall}}$).

Table 4.4: Estimations related to q_m , q_{τ} and q_{κ}

that the two distributions still peak at distinct values, with the eruptive population exceeding the confined, on average. The results imply a tendency that across each variation in algorithm, the suppression term tends to be weaker for the eruptive events. The distributions also reveal that the values for q_κ (which contains q_κ^o and q_κ^{o+w}) are generally smaller than other parameters, due to the numerator (Φ_τ) being generally smaller than the denominator (Φ). The values of the target events for each q -parameter are indicated in Figure 4.6. We find that compared to their values in r -scheme parameters (Figure 4.2), the target events' q -scheme values have decreased overall, and are now correctly classified as “confined” by most of the q -based parameters (see Table 4.6).

The statistical metrics for evaluating the distinguishing power of each parameter are summarized in Table 4.5. Within the bootstrap uncertainties, there is no significant difference between the r - and q -schemes for MFR description, thus we cannot state which scheme is superior. All resulting DA metrics are also presented in Figure 4.3. The most significant difference between the two schemes is that the uncertainties of the q -scheme parameters as estimated by a Monte Carlo analysis are fairly small (see also Figure 4.3). For some metrics (*e.g.*, all those corresponding to q_m^{o+w}), the uncertainties are zero, owing to the fact that this estimate is basically inherited from the uncertainty listed in Table 4.4. In contrast, the bootstrap method provides larger uncertainties that reflect the small sample size; this can be regarded as the upper bound of uncertainty in the evaluation metrics for the q -scheme.

In contrast to the r -scheme, the discrimination ability is not improved by the q -scheme when the wall field is included. We speculate that the intensity threshold for flare-ribbon regions should be considered an additional source of uncertainty. In Appendix C, we tested how the values of Φ_{Ribbon} , $\Phi_{\text{overlying,R}}$, and $\Phi_{\text{wall,R}}$ vary with adjusting the intensity threshold, finding that the magnetic flux varies substantially for some events, and shows no significant change for others. This implies an additional uncertainty with regards to the definition of flare ribbons. Despite these considerable uncertainties, these metrics provide a hint of how the propensity to erupt varies across different approximations of an MFR's location and boundaries.

Next we discuss how the parameter values for events #35, #36, and #37 change across the distinct schemes. The values of all parameters for these target events are shown in Figures 4.2 and 4.6, and we find that the values of their r -scheme parameters decrease in the related q -scheme parameters. This can be confirmed through comparing the targets' values relative to the means of the distributions: the values are all close to the average in r -scheme, whereas for the q -scheme, the values are smaller than the average.

To confirm the impact of using the flare-ribbon flux for the three targeted events, we summarize the ability of the two schemes to correctly classify them in Table 4.6, including $n - 1$ cross validation.

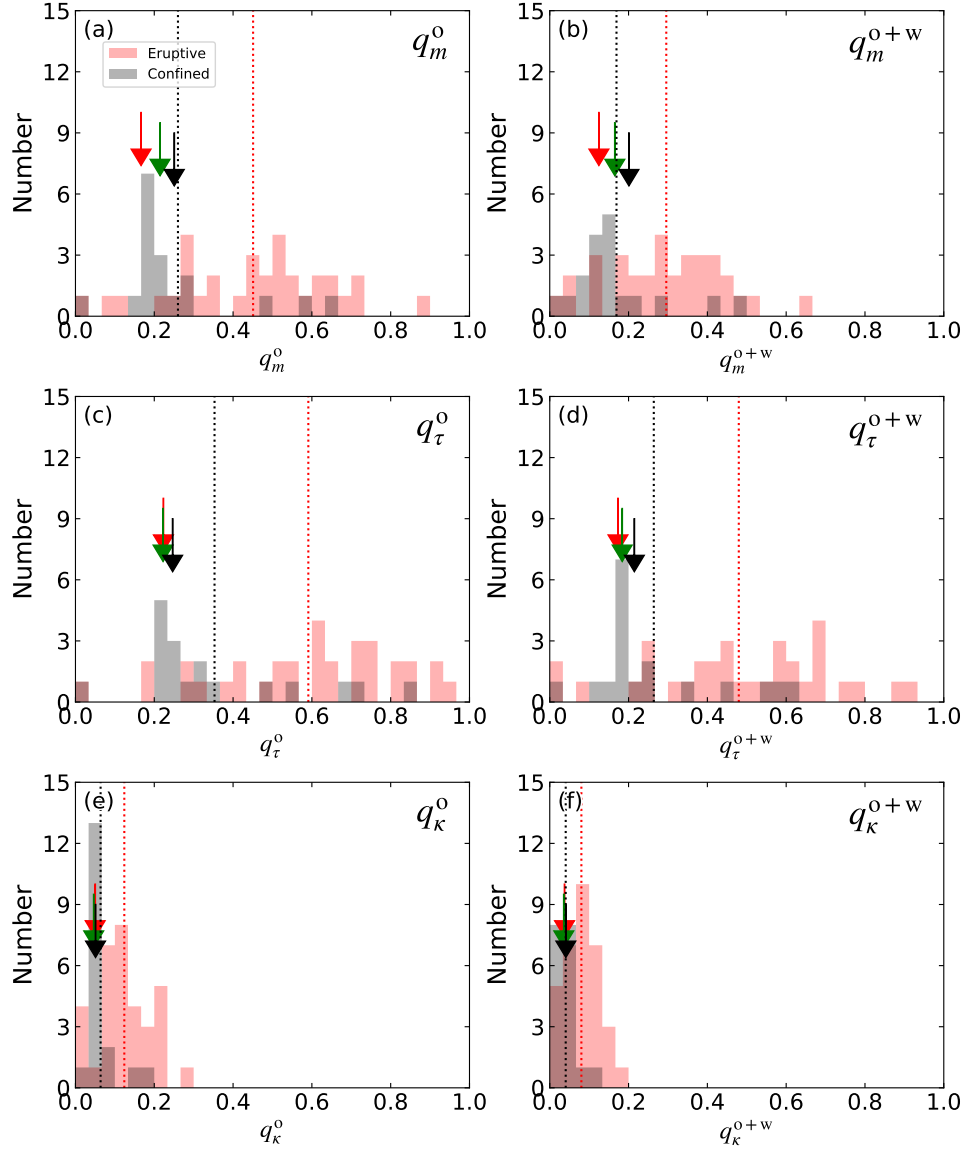


Figure 4.6: Histograms of (a) q_m^o , (b) q_m^{o+w} , (c) q_τ^o , (d) q_τ^{o+w} , (e) q_κ^o , and (f) q_κ^{o+w} for eruptive events (red) and confined events (black). Red (black) vertical dash lines indicate the mean value of the variables for eruptive (confined) events. The arrows colored in red, green, and black indicate the values for events #35, #36, #37, respectively.

Parameter	Mehod	Statistical Metrics			
		Probability (%)	MD ^a	CR ^b	TSS
q_m^o	Original	98.2	1.03	0.80	0.55
	Monte Carlo	98.2±0.0%	1.03±0.00	0.78±0.00	0.52±0.00
	Boot Strap	93.3±9.4%	1.05±0.66	0.72±0.08	0.29±0.29
q_m^{o+w}	Original	96.1	0.78	0.69	0.26
	Monte Carlo	96.1±0.0%	0.78±0.00	0.67±0.00	0.21±0.00
	Boot Strap	88.7±15.0%	0.81±0.56	0.69±0.08	0.19±0.26
q_τ^o	Original	98.2	1.04	0.76	0.48
	Monte Carlo	98.1±0.5%	1.02±0.07	0.74±0.02	0.40±0.06
	Boot Strap	94.0±8.3%	1.08±0.68	0.73±0.07	0.32±0.26
q_τ^{o+w}	Original	98.1	1.00	0.78	0.49
	Monte Carlo	98.1±0.2%	1.01±0.04	0.74±0.01	0.42±0.02
	Boot Strap	93.8±8.0%	1.01±0.59	0.72±0.08	0.28±0.27
q_κ^o	Original	97.9	0.97	0.80	0.55
	Monte Carlo	98.2±0.0%	1.03±0.01	0.78±0.00	0.52±0.00
	Boot Strap	93.9±7.6%	0.93±0.52	0.71±0.10	0.25±0.32
q_κ^{o+w}	Original	97.5	0.92	0.73	0.35
	Monte Carlo	96.2±0.1%	0.78±0.00	0.67±0.00	0.21±0.00
	Boot Strap	93.7±7.0%	0.88±0.47	0.69±0.08	0.20±0.26

^a Mahalanobis distance for the sample PDFs.

^b Correct rate of the classification table.

Table 4.5: DA results (with $n - 1$ Cross-validation)

We find that the q -scheme classifications, where the inferred sites of magnetic reconnection (flare ribbons) define the MFR, are in better agreement with the confined nature of these three events, particularly for q_τ^o , q_τ^{o+w} , and q_κ^o . None of r -scheme parameters provide a correct classification for these three events, hence we conclude that highly twisted flux ($|T_w| > 0.2$) provides an insufficient condition to identify the reconnected field lines.

Event#	r -scheme						q -scheme					
	r_m^o	r_m^{o+w}	r_τ^o	r_τ^{o+w}	r_κ^o	r_κ^{o+w}	q_m^o	q_m^{o+w}	q_τ^o	q_τ^{o+w}	q_κ^o	q_κ^{o+w}
35	×	×	×	×	×	×	○	×	○	○	○	×
36	×	×	×	×	×	×	○	×	○	○	○	×
37	×	×	×	×	×	×	×	×	○	○	○	×

○: correct classification; ×: mis-classification.

Table 4.6: Comparison of DA results across different schemes

4.3 Discussion

4.3.1 Critical height analysis

The Torus Instability (TI; Démoulin & Aulanier, 2010, Kliem & Török, 2006) is an MHD instability described by force balance in the context of a coronal loop placed in an external magnetic field whose strength decreases with height. TI has been invoked in many studies to explain the eruptive properties of certain solar flares (e.g. Baumgartner et al., 2018, Duan et al., 2019, Fan & Gibson, 2007, Guo et al., 2010, Jing et al., 2015, Liu, 2008, Nindos et al., 2012, Wang et al., 2017). In this part, we investigate why the q -scheme can better classify the (non)-eruptive nature of the three target events than can the r -scheme, from the viewpoint of this MHD instability.

The decay index n quantifies the fall-off with height of the strapping force available to constrain an underlying MFR:

$$n = -\frac{\partial \log B_h}{\partial \log z}, \quad (4.8)$$

where B_h is the horizontal component of the external magnetic field, and z represents the distance above the photosphere in the direction opposite gravity.

A critical height is defined as that where the corresponding n exceeds a critical value n_c , and the strapping force can no longer constrain an MFR; the subsequent eruption will give rise to a CME. Analytic modeling indicates that n_c is typically between [1.1–2.0] (Bateman & Grimm, 1979, Kliem & Török, 2006), and $n_c = 1.5$ is widely used (e.g. Chen et al., 2015, Chintzoglou et al., 2017, Jing et al., 2018). Since the major difference between the q -scheme and the r -scheme is the distinct way of determining the MFR-relevant field lines (those in the flare-ribbon regions *v.s.* those with

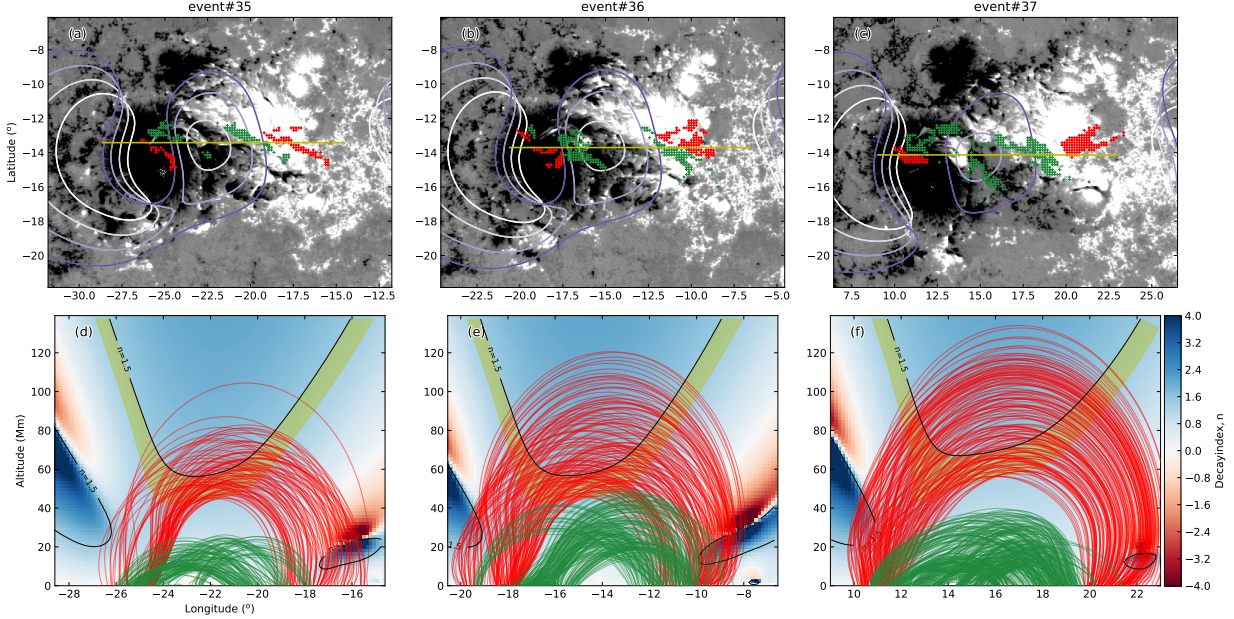


Figure 4.7: (a)-(c) Contour plot of decay index with height, overlaid on photospheric CEA B_r magnetograms saturated at ± 500 Gauss. Marks correspond to the footpoints of the ribbon-associated magnetic fieldlines (green) and the footpoints of the highly twisted ($|T_w| \geq 0.2$) fieldlines that have achieved the critical height (red), as indicated in panel (d)-(f). Areas within purple-white colored isocontours correspond to the area with $n = 1.5$ at the heights of 50, 60, 70, and 80 Mm. (d)-(f): Vertical slices cut at the yellow lines in (a)-(c) show the distribution with height of n for each event, and the black contours indicate the critical height. Note that (d)-(f) only cover the extent of the yellow lines shown in (a)-(c). The translucent yellow area along with the black contours denotes the altitude corresponds to a critical value range $n = [1.3 - 1.5]$. The curves represent (red:) all the projected field lines anchored in highly twisted region ($|T_w| \geq 0.2$) that achieves the critical height ($n = [1.3 - 1.5]$, as the yellow area shown) and (green:) the projected field lines anchored in the flare ribbons.

large T_w), the height that an inferred MFR can achieve could differ under these definitions. In this section, we compare the critical height derived for Events #35, #36, and #37 in the context of the two schemes and TI stability.

The TI analysis of the target events is outlined in Figure 4.7. For each event, n is calculated over the entire computational domain described in §2.3.1. Of note, we use the potential field that initiates the NLFFF to estimate B_h , and that model is provided roughly 1 hour before the *GOES*

flare start time. We use the potential field to calculate n because we regard the potential field to better approximate the magnetic field around the MFR compared to the NLFFF reconstructed magnetic field. We have also calculated n with the NLFFF reconstructed data, finding that there is no significant difference between two resulting n distributions. By comparing the volume where the decay index is greater than a critical threshold (here $n > 1.5$) with the relevant extrapolated field lines, we can identify where the horizontal field is too weak to trap the MFR. We find “tunnel” structures defined by $n > 1.5$ that indicate paths where MFRs could possibly escape away. In Figure 4.7 (a)-(c), recalling that the target events are homologous flares as defined by the integrated flare ribbon areas, the configurations of the TI-unstable tunnels across the events are very similar. There are three TI-unstable tunnels in AR 12192, two tunnels locate in its periphery and one located near the central, major PIL.

To confirm the TI condition, the body of the MFR must lie underneath the height at which the decay index becomes critical, hence we also examine the vertical distribution of n . Figure 4.7 (d)-(f) shows a cut of the vertical distribution of n in the context of the reconnection-imminent fieldlines as selected by the r and q schemes. Not surprisingly, the vertical distribution of n is similar across all three events, as are the field-line distributions. Those fieldlines identified with the MFR and as reconnection-imminent according to the r -scheme by their $|T_w| \geq 0.2$ structure, extend to a higher altitude and insert into the TI-unstable tunnel. The r -scheme classifies these events as eruptive, consistent with what would be expected in the context of the torus instability, but incorrect. Those fieldlines associated with the eventual flare ribbons, as defined by the q -scheme, do not reach as high in altitude, and do not cross the $n \geq 1.5$ boundary or insert into the TI-unstable tunnel. The q -scheme’s correct classification of “confined” is understood now in terms of this MHD instability as well.

We briefly examine whether, besides for NOAA AR 12192, “highly-twisted fieldlines cannot represent a flux rope” is a general feature among other events that are mis-classified by the r_m scheme. We surveyed the geometry of fieldlines in terms of the torus instability, following the analysis above, across 14 r_m -exceptional events, finding that:

- among 6 eruptive events, none has highly twisted field lines that exceed the $n > 1.5$ instability criterion, and
- among 8 confined events, four have highly twisted field lines that exceed the $n > 1.5$ instability criterion (3 of those four being the target events discussed above).

As a result, we suggest that representing an MFR by the $|T_w| \geq 0.2$ threshold may have also caused mis-classification in other events originating from active regions besides AR 12192.

With the critical height study presented here, we find that the deduced eruptive potential is strongly dependent on the definition of the MFR. We see why the q -scheme performs better for the three target events, in that the real reconnected flux might be closer to the magnetic flux spatially associated with the flare ribbons. We find a substantial height difference between the field lines with $|T_w| \geq 0.2$ and those field lines associated with the flare ribbons. This difference implies that using the r -scheme to identify the eruption-imminent MFR could include field lines that are not responsible for the flare-triggering reconnection.

4.3.2 Differences between the “highly-twisted” regions and the “flare ribbon” Regions

From the comparison of the r - and q -scheme based on the TI analysis, we surmise that appropriately determining the MFR could be crucial for classifying an event’s eruptivity. We conclude that for some ARs/events, the MFR can be more appropriately approximated by the q -scheme (flare-ribbon field lines). Here we address a question: what makes T_w an insufficient condition for appropriately representing the MFR for some ARs/events?

The T_w is calculated using linear integration of α along the full field line from the NLFFF model. Some fieldlines will meet the threshold of $|T_w| \geq 0.2$, with fairly low non-potentiality (a small force-free constant α) but relatively long field-line length. As a result, even though T_w may serve as a good indication of the presence of an MFR, imposing the $|T_w| \geq 0.2$ threshold may fail to indicate the “volume” of the MFR, particularly in the target events.

To verify this hypothesis, in Figure 4.8, we examine the spatial distributions of T_w , field-line length (L), and α at the photosphere (the value for the corresponding fieldline). These maps are deduced from the NLFFF model 1 hour before the event. Across the maps for events #35, #36, and #37, the red contours mark the highly twisted region that has been determined in §3, the footpoints of field lines anchoring in the flare ribbons are indicated by green contours, and the two contours are co-aligned according to solar differential rotation. In the T_w maps (Figure 4.8 (a)-(c)), one can see that despite the flare ribbons being identified through a purely photometric method, they resemble the highly twisted regions in some parts: the flare ribbons and the twist number provide some consistent information regarding the location of the MFR, although the flare ribbons can only be mapped after the flare.

From the L maps (Figure 4.8 (d)-(f)) compared to the flare-ribbon area, the “highly twisted regions” seem to stretch away from the PIL, corresponding to footpoints where the $T_w < -0.2$ is due primarily to the longer L . However, compared to L , it is difficult to distinguish any difference

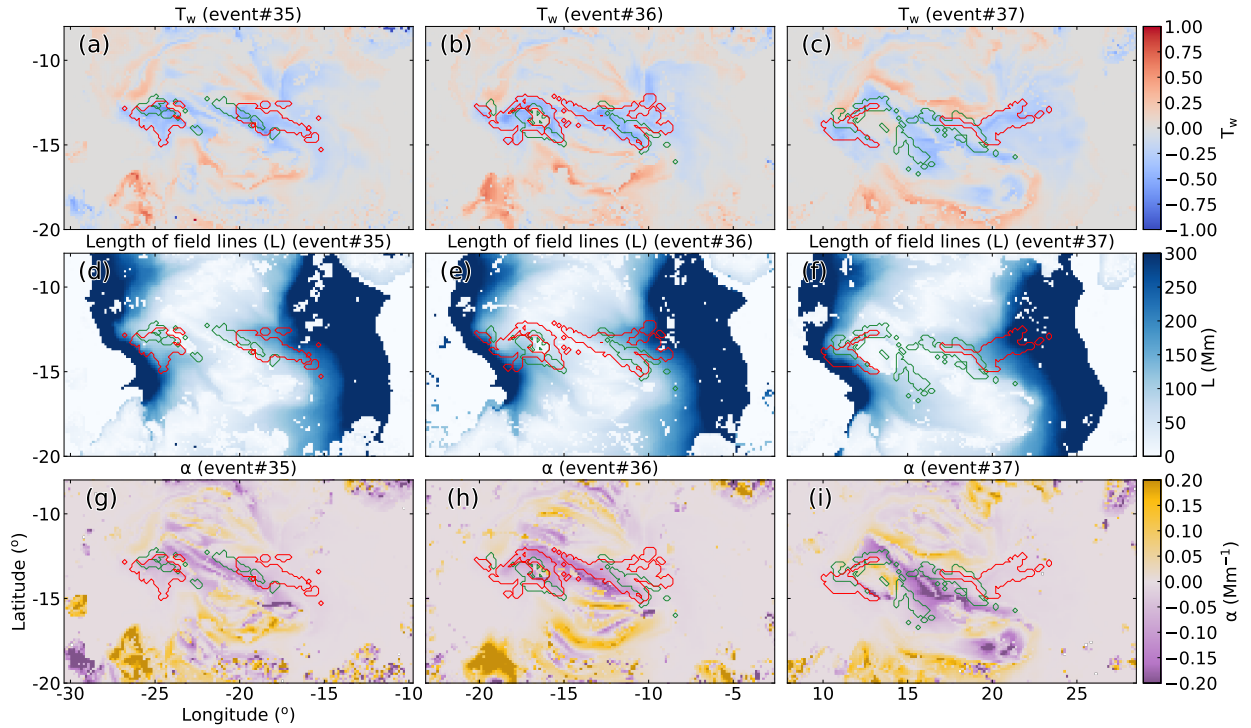


Figure 4.8: (a)-(c) Map of integrated twist T_w , (d)-(f) lengths of field lines (L), and (g)-(i) force-free constant (α) inferred from the NLFFF-extrapolated magnetic field model for event #35, #36, and #37. Red contours enclose the area with $|T_w| > 0.2$ that is used in calculating r parameters, green contours enclose the footpoint area for fieldlines that have both footpoints anchored co-spatially with the flare ribbons.

in the α distribution (Figure 4.8 (g)-(i)) between the flare ribbon area (green contours) and the highly-twisted regions (red contours).

For a quantitative comparison, Figure 4.9 shows, for the three events, the distributions of L and α for the MFR-defining fieldlines identified by the r - and q -schemes. The temporal evolution of flare ribbon is also indicated, as is the T_w threshold used in this study and in §3. It is shown in Figure 4.9 that although the flare-ribbon field lines have predominantly $|T_w| \geq 0.2$, there are still some with $|T_w| < 0.2$. This implies that the reconnected field lines are not always highly twisted as per our definition here.

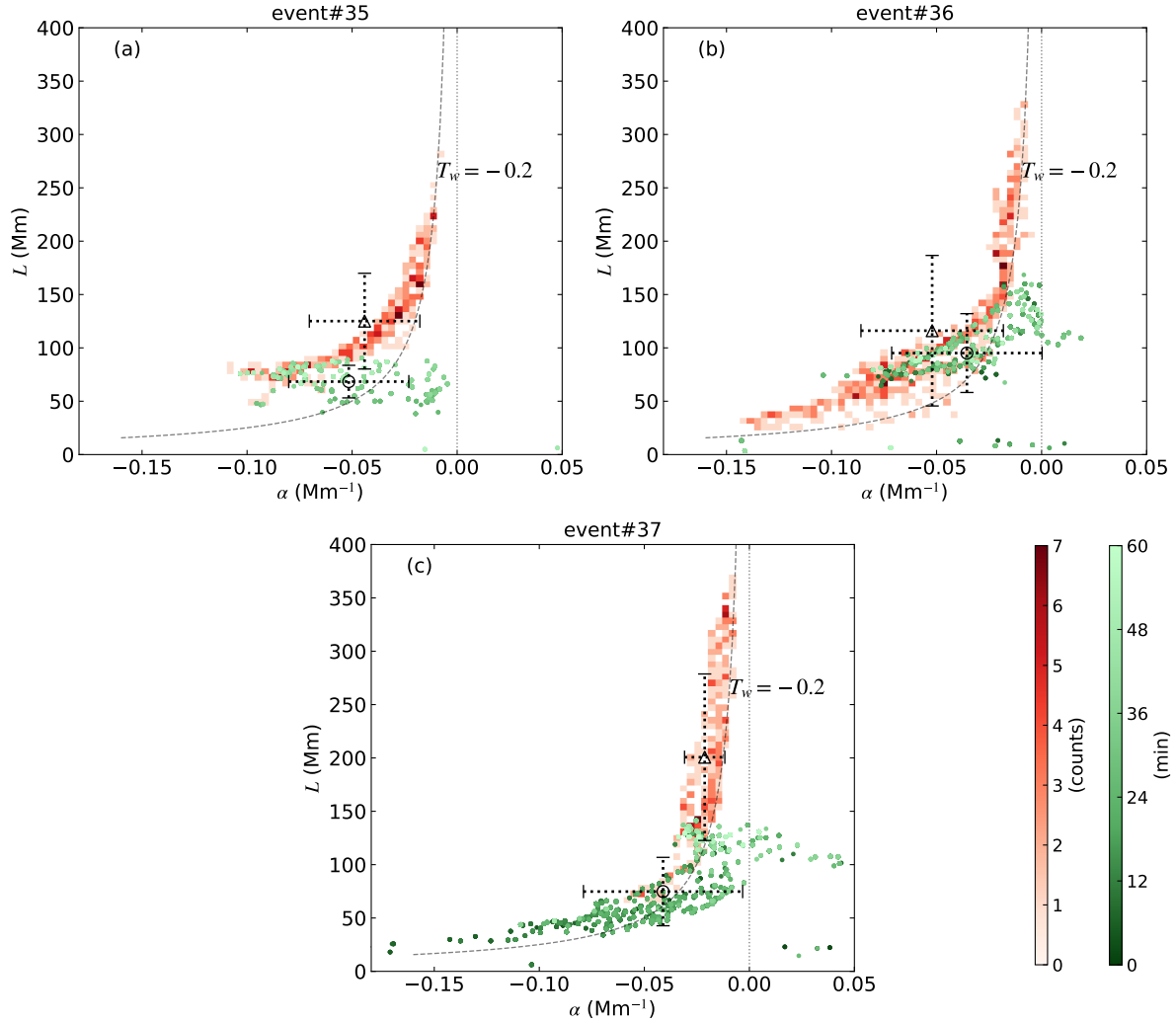


Figure 4.9: Diagram of α versus L for (a) event #35, (b) event #36, and (c) event #37. The dots (colored in green-white gradient) indicate the locus for the flare-ribbon field lines (as identified for the q -scheme analysis) as a function of time (minutes after flare onset) when that field-line footpoint’s pixel first brightens in the AIA 1600 Å images. The underlying 2-D histograms (red gradation) present the number density of the $\alpha - L$ distribution of field lines with $T_w < -0.2$ used in the r -scheme analysis. The average α and L for the $|T_w| > 0.2$ and flare-ribbon groups are indicated by the triangle and circle, respectively. The error bars indicate a $\pm\sigma$ spread. The dashed curve marks the $T_w = -0.2$ boundary.

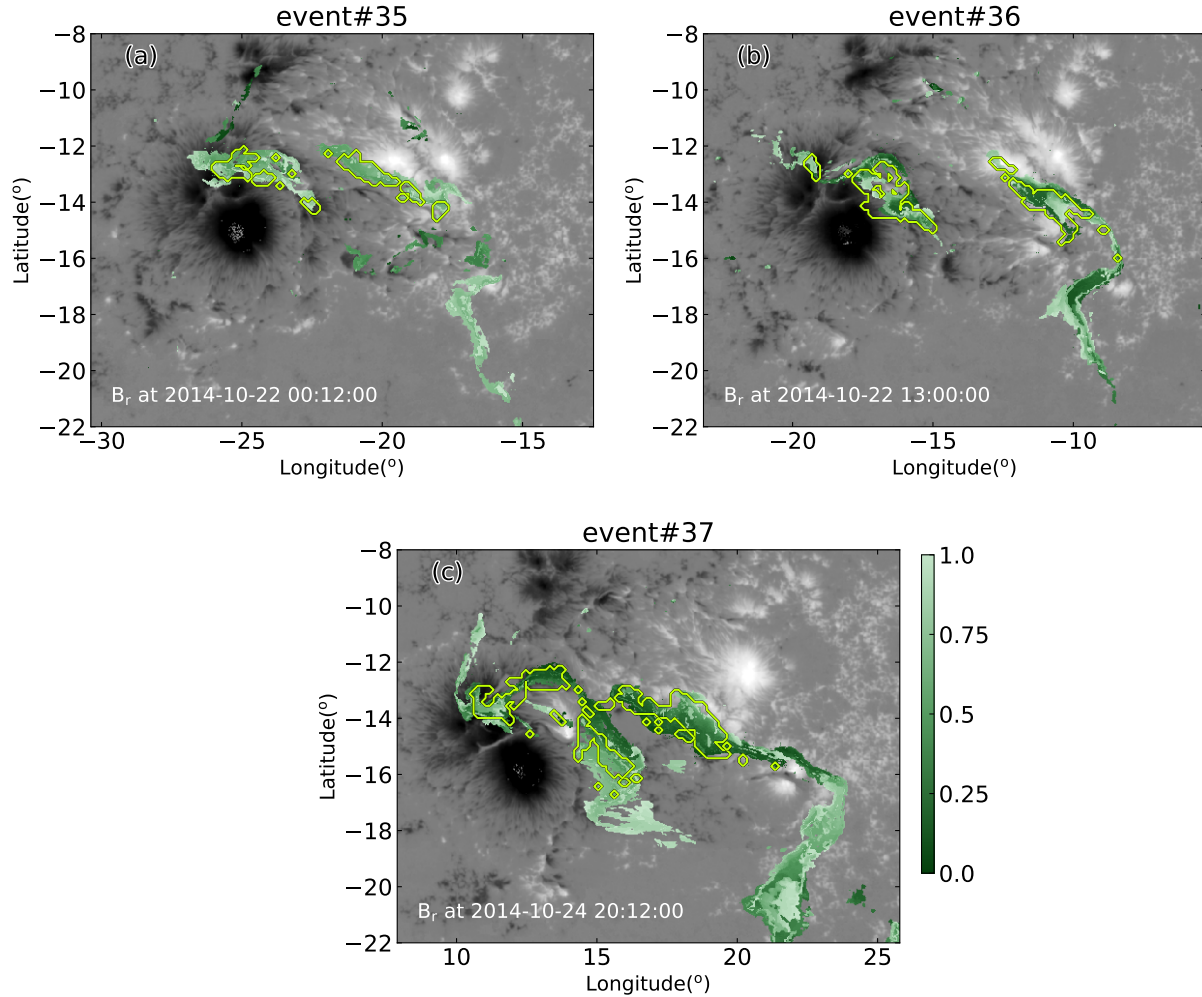


Figure 4.10: Temporal evolution of flare ribbons overlaid on the SHARP B_r magnetogram (from ≈ 1 hr before the flare onset, and saturated at $\pm 2500G$) for (a) event #35, (b) event #36, and (c) event #37. The color is assigned according to when the flare-ribbon pixel first appears in AIA 1600 Å images from the *GOES* start time up to the *GOES* peak time listed in Table 4.1, which is normalized to between [0, 1]. The light-green contours highlight the pixels included in calculating the q -based parameters.

The average L is larger for field lines in the $|T_w| > 0.2$ and shorter than 150 Mm in length for the flare-ribbon associated field lines. This implies that the flare-related reconnection mainly occurs

on shorter field lines. The values of average α , on the other hand, show no significant difference between the two groups compared to the difference for the average L . This suggests that even the field lines with small nonpotentiality could be involved in the reconnection process.

The temporal evolution of the flare ribbons presented in Figure 4.9 shows no consistent trend across the three events. For some details on the inconsistency of the ribbon progressions, a spatial depiction of the flare-ribbon evolution as seen in AIA 1600Å images is presented in Figure 4.10. We relate the progression shown in the α - L diagram (Figure 4.9) to the spatial progression (Figure 4.10) thus:

- *Event #35*: the initial brightening appears near longitude/latitude -25,-10.
- *Event #36*: the initial brightening appears at multiple locations; hence, there is no obvious temporal trend in the α - L diagram.
- *Event #37*: the ribbon patterns start near the PIL, gradually spreading away from it. The flare-related fieldlines gradually progress from high α to low α locations (as shown in Figure 4.8 (i)). This profile is consistent with the α - L diagram.

The results presented here suggest that the differing temporal evolution is due to the initial reconnection being activated at different locations. However, the coronal loops associated with the progressive reconnections share similar geometrical and topological features. As a result, the resulting flare ribbons are similar to each other in the integrated properties because the observed ribbons are connecting to these coronal loop structures at the corresponding footprints, even if they differ in some details.

With the distributions of α and L (Figure 4.9), we can compare the two schemes:

- *Detecting / Defining the MFR*: fieldlines with $|T_w| \geq 0.2$ and lying near the PIL involved in the flare and near the flare ribbons in the r -scheme; flare-ribbon-related fieldlines in the q -scheme.
- α in the MFR: no significant difference between the two schemes.
- L in the MFR: no strong tendency across these three MFRs as defined by r -scheme, while these MFRs as defined by q -scheme are dominated by fieldlines with $L < 150$ Mm.

Since the q -scheme better represents the MFRs in these target events, we conclude that it is almost impossible to identify an MFR only based on nonpotentiality measures, for instance, α or T_w . We

conclude that field-line length could be a good MFR identifier, as demonstrated for these three events. In summary, to estimate the *total* amount of reconnection contributed by an MFR, the geometrical information of fieldlines that compose the MFR is required in some events.

4.4 Summary and conclusions

The eruptive (or confined) nature of three solar flares originating from AR12192, identified as events #35, #36, and #37 in §3, failed to be correctly classified in that study by the original parameter r_m used to evaluate the magnetic flux rope force balance in the context of its surrounding field. Here, we perform a systematic study on these three events to understand factors which contributed to that failure. First, we propose that other physical quantities could better represent the force balance acting on the MFR. To test this hypothesis, we modified the r_m algorithm to incorporate instead the magnetic twist flux (Φ_τ), proposing two new parameters: r_τ and r_κ , which instead use the ratio of magnetic twist flux and the ratio of magnetic twist flux over magnetic flux, respectively. Second, we further proposed that the area defined by field lines showing greater than 0.2 winds ($|T_w| \geq 0.2$) may insufficiently represent the MFR.

Taking a different tact, we then suggest that using information on the flare ribbon location and evolution may provide a more direct approximation of the reconnected magnetic flux, that is, would better identify those field lines that comprise the MFR. Mirroring the r -scheme and its parameters r_m , r_τ , and r_κ , we propose the q -scheme based on the flare-ribbon associated magnetic field, and parameters q_m , q_τ , and q_κ . In the q -scheme, the highly twisted field lines used in the r -scheme are replaced by field lines whose footpoints are cospatial with flare ribbons as identified using AIA 1600Å image sequences.

Linear discriminant analysis was used to classify all 51 of the events for all parameters from both r - and q -schemes. Quantitative metrics are then used to evaluate the parameters' classification success. The resulting DA metrics demonstrate that both schemes have a “moderate” classification ability overall, with large uncertainties due primarily to small sample size. For the three target events, none of the parameters in r -scheme, including the new ones, provide correct classification outcomes. Conversely, as summarized in Table 4.6 three of the six q -scheme correctly classify the three target events' eruptivities.

To investigate this performance difference for the three target events, we invoke an analysis based on the torus instability, comparing the height where the decay index reaches critical levels to the height reached by the relevant magnetic field lines in the two schemes. We find that the expected

eruptivity as diagnosed by TI is surprisingly consistent with the results as inferred by the q -scheme (correctly expecting confined events) and the r -scheme (incorrectly expecting eruptive events). The exercise of comparing the expected eruptivities from two entirely distinct methods emphasizes the importance of correctly separating the volume of an MFR from the ambient magnetic field.

The analysis so far demonstrates that any MFRs existing in the target events are improperly represented by the field having more than 0.2 turns. To search for field lines with twist number exceeding 0.2 turns but that contain inadequate nonpotentiality, our α - L diagram (Figure 4.9) shows the distributions of the force-free parameter α and NLFFF-model field-line length L for the two distinct groups of field lines. Counterintuitively, we find no obvious difference between the two schemes' field lines in terms of the distribution of α , implying almost equal nonpotentiality among them across the target events. However, all of the flare-ribbon-associated field lines are shorter than 150 Mm in length, while the r -scheme defined fieldlines appear with a wide range of lengths $25 \gtrsim L \gtrsim 380$ Mm. This finding leads us to conclude that the event-triggering reconnections for these events are restricted to shorter, although not necessarily highly non-potential, fieldlines.

The temporal behaviors of the flare ribbons shown in α - L diagrams suggest that there is no consistent tendency in the temporal evolution of these three flares. We examine the flare-ribbon behaviors in detail through time-sequences of SDO/AIA 1600 Å filtergrams, presenting the flares' progressions in Figure 4.10. We find that the target events' onset reconnections begin at different locations but associated with similar coronal magnetic field systems. These differences in ribbon evolution are notable in that otherwise, the three flares appear homologous.

In summary, we contend that for these three events, the factor behind their incorrect classification in the r -scheme is the incorrect identification of the volume of the MFRs. Admittedly, the physical quantities involving nonpotentiality (*i.e.*, T_w or α) may be useful to indicate the presence of an MFR. However, employing a strict twist threshold (here $|T_w| \geq 0.2$), or other parameters based on common measures of magnetic nonpotentiality, can be an insufficient condition for isolating the main body of an MFR, and the correct identification of the MFR can greatly impact any prediction of an event's associated CME production. Moreover, although the q -scheme correctly classified the three target events whereas the r -schemes had so failed, overall for the 51 events studied, the classification performance stayed the same between the two schemes, with a moderate level of success. We propose that there is likely to be more than one mechanism governing CME production. Finally, the results presented in this study demonstrate that the argument regarding whether a flare will erupt with a CME or not, should be redefined as the question of how to accurately extract the relevant magnetic flux rope characteristics from the observations.

Chapter 5

Conclusions and Future Work

In this thesis, we considered the balance between the non-potential magnetic configuration (magnetic flux rope; MFR in this study) and the magnetic field in its immediate vicinity, with a focus on its feasibility for determining the nature of eruptivities of coronal mass ejections (CMEs) for an active region (AR). In the first part of this thesis, the r_m parameter is proposed to approximate the balance, which is defined by:

$$r_m = \frac{\Phi_{T_w \geq T_c}}{\Phi_{\text{surrounding}} + \Phi_{T_w \geq T_c}}, \quad (5.1)$$

where $\Phi_{T_w \geq T_c}$ is the highly twisted magnetic flux used to approach the reconnected flux has been contributed by an MFR. The term $\Phi_{\text{surrounding}}$ is the magnetic flux at the nearby field lines that suppress the MFR. We estimated the value of r_m across each event listed in Table 2.1, and statistically evaluate the difference of r_m values between the eruptive and confined groups. The linear discriminant analysis applied in this study suggested that a larger discrepancy could be found using $r_m^{\text{o+w}}$ compared to r_m^{o} . This result implies that the wall field – which is the field lines that are fencing in the highly twisted field – indeed provide confinement to a CME onset.

In the second part of this thesis, as an extension of r_m , the r - and q -scheme are designed to estimate the likelihood that a flare would be eruptive, where the r -scheme uses highly-twisted fieldlines to represent the MFRs, and the q -scheme applied the flare-ribbon-associated fieldlines to approach the MFRs. The conclusions presented in this work show that both q -scheme and r -scheme was able to independently determine the association of a flare with an accompanying CME; however, the CME-eruptivity classification success for the three target events (events listed in Table 4.1) can only be improved with the q -scheme. An analysis based on torus instability (TI) performed on events #35-37 demonstrates that the failure classification in r_m could arise from incorrectly

isolating the volume of the MFRs from the background: the highly-twisted field lines are in fact TI-susceptible, which is inconsistent with the observed CME-eruptivity (events #35-37 are all reported to be confined). We argued that part of the highly-twisted field lines could have inadequate α values but with long field-line length, such that field lines certifying $|T_w| \geq 0.2$ might still be potential-like. However, we found no significant difference between the flare-associated field lines and the highly twisted field lines in terms of their α profiles. On the other hand, the properties based on magnetic morphology (*e.g.*, L in this study) could be more indicative for identifying the MFRs.

In this work, neither r - nor q -scheme cannot provide a perfect performance for determining the CME-eruptivity, which implies that multiple mechanisms are involved in the CME-eruptivity. Certainly, it is far beyond the scope of this work to provide conclusive solutions for including all the possible CME-initialization mechanisms. Here, we made effort to give possible answers of the fundamental problems addressed in the introduction (§1.4). These issues include the specific definition of an MFR, identification of real straddling field acting on MFRs, and if the magnetic field’s topology is crucial for the eruptivity. We expect that these general questions could also be existing in most of the current CME-forecasting-related researches.

The method for defining MFRs is a stated issue in the research of CME-initialization. The results presented in the $\alpha - L$ diagram (Figure 4.9) implies that there is no significant difference found between the MFRs and their immediate vicinity based on any physical quantities involving nonpotentiality (*i.e.*, T_w and α), at least in the events originating from NOAA AR 12192. On the contrary, one of the most striking features appears in the three target events is that the reconnect-imminent field lines are all short field lines. This result entails significant implications for the eruptivity-diagnosis of an active region that typology of the field line might play an important role in determining MFRs. We suspect that some tools based on topological properties might provide further information. For instance, quasi-separatrix layers analysis (Titov, 2007, Titov et al., 2002), which is a method that can group the field lines with different connectivity and could possibly provide additional hints regarding the true locus of a MFR.

Having proposed hypotheses to isolate the strapping field lines from the background, we develop a whole-automatic procedure to identify the overlying and wall field. With this approach, one can exclude the field line that is supposed to have no interaction with the MFR. The refinement of the straddling field is shown to be able to improve the diagnosis of eruptivity: with comparing the discriminant function analysis metrics of r_m and $|\Phi|_{\text{Ribbon}}/|\Phi|_{\text{AR}}$ (Toriumi et al., 2017) presented in Table 3.3, we found that including the overlying and wall field specifically can indeed enhance the resulting classification of eruptive/confined events. As an extension of this analysis, we expect that there might be additional confining field out of the NLFFF numerical domain; the field lines with a

larger scale can be tested to improve the r - and q -scheme in future work. These large-scale fieldlines could be inferred by applying the potential field source-surface model (which has been introduced in §2.3.1).

The analysis corresponding to the geometry of the surrounding field implies that the field line morphology could affect the eruptivity hosted by an eruption. Despite the fact that much of the previous results attempted to estimate the field strength *only above* the eruption site, the statistical results demonstrate that wall field, which is field fencing in the MFR instead of across over it, can also give confinements to an eruption and casing confined events. We therefore wonder that if the topological analysis of the ambient field can be served as the extension of the r_m analysis, it appears worthwhile to investigate the topological properties that might facilitate the lifting-up of an MFR, or, suppress the MFR in the future. for instance, some special magnetical structure (*e.g.*, magnetic null point) might be associated with the CME-eruptivity (*e.g.*, Chintzoglou et al., 2017, DeRosa & Barnes, 2018).

Finally, another possibility that can increase the robustness of this work could be enlarging the sample size of the event list for analysis. Since the present conclusions are mainly inferred from the statistical approach, large sample size could strengthen the conclusions we have shown in this work, particularly, reducing the uncertainties estimated by the bootstrap method. In future research, we expect to be able to provide a more robust conclusion with a greater number of events than is implemented in this study.

References

- Alexander, D., Liu, R., & Gilbert, H. R. (2006). Hard X-ray production in a failed filament eruption. *Astrophysical Journal*, *653*(1), 719.
- Alissandrakis, C. (1981). On the computation of constant alpha force-free magnetic field. *Astronomy and Astrophysics*, *100*, 197–200.
- Altschuler, M. D., & Newkirk, G. (1969). Magnetic fields and the structure of the solar corona. *Solar Physics*, *9*(1), 131–149.
- Amari, T., Aly, J.-J., Mikic, Z., & Linker, J. (2010). Coronal mass ejection initiation: on the nature of the flux cancellation model. *The Astrophysical Journal Letters*, *717*(1), L26.
- Andersen, H., Larsen, S., Spliid, H., & Christensen, N. D. (1999). Multivariate statistical analysis of organ weights in toxicity studies. *Toxicology*, *136*(2-3), 67–77.
- Andrews, M. (2003). A search for CMEs associated with big flares. *Solar Physics*, *218*(1/2), 261–279.
- Antiochos, S. K., DeVore, C. R., & Klimchuk, J. A. (1999). A model for solar coronal mass ejections. *Astrophysical Journal*, *510*(1), 485–493.
- Antonucci, E., & Dennis, B. (1983). Observation of chromospheric evaporation during the solar maximum mission. In *Recent Advances in the Understanding of Solar Flares*, (pp. 67–77). Springer.
- Archontis, V., & Török, T. (2008). Eruption of magnetic flux ropes during flux emergence. *Astronomy & Astrophysics*, *492*(2), L35–L38.
- Aulanier, G., DeLuca, E., Antiochos, S., McMullen, R., & Golub, L. (2000). The topology and evolution of the bastille day flare. *The Astrophysical Journal*, *540*(2), 1126.

- Aulanier, G., Démoulin, P., van Driel-Gesztelyi, L., Mein, P., & Deforest, C. (1998). 3-D magnetic configurations supporting prominences. II. The lateral feet as a perturbation of a twisted flux-tube. *Astronomy and Astrophysics*, *335*, 309–322.
- Bamba, Y., Lee, K.-S., Imada, S., & Kusano, K. (2017). Study on precursor activity of the X1.6 flare in the great AR 12192 with SDO, IRIS, and Hinode. *Astrophysical Journal*, *840*(2), 116.
- Bateman, G., & Grimm, R. C. (1979). MHD instabilities. *Physics Today*, *32*(10), 61–62.
- Baumgartner, C., Thalmann, J. K., & Veronig, A. M. (2018). On the factors determining the eruptive character of solar flares. *Astrophysical Journal*, *853*, 105.
- Berger, M. A., & Prior, C. (2006). The writhe of open and closed curves. *Journal of Physics A: Mathematical and General*, *39*(26), 8321–8348.
- Bloomfield, D. S., Higgins, P. A., McAteer, R. J., & Gallagher, P. T. (2012). Toward reliable benchmarking of solar flare forecasting methods. *The Astrophysical Journal Letters*, *747*(2), L41.
- Borrero, J., Tomczyk, S., Kubo, M., Socas-Navarro, H., Schou, J., Couvidat, S., & Bogart, R. (2011). VFISV: very fast inversion of the stokes vector for the helioseismic and magnetic imager. *Solar Physics*, *273*(1), 267–293.
- Burlaga, L., Sittler, E., Mariani, F., & Schwenn, a. R. (1981). Magnetic loop behind an interplanetary shock: Voyager, Helios, and IMP 8 observations. *Journal of Geophysical Research: Space Physics*, *86*(A8), 6673–6684.
- Carmichael, H. (1964). 54 a process for flares. In *AAS NASA Symposium on the Physics of Solar Flares: Proceedings of a Symposium Held at the Goddard Space Flight Center, Greenbelt, Maryland, October 28-30, 1963*, vol. 50, (p. 451). National Aeronautics and Space Administration.
- Carrington, R. C. (1859). Description of a singular appearance seen in the Sun on September 1, 1859. *Monthly Notices of the Royal Astronomical Society*, *20*, 13–15.
- Chen, H., Zhang, J., Cheng, X., Ma, S., Yang, S., & Li, T. (2014). Direct observations of tether-cutting reconnection during a major solar event from 2014 February 24 to 25. *The Astrophysical Journal Letters*, *797*(2), L15.
- Chen, H., Zhang, J., Ma, S., Yang, S., Li, L., Huang, X., & Xiao, J. (2015). Confined flares in solar active region 12192 from 2014 October 18 to 29. *The Astrophysical Journal Letters*, *808*(1), L24.

- Chen, J., Howard, R., Brueckner, G., Santoro, R., Krall, J., Paswaters, S., Cyr, O. S., Schwenn, R., Lamy, P., & Simnett, G. (1997). Evidence of an erupting magnetic flux rope: LASCO coronal mass ejection of 1997 April 13. *The Astrophysical Journal Letters*, *490*(2), L191.
- Chen, P. (2011). Coronal mass ejections: models and their observational basis. *Living Reviews in Solar Physics*, *8*(1), 1.
- Cheng, X., Guo, Y., & Ding, M. (2017). Origin and structures of solar eruptions I: magnetic flux rope. *Science China Earth Sciences*, *60*(8), 1383–1407.
- Cheng, X., Zhang, J., Ding, M., Guo, Y., & Su, J. (2011). A comparative study of confined and eruptive flares in NOAA AR 10720. *The Astrophysical Journal*, *732*(2), 87.
- Cheng, X., Zhang, J., Ding, M. D., & Poomvises, W. (2010). A statistical study of the post-impulsive-phase acceleration of flare-associated coronal mass ejections. *Astrophysical Journal*, *712*(1), 752–760.
- Chintzoglou, G., Vourlidas, A., Savcheva, A., Tassev, S., Beltran, S. T., & Stenborg, G. (2017). Magnetic flux rope shredding by a hyperbolic flux tube: The detrimental effects of magnetic topology on solar eruptions. *Astrophysical Journal*, *843*(2), 93.
- Chiu, Y., & Hilton, H. (1977). Exact green's function method of solar force-free magnetic-field computations with constant alpha. I-theory and basic test cases. *The Astrophysical Journal*, *212*, 873–885.
- Cremades, H., & Bothmer, V. (2004). On the three-dimensional configuration of coronal mass ejections. *Astronomy & Astrophysics*, *422*(1), 307–322.
- Cui, Y., Wang, H., Xu, Y., & Liu, S. (2018). Statistical study of magnetic topology for eruptive and confined solar flares. *Journal of Geophysical Research: Space Physics*.
- Dedner, A., Kemm, F., Kröner, D., Munz, C.-D., Schnitzer, T., & Wesenberg, M. (2002). Hyperbolic divergence cleaning for the MHD equations. *Journal of Computational Physics*, *175*(2), 645–673.
- Démoulin, P., & Aulanier, G. (2010). Criteria for flux rope eruption: non-equilibrium versus torus instability. *Astrophysical Journal*, *718*(2), 1388–1399.
- Dere, K., Brueckner, G., Howard, R., Michels, D., & Delaboudiniere, J. (1999). LASCO and EIT observations of helical structure in coronal mass ejections. *Astrophysical Journal*, *516*(1), 465.

- DeRosa, M., Wheatland, M., Leka, K., Barnes, G., Amari, T., Canou, A., Gilchrist, S., Thalmann, J., Valori, G., Wiegmann, T., et al. (2015). The influence of spatial resolution on nonlinear force-free modeling. *The Astrophysical Journal*, *811*(2), 107.
- DeRosa, M. L., & Barnes, G. (2018). Does nearby open flux affect the eruptivity of solar active regions? *Astrophysical Journal*, *861*(2), 131.
- DeRosa, M. L., Schrijver, C. J., Barnes, G., Leka, K., Lites, B. W., Aschwanden, M. J., Amari, T., Canou, A., McTiernan, J. M., Régnier, S., et al. (2009). A critical assessment of nonlinear force-free field modeling of the solar corona for active region 10953. *The Astrophysical Journal*, *696*(2), 1780.
- Doyle, L., Wyper, P. F., Scullion, E., McLaughlin, J. A., Ramsay, G., & Doyle, J. G. (2019). Observations and 3D magnetohydrodynamic modeling of a confined helical jet launched by a filament eruption. *The Astrophysical Journal*, *887*(2), 246.
- Duan, A., Jiang, C., He, W., Feng, X., Zou, P., & Cui, J. (2019). A study of pre-flare solar coronal magnetic fields: Magnetic flux ropes. *Astrophysical Journal*, *884*(1), 73.
- Falconer, D., Moore, R., & Gary, G. (2002). Correlation of the coronal mass ejection productivity of solar active regions with measures of their global nonpotentiality from vector magnetograms: Baseline results. *The Astrophysical Journal*, *569*(2), 1016.
- Fan, Y., & Gibson, S. (2006). On the nature of the X-ray bright core in a stable filament channel. *The Astrophysical Journal Letters*, *641*(2), L149.
- Fan, Y., & Gibson, S. E. (2007). Onset of coronal mass ejections due to loss of confinement of coronal flux ropes. *Astrophysical Journal*, *668*(2), 1232–1245.
- Filippov, B. (2020). Failed prominence eruptions near 24 cycle maximum. *Monthly Notices of the Royal Astronomical Society*, *494*(2), 2166–2177.
- Filippov, B., Martsenyuk, O., Srivastava, A. K., & Uddin, W. (2015). Solar magnetic flux ropes. *Journal of Astrophysics and Astronomy*, *36*(1), 157–184.
- Forbes, T. (2000). A review on the genesis of coronal mass ejections. *Journal of Geophysical Research: Space Physics*, *105*(A10), 23153–23165.
- Gary, G. A. (2001). Plasma beta above a solar active region: Rethinking the paradigm. *Solar Physics*, *203*(1), 71–86.

- Gibson, S., & Fan, Y. (2006). The partial expulsion of a magnetic flux rope. *The Astrophysical Journal Letters*, 637(1), L65.
- Gibson, S., Fan, Y., Török, T., & Kliem, B. (2006). The evolving sigmoid: evidence for magnetic flux ropes in the corona before, during, and after CMEs. *Space science reviews*, 124(1-4), 131–144.
- Gopalswamy, N., & Kundu, M. (1992). Estimation of the mass of a coronal mass ejection from radio observations. *The Astrophysical Journal*, 390, L37–L39.
- Gopalswamy, N., Lara, A., Yashiro, S., Nunes, S., & Howard, R. A. (2003). Coronal mass ejection activity during solar cycle 23. In *Solar Variability as an Input to the Earth's Environment*, vol. 535, (pp. 403–414).
- Gosling, J. T. (1990). Coronal mass ejections and magnetic flux ropes in interplanetary space. *Physics of magnetic flux ropes*, 58, 343–364.
- Green, L. M., & Kliem, B. (2009). Flux rope formation preceding coronal mass ejection onset. *The Astrophysical Journal Letters*, 700(2), L83.
- Green, L. M., Kliem, B., & Wallace, A. (2011). Photospheric flux cancellation and associated flux rope formation and eruption. *Astronomy & Astrophysics*, 526, A2.
- Guo, Y., Ding, M., Schmieder, B., Li, H., Török, T., & Wiegmann, T. (2010). Driving mechanism and onset condition of a confined eruption. *The Astrophysical Journal Letters*, 725(1), L38.
- Hanssen, A., & Kuipers, W. (1965). *On the Relationship Between the Frequency of Rain and Various Meteorological Parameters. (With Reference to the Problem of Objective Forecasting)*. Koninklijk Nederlands Meteorologisch Instituut.
- Harra, L. K., Schrijver, C. J., Janvier, M., Toriumi, S., Hudson, H., Matthews, S., Woods, M. M., Hara, H., Guedel, M., Kowalski, A., Osten, R., Kusano, K., & Lueftinger, T. (2016). The characteristics of solar X-class flares and CMEs: a paradigm for stellar superflares and eruptions? *Solar Physics*, 291(6), 1761–1782.
- Harrison, R. (1995). The nature of solar flares associated with coronal mass ejection. *Astronomy & Astrophysics*, 304, 585.
- Harrison, R. (2003). SOHO observations relating to the association between flares and coronal mass ejections. *Advances in Space Research*, 32(12), 2425–2437.

- Hesse, M., & Cassak, P. (2020). Magnetic reconnection in the space sciences: past, present, and future. *Journal of Geophysical Research: Space Physics*, *125*(2), e2018JA025935.
- Hiei, E., Hundhausen, A., & Sime, D. (1993). Reformation of a coronal helmet streamer by magnetic reconnection after a coronal mass ejection. *Geophysical research letters*, *20*(24), 2785–2788.
- Hills, M. (1966). Allocation rules and their error rates. *Journal of the Royal Statistical Society: Series B (Methodological)*, *28*(1), 1–20.
- Hirayama, T. (1974). Theoretical model of flares and prominences. *Solar Physics*, *34*(2), 323–338.
- Hodgson, R. (1859). On a curious appearance seen in the Sun. *Monthly Notices of the Royal Astronomical Society*, *20*, 15–16.
- Hood, A. W., & Priest, E. R. (1979). Kink instability of solar coronal loops as the cause of solar flares. *Solar Physics*, *64*(2), 303–321.
- House, L., Wagner, W., Hildner, E., Sawyer, C., & Schmidt, H. (1981). Studies of the corona with the solar maximum mission coronagraph/polarimeter. *The Astrophysical Journal*, *244*, L117–L121.
- Hoyng, P., Duijveman, A., Machado, M. E., Rust, D. M., Svestka, Z., Boelee, A., de Jager, C., Frost, K. T., Lafleur, H., Simnett, G. M., van Beek, H. F., & Woodgate, B. E. (1981). Origin and location of the hard X-Ray emission in a two-ribbon flare. *The Astrophysical Journal*, *246*, L155.
- Hudson, H., Acton, L., & Freeland, S. (1996). A long-duration solar flare with mass ejection and global consequences. *The Astrophysical Journal*, *470*, 629.
- Hudson, H., Kosugi, T., Nitta, N., & Shimojo, M. (2001). Hard X-radiation from a fast coronal ejection. *The Astrophysical Journal Letters*, *561*(2), L211.
- Illing, R., & Hundhausen, A. (1985). Observation of a coronal transient from 1.2 to 6 solar radii. *Journal of Geophysical Research: Space Physics*, *90*(A1), 275–282.
- Inoue, S., Hayashi, K., & Kusano, K. (2016). Structure and stability of magnetic fields in solar active region 12192 based on nonlinear force-free field modeling. *Astrophysical Journal*, *818*(2), 168.
- Inoue, S., Hayashi, K., Magara, T., Choe, G. S., & Park, Y. D. (2014a). Magnetohydrodynamic simulation of the X2.2 solar flare on 2011 February 15. I. comparison with the observations. *Astrophysical Journal*, *788*(2), 182.

- Inoue, S., Hayashi, K., Magara, T., Choe, G. S., & Park, Y. D. (2015). Magnetohydrodynamic simulation of the X2.2 solar flare on 2011 February 15. II. dynamics connecting the solar flare and the coronal mass ejection. *Astrophysical Journal*, *803*(2), 73.
- Inoue, S., Hayashi, K., Shiota, D., Magara, T., & Choe, G. S. (2013). Magnetic structure producing X- and M-class solar flares in solar active region 11158. *Astrophysical Journal*, *770*(1), 79.
- Inoue, S., Kusano, K., Magara, T., Shiota, D., & Yamamoto, T. T. (2011). Twist and connectivity of magnetic field lines in the solar active region NOAA 10930. *Astrophysical Journal*, *738*(2), 161.
- Inoue, S., Magara, T., Pandey, V., Shiota, D., Kusano, K., Choe, G., & Kim, K. (2014b). Non-linear force-free extrapolation of the coronal magnetic field based on the magnetohydrodynamic relaxation method. *The Astrophysical Journal*, *780*(1), 101.
- Ishiguro, N., & Kusano, K. (2017). Double arc instability in the solar corona. *Astrophysical Journal*, *843*(2), 101.
- Jackson, B. (1985). Imaging of coronal mass ejections by the helios spacecraft. *Solar physics*, *100*(1-2), 563–574.
- Ji, H., Wang, H., Schmahl, E. J., Moon, Y.-J., & Jiang, Y. (2003). Observations of the failed eruption of a filament. *The Astrophysical Journal Letters*, *595*(2), L135.
- Jiang, C., & Feng, X. (2012). A new implementation of the magnetohydrodynamics-relaxation method for nonlinear force-free field extrapolation in the solar corona. *The Astrophysical Journal*, *749*(2), 135.
- Jiang, C., Wu, S. T., Yurchyshyn, V., Wang, H., Feng, X., & Hu, Q. (2016). How did a major confined flare occur in super solar active region 12192? *Astrophysical Journal*, *828*(1), 62.
- Jing, J., Liu, C., Lee, J., Ji, H., Liu, N., Xu, Y., & Wang, H. (2018). Statistical analysis of torus and kink instabilities in solar eruptions. *Astrophysical Journal*, *864*(2), 138.
- Jing, J., Tan, C., Yuan, Y., Wang, B., Wiegmann, T., Xu, Y., & Wang, H. (2010). Free magnetic energy and flare productivity of active regions. *The Astrophysical Journal*, *713*(1), 440–449.
- Jing, J., Xu, Y., Lee, J., Nitta, N. V., Liu, C., Park, S.-H., Wiegmann, T., & Wang, H. (2015). Comparison between the eruptive X2.2 flare on 2011 February 15 and confined X3.1 flare on 2014 October 24. *Research in Astronomy and Astrophysics*, *15*(9), 1537–1546.

- Jing, J., Yurchyshyn, V. B., Yang, G., Xu, Y., & Wang, H. (2004). On the relation between filament eruptions, flares, and coronal mass ejections. *The Astrophysical Journal*, *614*(2), 1054.
- Kahler, S. W. (1992). Solar flares and coronal mass ejections. *Annual Review of Astronomy and Astrophysics*, *30*(1), 113–141.
- Kahler, S. W., N. R., J. S., & Liggett, M. (1989). Coronal mass ejections and associated X-ray flare durations. *Astrophysical Journal*, *344*, 1026.
- Kang, J., Inoue, S., Kusano, K., Park, S.-H., & Moon, Y.-J. (2019). Onset mechanism of M6.5 solar flare observed in active region 12371. *The Astrophysical Journal*, *887*(2), 263.
- Kang, J., Magara, T., Inoue, S., Kubo, Y., & Nishizuka, N. (2016). Distribution characteristics of coronal electric current density as an indicator for the occurrence of a solar flare. *Publications of the Astronomical Society of Japan*, *68*(6), 101.
- Kazachenko, M. D., Lynch, B. J., Welsch, B. T., & Sun, X. (2017). A database of flare ribbon properties from the Solar Dynamics Observatory. I. Reconnection flux. *The Astrophysical Journal*, *845*(1), 49.
- Kendall, M., Stuart, A., & Ord, J. K. (1983). Classification: discrimination and clustering. *The advanced theory of statistics*, *3*, 370–421.
- Kliem, B., Lin, J., Forbes, T., Priest, E., & Török, T. (2014). Catastrophe versus instability for the eruption of a toroidal solar magnetic flux rope. *The Astrophysical Journal*, *789*(1), 46.
- Kliem, B., Titov, V., & Török, T. (2004). Formation of current sheets and sigmoidal structure by the kink instability of a magnetic loop. *Astronomy & Astrophysics*, *413*(3), L23–L26.
- Kliem, B., & Török, T. (2006). Torus instability. *Physical Review Letters*, *96*(25).
- Kopp, R., & Pneuman, G. (1976). Magnetic reconnection in the corona and the loop prominence phenomenon. *Solar Physics*, *50*(1), 85–98.
- Krall, K., Smith, J., Hagyard, M., West, E., & Cummings, N. (1982). Vector magnetic field evolution, energy storage, and associated photospheric velocity shear within a flare-productive active region. *Solar Physics*, *79*(1), 59–75.
- Kuperus, M., & Raadu, M. (1974). The support of prominences formed in neutral sheets. *Astronomy and Astrophysics*, *31*, 189.

- Kuridze, D., Mathioudakis, M., Kowalski, A., Keys, P., Jess, D., Balasubramaniam, K., & Keenan, F. (2013). Failed filament eruption inside a coronal mass ejection in active region 11121. *Astronomy & Astrophysics*, *552*, A55.
- Kusano, K., Iju, T., Bamba, Y., & Inoue, S. (2020). A physics-based method that can predict imminent large solar flares. *Science*, *369*(6503), 587–591.
- Kushwaha, U., Joshi, B., Veronig, A. M., & Moon, Y.-J. (2015). Large-scale contraction and subsequent disruption of coronal loops during various phases of the M6. 2 flare associated with the confined flux rope eruption. *Astrophysical Journal*, *807*(1), 101.
- Leamon, R. J., Canfield, R. C., Blehm, Z., & Pevtsov, A. A. (2003). What is the role of the kink instability in solar coronal eruptions? *The Astrophysical Journal*, *596*(2), L255–L258.
- Leka, K., & Barnes, G. (2007). Photospheric magnetic field properties of flaring versus flare-quiet active regions. IV. A statistically significant sample. *Astrophysical Journal*, *656*(2), 1173.
- Leka, K., Barnes, G., Crouch, A., Metcalf, T. R., Gary, G. A., Jing, J., & Liu, Y. (2009). Resolving the 180 ambiguity in solar vector magnetic field data: Evaluating the effects of noise, spatial resolution, and method assumptions. *Solar Physics*, *260*(1), 83–108.
- Leka, K., Fan, Y., & Barnes, G. (2005). On the availability of sufficient twist in solar active regions to trigger the kink instability. *Astrophysical Journal*, *626*(2), 1091.
- Leka, K., & Skumanich, A. (1999). On the value of ‘ α_{ar} ’ from vector magnetograph data. *Solar Physics*, *188*(1), 3–19.
- Leka, K. D., & Barnes, G. (2003). Photospheric magnetic field properties of flaring versus flare-quiet active regions. II. discriminant analysis. *Astrophysical Journal*, *595*(2), 1296–1306.
- Lemen, J. R., Akin, D. J., Boerner, P. F., Chou, C., Drake, J. F., Duncan, D. W., Edwards, C. G., Friedlaender, F. M., Heyman, G. F., Hurlburt, N. E., et al. (2011). The atmospheric imaging assembly (AIA) on the solar dynamics observatory (SDO). In *The solar dynamics observatory*, (pp. 17–40). Springer.
- Lepping, R., Jones, J., & Burlaga, L. (1990). Magnetic field structure of interplanetary magnetic clouds at 1 AU. *Journal of Geophysical Research: Space Physics*, *95*(A8), 11957–11965.
- Lin, J., & Forbes, T. (2000). Effects of reconnection on the coronal mass ejection process. *Journal of Geophysical Research: Space Physics*, *105*(A2), 2375–2392.

- Liu, C., Deng, N., Lee, J., Wiegmann, T., Moore, R. L., & Wang, H. (2013). Evidence for solar tether-cutting magnetic reconnection from coronal field extrapolations. *The Astrophysical Journal Letters*, *778*(2), L36.
- Liu, R., Kliem, B., Titov, V. S., Chen, J., Wang, Y., Wang, H., Liu, C., Xu, Y., & Wiegmann, T. (2016). Structure, stability, and evolution of magnetic flux ropes from the perspective of magnetic twist. *Astrophysical Journal*, *818*(2), 148.
- Liu, Y. (2008). Magnetic field overlying solar eruption regions and kink and torus instabilities. *Astrophysical Journal*, *679*(2), L151–L154.
- Liu, Y., Hoeksema, J. T., Sun, X., & Hayashi, K. (2017). Vector magnetic field synoptic charts from the Helioseismic and Magnetic Imager (HMI). *Solar Physics*, *292*(2), 29.
- Liu, Y., Su, J., Xu, Z., Lin, H., Shibata, K., & Kurokawa, H. (2009). New observation of failed filament eruptions: The influence of asymmetric coronal background fields on solar eruptions. *The Astrophysical Journal Letters*, *696*(1), L70.
- Longcope, D., Beveridge, C., Qiu, J., Ravindra, B., Barnes, G., & Dasso, S. (2007). Modeling and measuring the flux reconnected and ejected by the two-ribbon flare/CME event on 7 November 2004. *Solar Physics*, *244*(1-2), 45–73.
- Low, B., & Hundhausen, J. (1995). Magnetostatic structures of the solar corona. 2: The magnetic topology of quiescent prominences. *The Astrophysical Journal*, *443*, 818–836.
- Machado, M. E., Moore, R. L., Hernandez, A. M., Rovira, M. G., Hagyard, M. J., & Smith Jr, J. B. (1988). The observed characteristics of flare energy release. I-Magnetic structure at the energy release site. *The Astrophysical Journal*, *326*, 425–450.
- MacQueen, R., Eddy, J., Gosling, J., Hildner, E., Munro, R., Newkirk Jr, G., Poland, A., & Ross, C. (1974). The outer solar corona as observed from Skylab: Preliminary results. *The Astrophysical Journal*, *187*, L85.
- MacTaggart, D., & Hood, A. W. (2009). Multiple eruptions from magnetic flux emergence. *Astronomy & Astrophysics*, *508*(1), 445–449.
- Maričić, D., Vršnak, B., Stanger, A. L., Veronig, A. M., Temmer, M., & Roša, D. (2007). Acceleration phase of coronal mass ejections: II. Synchronization of the energy release in the associated flare. *Solar Physics*, *241*(1), 99–112.

- Mariska, J. T., Sakao, T., & Bentley, R. (1996). Hard and soft X-ray observations of solar limb flares. *The Astrophysical Journal*, *459*, 815.
- Masuda, S., Kosugi, T., Hara, H., Tsuneta, S., & Ogawara, Y. (1994). A loop-top hard X-ray source in a compact solar flare as evidence for magnetic reconnection. *Nature*, *371*(6497), 495–497.
- McClymont, A., & Mikic, Z. (1994). Thickness variations along coronal loops inferred from vector magnetograph data. *The Astrophysical Journal*, *422*, 899–905.
- Metcalf, T. R. (1994). Resolving the 180-degree ambiguity in vector magnetic field measurements: The ‘minimum’ energy solution. *Solar Physics*, *155*(2), 235–242.
- Metcalf, T. R., DeRosa, M. L., Schrijver, C. J., Barnes, G., van Ballegooijen, A. A., Wiegmann, T., Wheatland, M. S., Valori, G., & McTiernan, J. M. (2008). Nonlinear force-free modeling of coronal magnetic fields. II. modeling a filament arcade and simulated chromospheric and photospheric vector fields. *Solar Physics*, *247*(2), 269–299.
- Metcalf, T. R., Jiao, L., McClymont, A. N., Canfield, R. C., & Uitenbroek, H. (1995). Is the solar chromospheric magnetic field force-free? *The Astrophysical Journal*, *439*, 474–481.
- Mikic, Z., Barnes, D., & Schnack, D. (1988). Dynamical evolution of a solar coronal magnetic field arcade. *The Astrophysical Journal*, *328*, 830–847.
- Milligan, R. O., Gallagher, P. T., Mathioudakis, M., & Keenan, F. P. (2006). Observational evidence of gentle chromospheric evaporation during the impulsive phase of a solar flare. *The Astrophysical Journal Letters*, *642*(2), L169.
- Moore, R. L., Sterling, A. C., Hudson, H. S., & Lemen, J. R. (2001). Onset of the magnetic explosion in solar flares and coronal mass ejections. *Astrophysical Journal*, *552*(2), 833–848.
- Muhamad, J., Kusano, K., Inoue, S., & Bamba, Y. (2018). A study of magnetic field characteristics of the flaring active region based on nonlinear force-free field extrapolation. *Astrophysical Journal*, *863*(2), 162.
- Munro, R., Gosling, J., Hildner, E., MacQueen, R., Poland, A., & Ross, C. (1979). The association of coronal mass ejection transients with other forms of solar activity. *Solar Physics*, *61*(1), 201–215.
- Myers, C. E., Yamada, M., Ji, H., Yoo, J., Fox, W., Jara-Almonte, J., Savcheva, A., & DeLuca, E. E. (2015). A dynamic magnetic tension force as the cause of failed solar eruptions. *Nature*, *528*(7583), 526–529.

- Möstl, C., Rollett, T., Frahm, R. A., Liu, Y. D., Long, D. M., Colaninno, R. C., Reiss, M. A., Temmer, M., Farrugia, C. J., Posner, A., Dumbović, M., Janvier, M., Démoulin, P., Boakes, P., Devos, A., Kraaikamp, E., Mays, M. L., & Vršnak, B. (2015). Strong coronal channelling and interplanetary evolution of a solar storm up to earth and mars. *Nature Communications*, *6*(1).
- Nakagawa, Y. (1974). Dynamics of the solar magnetic field. I. method of examination of force-free magnetic fields. *The Astrophysical Journal*, *190*, 437–440.
- Nindos, A., Patsourakos, S., & Wiegmann, T. (2012). On the role of the background overlying magnetic field in solar eruptions. *Astrophysical Journal*, *748*(1), L6.
- Pagano, P., Mackay, D. H., & Yardley, S. L. (2019). A prospective new diagnostic technique for distinguishing eruptive and noneruptive active regions. *Astrophysical Journal*, *883*(2), 112.
- Panesar, N. K., Sterling, A. C., & Moore, R. L. (2016). Homologous jet-driven coronal mass ejections from solar active region 12192. *Astrophysical Journal*, *822*(2), L23.
- Priest, E., & Forbes, T. (2002). The magnetic nature of solar flares. *Astronomy & Astrophysics Reviews*, *10*(4), 313–377.
- Priest, E., Hood, A., & Anzer, U. (1989). A twisted flux-tube model for solar prominences. I-General properties. *The Astrophysical Journal*, *344*, 1010–1025.
- Qiu, J. (2009). Observational analysis of magnetic reconnection sequence. *Astrophysical Journal*, *692*(2), 1110.
- Qiu, J., Liu, W., Hill, N., & Kazachenko, M. (2010). Reconnection and energetics in two-ribbon flares: a revisit of the bastille-day flare. *The Astrophysical Journal*, *725*(1), 319.
- Qiu, J., Liu, W.-J., & Longcope, D. W. (2012). Heating of flare loops with observationally constrained heating functions. *Astrophysical Journal*, *752*(2), 124.
- Riley, P., Lionello, R., Mikić, Z., & Linker, J. (2008). Using global simulations to relate the three-part structure of coronal mass ejections to in situ signatures. *The Astrophysical Journal*, *672*(2), 1221.
- Rust, D. M., & Kumar, A. (1996). Evidence for helically kinked magnetic flux ropes in solar eruptions. *The Astrophysical Journal Letters*, *464*(2), L199.
- Saito, K., & Hyder, C. L. (1968). A concentric ellipse multiple-arch system in the solar corona. *Solar Physics*, *5*(1), 61–86.

- Saito, K., & Tandberg-Hanssen, E. (1973). The arch systems, cavities and prominences in the helmet streamer observed at the solar eclipse, November 12, 1966. *Solar Physics*, *31*(1), 105–121.
- Sakurai, T. (1976). Magnetohydrodynamic interpretation of the motion of prominences. *Publications of the Astronomical Society of Japan*, *28*, 177–198.
- Sakurai, T. (1981). Calculation of force-free magnetic field with non-constant α . *Solar physics*, *69*(2), 343–359.
- Sakurai, T. (1982). Green's function methods for potential magnetic fields. *Solar Physics*, *76*(2), 301–321.
- Savcheva, A. S., Green, L. M., van Ballegooijen, A. A., & DeLuca, E. E. (2012). Photospheric flux cancellation and the build-up of sigmoidal flux ropes on the sun. *Astrophysical Journal*, *759*(2), 105.
- Schou, J., Scherrer, P. H., Bush, R. I., Wachter, R., Couvidat, S., Rabello-Soares, M. C., Bogart, R. S., Hoeksema, J., Liu, Y., Duvall, T., et al. (2012). Design and ground calibration of the helioseismic and magnetic imager (HMI) instrument on the solar dynamics observatory (SDO). *Solar Physics*, *275*(1-2), 229–259.
- Schrijver, C. J., DeRosa, M. L., Metcalf, T., Barnes, G., Lites, B., Tarbell, T., McTiernan, J., Valori, G., Wiegmann, T., Wheatland, M. S., Amari, T., Aulanier, G., Démoulin, P., Fuhrmann, M., Kusano, K., Régnier, S., & Thalmann, J. K. (2008). Nonlinear force-free field modeling of a solar active region around the time of a major flare and coronal mass ejection. *The Astrophysical Journal*, *675*(2), 1637–1644.
- Sheeley Jr, N., Howard, R., Koomen, M., & Michels, D. (1983). Associations between coronal mass ejections and soft X-ray events. *Astrophysical Journal*, *272*, 349–354.
- Shibata, K. (1998). Evidence of magnetic reconnection in solar flares and a unified model of flares. *Astrophysics and Space Science*, *264*(1-4), 129–144.
- Shibata, K., & Magara, T. (2011). Solar flares: magnetohydrodynamic processes. *Living Reviews in Solar Physics*, *8*(1), 6.
- Shibata, K. c., Masuda, S., Shimojo, M., Hara, H., Yokoyama, T., Tsuneta, S., Kosugi, T., & Ogawara, Y. (1995). Hot-plasma ejections associated with compact-loop solar flares. *The Astrophysical Journal Letters*, *451*(2), L83.

- Shiota, D., Kusano, K., Miyoshi, T., Nishikawa, N., & Shibata, K. (2008). A quantitative mhd study of the relation among arcade shearing, flux rope formation, and eruption due to the tearing instability. *Journal of Geophysical Research: Space Physics*, *113*(A3).
- Silva, A. V., White, S. M., Lin, R. P., De Pater, I., Gary, D. E., McTiernan, J. M., Hudson, H. S., Doyle, J. G., Hagyard, M. J., & Kundu, M. R. (1996). Comprehensive multiwavelength observations of the 1992 January 7 solar flare. *The Astrophysical Journal Supplement Series*, *106*, 621.
- St. Cyr, O. C., & Webb, D. F. (1991). Activity associated with coronal mass ejections at solar minimum: SMM observations from 1984-1986. *Solar Physics*, *136*(2), 379–394.
- Sturrock, P. (1966). Model of the high-energy phase of solar flares. *Nature*, *211*(5050), 695–697.
- Sturrock, P., & Smith, S. M. (1968). Magnetic-field structure associated with coronal streamers. *Solar Physics*, *5*(1), 87–101.
- Sturrock, P. A., Weber, M., Wheatland, M. S., & Wolfson, R. (2001). Metastable magnetic configurations and their significance for solar eruptive events. *The Astrophysical Journal*, *548*(1), 492.
- Sun, X., Bobra, M. G., Hoeksema, J. T., Liu, Y., Li, Y., Shen, C., Couvidat, S., Norton, A. A., & Fisher, G. H. (2015). Why is the great solar active region 12192 flare-rich but CME-poor? *Astrophysical Journal*, *804*(2), L28.
- Takasao, S., Asai, A., Isobe, H., & Shibata, K. (2011). Simultaneous observation of reconnection inflow and outflow associated with the 2010 August 18 solar flare. *The Astrophysical Journal Letters*, *745*(1), L6.
- Tanaka, K., & Nakagawa, Y. (1973). Force-free magnetic fields and flares of august 1972. *Solar physics*, *33*(1), 187–204.
- Tang, F. (1987). Quiescent prominences-where are they formed? *Solar physics*, *107*(2), 233–237.
- Temmer, M., Veronig, A., Vršnak, B., Rybák, J., Gömöry, P., Stoiser, S., & Maričić, D. (2008). Acceleration in fast halo cmes and synchronized flare HXR bursts. *The Astrophysical Journal Letters*, *673*(1), L95.
- Teriaca, L., Falchi, A., Falciani, R., Cauzzi, G., & Maltagliati, L. (2006). Dynamics and evolution of an eruptive flare. *Astronomy & Astrophysics*, *455*(3), 1123–1133.

- Thalmann, J., Su, Y., Temmer, M., & Veronig, A. (2015). The confined X-class flares of solar active region 2192. *The Astrophysical Journal Letters*, *801*(2), L23.
- Thalmann, J. K., & Wiegmann, T. (2008). Evolution of the flaring active region NOAA 10540 as a sequence of nonlinear force-free field extrapolations. *Astronomy & Astrophysics*, *484*(2), 495–502.
- Thalmann, J. K., Wiegmann, T., & Raouafi, N.-E. (2008). First nonlinear force-free field extrapolations of SOLIS/VSM data. *Astronomy & Astrophysics*, *488*(3), L71–L74.
- Titov, V., & Démoulin, P. (1999). Basic topology of twisted magnetic configurations in solar flares. *Astronomy and Astrophysics*, *351*, 707–720.
- Titov, V., Priest, E., & Demoulin, P. (1993). Conditions for the appearance of “bald patches” at the solar surface. *Astronomy and Astrophysics*, *276*, 564.
- Titov, V. S. (2007). Generalized squashing factors for covariant description of magnetic connectivity in the solar corona. *Astrophysical Journal*, *660*(1), 863.
- Titov, V. S., Hornig, G., & Démoulin, P. (2002). Theory of magnetic connectivity in the solar corona. *Journal of Geophysical Research: Space Physics*, *107*(A8), SSH–3.
- Toriumi, S., Schrijver, C. J., Harra, L. K., Hudson, H., & Nagashima, K. (2017). Magnetic properties of solar active regions that govern large solar flares and eruptions. *Astrophysical Journal*, *834*(1), 56.
- Török, T., & Kliem, B. (2005). Confined and ejective eruptions of kink-unstable flux ropes. *The Astrophysical Journal Letters*, *630*(1), L97.
- Tousey, R., Austin, W., Purcell, J., & Widing, K. (1973). Space research XIII, ed. *Rycroft, MJ, Runcorn SK*, (p. 173).
- Tsuneta, S. (1996). Structure and dynamics of magnetic reconnection in a solar flare. *The Astrophysical Journal*, *456*, 840.
- Tsuneta, S. (1997). Moving plasmoid and formation of the neutral sheet in a solar flare. *The Astrophysical Journal*, *483*(1), 507.
- van Ballegooijen, A. A., & Martens, P. (1989). Formation and eruption of solar prominences. *The Astrophysical Journal*, *343*, 971–984.

- van der Walt, S., Schönberger, J. L., Nunez-Iglesias, J., Boulogne, F., Warner, J. D., Yager, N., Gouillart, E., Yu, T., & the scikit-image contributors (2014). scikit-image: image processing in Python. *PeerJ*, 2, e453.
- Vourlidas, A., Lynch, B. J., Howard, R. A., & Li, Y. (2013). How many CMEs have flux ropes? deciphering the signatures of shocks, flux ropes, and prominences in coronagraph observations of CMEs. *Solar Physics*, 284(1), 179–201.
- Wang, D., Liu, R., Wang, Y., Liu, K., Chen, J., Liu, J., Zhou, Z., & Zhang, M. (2017). Critical height of the torus instability in two-ribbon solar flares. *Astrophysical Journal*, 843(1), L9.
- Wang, R., Liu, Y. D., Dai, X., Yang, Z., Huang, C., & Hu, H. (2015). The role of active region coronal magnetic field in determining coronal mass ejection propagation direction. *The Astrophysical Journal*, 814(1), 80.
- Wang, Y., & Zhang, J. (2007). A comparative study between eruptive X-class flares associated with coronal mass ejections and confined X-class flares. *The Astrophysical Journal*, 665(2), 1428.
- Wang, Y. M. (2002). A statistical study on the geoeffectiveness of earth-directed coronal mass ejections from march 1997 to december 2000. *Journal of Geophysical Research*, 107(A11).
- Webb, D., & Hundhausen, A. (1987). Activity associated with the solar origin of coronal mass ejections. *Solar physics*, 108(2), 383–401.
- Wheatland, M., & Regnier, S. (2009). A self-consistent nonlinear force-free solution for a solar active region magnetic field. *The Astrophysical Journal Letters*, 700(2), L88.
- Wiegelmann, T. (2008). Nonlinear force-free modeling of the solar coronal magnetic field. *Journal of Geophysical Research: Space Physics*, 113(A3).
- Wiegelmann, T., & Sakurai, T. (2012). Solar force-free magnetic fields. *Living Reviews in Solar Physics*, 9(1), 5.
- Woods, T., Eparvier, F., Hock, R., Jones, A., Woodraska, D., Judge, D., Didkovsky, L., Lean, J., Mariska, J., Warren, H., et al. (2010). Extreme Ultraviolet Variability Experiment (EVE) on the Solar Dynamics Observatory (SDO): Overview of science objectives, instrument design, data products, and model developments. In *The solar dynamics observatory*, (pp. 115–143). Springer.
- Wu, S., Sun, M., Chang, H., Hagyard, M., & Gary, G. (1990). On the numerical computation of nonlinear force-free magnetic fields. *The Astrophysical Journal*, 362, 698–708.

- Wu, Y., Tang, Y., Dai, Y., & Wu, G. (2002). The solar origin of the 6 January 1997 coronal mass ejection. *Solar Physics*, *207*(1), 159–171.
- Wyper, P., DeVore, C., & Antiochos, S. (2018). A breakout model for solar coronal jets with filaments. *The Astrophysical Journal*, *852*(2), 98.
- Xue, Z., Yan, X., Yang, L., Wang, J., & Zhao, L. (2017). Observing formation of flux rope by tether-cutting reconnection in the sun. *The Astrophysical Journal Letters*, *840*(2), L23.
- Yashiro, S. (2005). Visibility of coronal mass ejections as a function of flare location and intensity. *Journal of Geophysical Research*, *110*(A12).
- Zhang, J., & Dere, K. (2006). A statistical study of main and residual accelerations of coronal mass ejections. *Astrophysical Journal*, *649*(2), 1100.
- Zhang, J., Dere, K. P., Howard, R. A., Kundu, M. R., & White, S. M. (2001). On the temporal relationship between coronal mass ejections and flares. *Astrophysical Journal*, *559*(1), 452–462.
- Zhou, G., Wang, J., & Cao, Z. (2003). Correlation between halo coronal mass ejections and solar surface activity. *Astronomy & Astrophysics*, *397*(3), 1057–1067.

Appendices

Appendix A

Highly Twisted Region with $T_c = 0.1$

To investigate the lowest value of T_c should be applied in the comparison of $\Phi_{T_w \geq T_c}$ and Φ_{Ribbon} , here we also perform the analysis described in §3.2.1 based on $T_c = 0.1$. The scatter plot of $\Phi_{|T_w| \geq 0.1}$ and Φ_{Ribbon} is shown in Figure A.1. We found that the correlation coefficient derived using $T_c = 0.1$ is 0.825, which is higher than using $T_c = 0.2$ (where the correlation coefficient is 0.782), implying that the correlation tends to become better with a lower threshold. However, the slope of the regression line is greater than 1, and the difference between 1 is even larger when using $T_c = 0.2$. This result implies that the magnetic flux within the area of $T_c = 0.1$ is no longer on the same scale as the flare-ribbon flux as using $T_c = 0.2$. As a result, in this study, we use $T_c = 0.2$ as the lowest threshold for comparing with the flare-ribbon flux.

Moreover, the ability to identify each isolated highly twisted region (*i.e.*, the blobs are not encompassing the entire AR, and the separation between the blobs can be visibly confirmed, which is defined with a subjective threshold) becomes impossible when applying $T_c = 0.1$. As demonstrated in Figure A.2, we present the twist maps of event #38, and the area with twist value larger than T_c ($T_c \in [0.1, 0.5]$) is highlighted by the pink contours. One can find that the number of isolated highly twisted regions is the most when applying the lowest threshold ($T_c = 0.1$), and these patches almost connect to each other. Recalling that besides applying the thresholding method, we additionally took into account the flare's ribbon location to find the appropriate flux rope's footpoint region. In this case, we fail to accurately choose the patches associated with the flare ribbons.

To examine that if a partitioned twist map can show recognizable, isolated patches or not at a certain T_c value, we estimate the total amount of the separated blobs formed by the thresholding method across all 51 events, with T_c varies from 0.1 to 0.5. The resulting averaged amounts of blobs

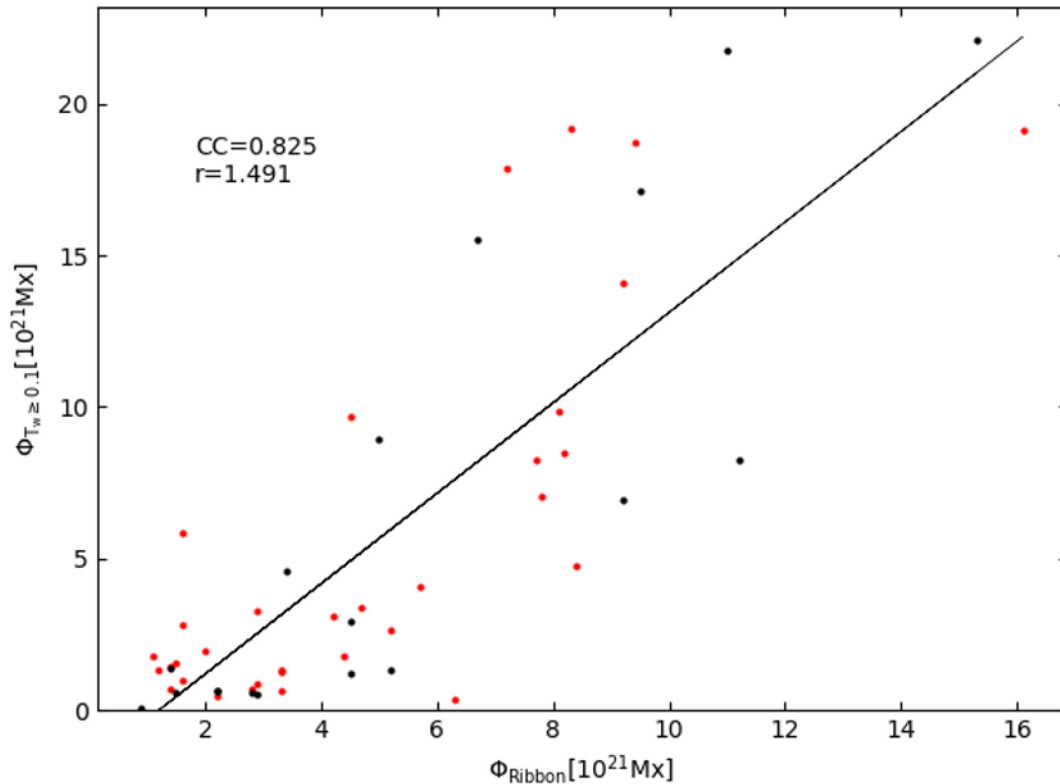


Figure A.1: Scatter plot presents the comparison of the $\Phi_{|T_w| \geq 0.1}$ and the Φ_{Ribbon} . Red (black) dots represent eruptive (confined) events. A straight line shows the result of a linear fit, while the correlation coefficient (CC) and the slope of regression line (r) are shown at the top left.

are 58.6, 31.5, 17.2, 9.5, and 6.5, corresponding to $T_c = 0.1$ to 0.5, respectively. It can be seen that the averaged amount of blobs with using $T_c = 0.1$ is greatly larger than with using other values of T_c ; thus the partitioning results are expected to be un-recognizable when applying $T_c = 0.1$. We therefore invoke the analysis with T_c starts from 0.2.

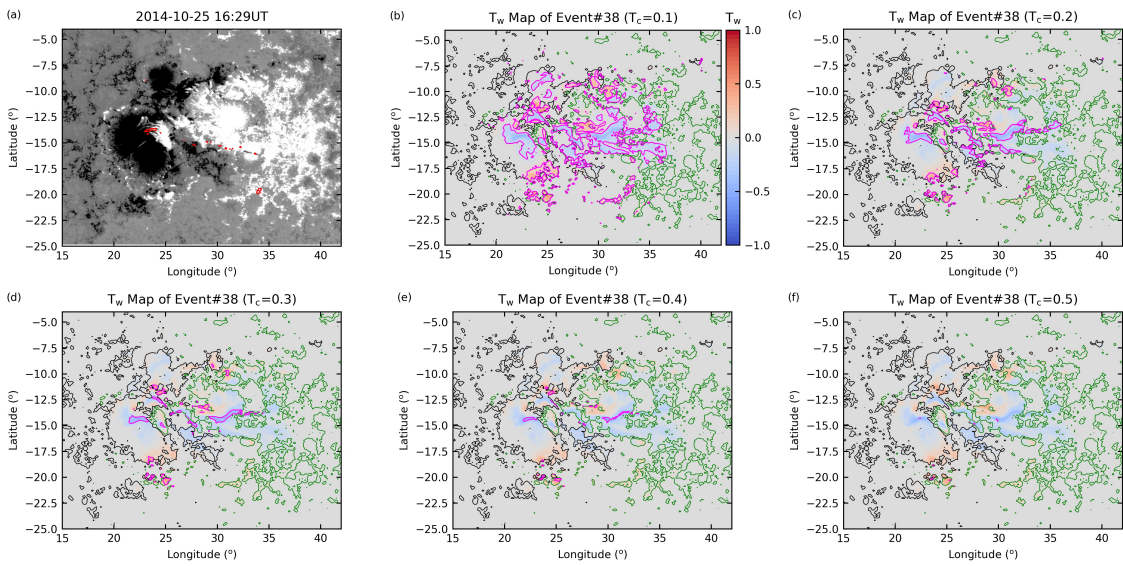


Figure A.2: (a) AIA 1600 Å emission captured at 25 October 2014 16:29 UT shows flare ribbons patterns (red contours) overlaid on SHARP magnetogram (saturated at ± 500 Gauss). The threshold used to highlight the emission patterns is the intensity that is equal to or larger than the mean value for 20σ (standard deviation) at a Sun-quiet time. (b)-(f) Twist maps for AR12192 calculated from NLFFF extrapolation at a time corresponding to event #38. In each sub-panel, the pink contours are the foot prints of the field lines twist larger than 0.1, 0.2, 0.3, 0.4, and 0.5 turns, respectively.

Appendix B

Error Analysis

We evaluated the expected sensitivity to the uncertainty in the magnetic boundary data through a Monte Carlo analysis of one event (event #1) and assume that the results are representative of expected data-imposed uncertainties for the analysis of the other 50 events. For event #1, reported uncertainties provided in the `hmi.sharp_cea_720s` segments: `Br_err.fits`, `Bp_err.fits`, and `Bt_err.fits`. The uncertainty at each pixel is multiplied by a random number generated from a distribution with normal distribution and unity variance, and added to the magnetogram used as the lower boundary of NLFFF extrapolation. The whole process was repeated 16 times, to obtain 16 sets of NLFFF data with different fluctuations as per realizations of the noise. We consequently estimate the variables that are used in this study (*e.g.*, $\Phi_{|T_w| \geq 0.2}$, etc.) using these data sets, and derive the corresponding standard deviation across all 16 data sets. These standard deviations provide the percentage errors quoted in Tables 3.2, 4.2, 4.4.

To test the reliability of the discriminant analysis metrics, we estimate their uncertainties by two methods: (1) Monte Carlo method to estimate the errors that arise from the errors in the data, and (2) a bootstrap algorithm to indicate the uncertainties that arise from the small sample size.

For (1) the Monte Carlo method, the uncertainties for each parameter are inherited from the uncertainties of Φ and Φ_τ as described above. We perform the DA on 10,000 sets of a parameter chosen for testing wherein for each set, uncertainties are added based on Gaussian-distributed random numbers and the standard deviation of the error values of Φ or Φ_τ to calculate the corresponding values of parameters in the r -scheme and the q -scheme. The uncertainties from this method are generally quite small.

The bootstrap method (2) provides uncertainty levels that arise from the sampling process. We

reconstruct the samples by drawing (with replacement) 51 samples from the original data set to obtain a different realization of samples. Each realization thus may include repeated samples, and present a different event rate. We repeat this resampling procedure 100 times, and obtain 100 sets of resulting DA metrics from which we calculate the standard deviation, and report it as the uncertainty in that metric.

Appendix C

Flare Ribbon Area Sensitivity to Different Intensity Thresholds

An intensity threshold is defined for AIA 1600 Å observations above which we label pixels as having brightened sufficiently to be included as part of the “flare ribbons”. This 1600Å intensity threshold is empirically imposed as 20σ above the mean 1600Å intensity at a flare-quiet time. This brings us to the question to what extent does the choice of the threshold affect the resulting flare-ribbon area and associated magnetic flux calculations?

To answer this question, we adjust the threshold across $10\sigma - 30\sigma$, and from the resulting flare ribbon masks we calculate the corresponding values of Φ_{Ribbon} , $\Phi_{\text{overlying,R}}$, and $\Phi_{\text{wall,R}}$ following the method outlined in §4.2.2. We consequently calculate the differences in the yielded values relative to those calculated using the 20σ threshold, where the variation is defined as:

$$\Delta\Phi_{\text{Ribbon},n\sigma} = \frac{|\Phi_{\text{Ribbon},n\sigma} - \Phi_{\text{Ribbon},20\sigma}|}{\Phi_{\text{Ribbon},20\sigma}}, \quad (\text{C.1})$$

where $\Phi_{\text{Ribbon},n\sigma}$ indicates the flare-ribbon-related magnetic flux calculated with the intensity threshold at $n\sigma$ above the mean quiet 1600Å intensity. The maximum variation among the values derived with $n \in [10, 30]$ is provided in Table C.1. Mirroring the estimation of $\Delta\Phi_{\text{Ribbon},n\sigma}$, we calculate $\Delta\Phi_{\text{overlying,R},n\sigma}$ and $\Delta\Phi_{\text{wall,R},n\sigma}$ as

$$\Delta\Phi_{\text{overlying,R},n\sigma} = \frac{|\Phi_{\text{overlying,R},n\sigma} - \Phi_{\text{overlying,R},20\sigma}|}{\Phi_{\text{overlying,R},20\sigma}}, \quad (\text{C.2})$$

$$\Delta\Phi_{\text{wall,R},n\sigma} = \frac{|\Phi_{\text{wall,R},n\sigma} - \Phi_{\text{wall,R},20\sigma}|}{\Phi_{\text{wall,R},20\sigma}}. \quad (\text{C.3})$$

The maximum variation of the overlying-field and wall-field term is also listed in Table C.1. We find that the variation can reach seven times the original flux (Φ_{Ribbon} in event #43), although sometimes the values change minimally (*e.g.*, event #25). In general, the flare-ribbon magnetic flux varies between 10% to 90% from what was used in the present analysis, indicating a fairly strong sensitivity to the empirical threshold used to determine what constitutes a flare ribbon. We note that this large uncertainty is consistent with the conclusions regarding the difficulty of determining the MFR characteristics.

From relevant literature, Qiu et al. (2010) denoted that the “steady-state” UV brightening associated with plage regions is generally at 3.5 times the background median value. A threshold set at 10σ above the mean intensity will typically be greater than this value. As a result, we expect that an intensity threshold at least $\geq 10\sigma$ above the background mean intensity would be suitable to capture the major morphology of flare ribbons. Besides the 20σ threshold applied herein, Toriumi et al. (2017) applied a threshold intensity at 40σ above the quiet-Sun mean values; Kazachenko et al. (2017) used thresholds ranging 6 – 10 times above the background median value. These thresholds are all substantially greater than that suggested by Qiu et al. (2010).

Next we discuss that which threshold is most appropriate for this study. We apply DA on the parameters as yielded with the threshold intensity at $n\sigma$ above the mean values, adjusting n across 10 – 30, to see how the discrimination ability changes across different value of n . Table C.2 shows all of the used DA metrics averaged across all q -parameters varies with n . The listed quantities demonstrate that the averaged DA metrics show comparative performances when $n \in [10, 20]$, while the performance drastically decreases at and beyond $n = 25$. Therefore, we elect $n = 20$ in our analysis such that we will not underestimate the performance of the q -scheme.

Event#	Φ_{Ribbon} (10^{20}Mx)	$\Phi_{\text{overlying,R}}$ (10^{20}Mx)	$\Phi_{\text{wall,R}}$ (10^{20}Mx)
1	1.91	0.19	0.16
2	0.54	0.38	0.02
3	1.51	0	0.30
4	0.27	0.68	1.16
5	0.42	0.25	0
6	0.61	0.93	1.15
7	0.37	1.61	4.70
8	0.15	1.85	0.74
9	0.50	0.67	0.34
10	4.12	1.46	2.36
11	0.28	1.00	0
12	1.73	0.85	0
13	0.13	0.40	0.03
14	0.43	0.25	0.22
15	0.34	0.74	0.59
16	0.85	0.46	3.19
17	0.55	0.14	0.20
18	0.80	0.34	0.34
19	2.00	1.93	1.64
20	0.49	1.23	0.23
21	1.17	0.50	0.14
22	0.65	0.97	0.38
23	0.34	0.72	0.01
24	0.12	0.17	0.80
25	0.04	0.14	0.02
26	0.08	0.18	0
27	0.05	0.95	0.01
28	1.01	0.19	0.03
29	0.45	1.58	2.01
30	0.57	0.09	0.01
31	0.23	0.39	0.18
32	0.22	0.36	0
33	0.77	0.77	0
34	0.61	0.08	0.31
35	0.78	0.38	0.23
36	0.34	0	0
37	0.47	0.65	0.30
38	0.33	0.30	0
39	0.88	0.70	0.06
40	0.87	0.70	0.16
41	0.20	0.21	0
42	0.16	0.70	0.06
43	7.77	0.23	1.06
44	0.85	0.22	0
45	0.71	0.32	0.01
46	0.26	2.80	5.39
47	0.43	0.34	0.30
48	0.65	0.27	0
49	0.30	0.38	0.10
50	0	1.14	0.04
51	0.26	0.46	0

Table C.1: Maximum variation rate with different intensity thresholds

Parameter	Statistical Metrics			
	Probability (%)	MD ^a	CR ^b	TSS
10	98.0	1.09	0.76	0.46
15	98.2	1.07	0.76	0.45
20	97.7	0.96	0.76	0.45
25	95.7	0.74	0.69	0.26
30	95.5	0.73	0.66	0.20

^a Mahalanobis distance for the sample PDFs.

^b Correct rate of the classification table.

Table C.2: DA results (with $n - 1$ cross-validation)